YOKOHAMA NATIONAL UNIVERSITY

Doctoral Thesis

Bayesian uncertainty quantification of model parameters of existing structures using earthquake response data

Author:

TRAN Thi Xuan Thanh

Supervisor: Assoc. Prof. Mayuko NISHIO

A thesis submitted in fulfillment of the requirements
for the degree of Doctor of Philosophy in Engineering
in the
Department of Urban Innovation

September 7th, 2018

Abstract

In modeling existing structures for seismic response analysis, parameter uncertainties due to seismic loading histories cannot be ignored. The models need to be updated considering those uncertainties. The updated models can be used for monitoring the health of structures, especially the ones suffering from large earthquakes. A combination of global sensitivity analysis (GSA) and uncertainty quantification (UQ) is often used for updating uncertain structural parameters. GSA can extract significant features of model outputs before UQ is applied. The validity of resulting posterior distributions from UQ strongly depends on how sensitive each parameter is on the outputs. However, sensitivity degree significantly varies under different seismic loadings, and therefore has unneglectable impacts on the validity of the distributions.

Global sensitivity analysis (GSA) via Monto Carlo methods (MCSA), which can indicate model parameters' importance to responses, requires a high computational cost. Alternatively, GSA can be conducted using metamodels which represent the input-output relationship based on training data following Bayesian approach, i.e., Bayesian sensitivity analysis (BSA). Firstly, we showed the applicability of BSA for linear and nonlinear dynamic models by comparing with MCSA. Then, dynamic property changes on the existing base-isolated building due to the Great East Japan earthquake in 2011 were verified by system identification and transfer function analysis using earthquake response monitoring data. Here, the possibility of local stiffness changes in the superstructure was clarified. Finally, BSA was applied to the numerical model of the building. It was shown that effect of local stiffness on maximum responses is strongly related to mode shapes, and the response monitoring data of small earthquakes could be used for reducing and updating those local parameters' uncertainties. It was concluded that BSA with selected response features was applicable to understand the sensitivity of model parameters to output responses in modeling of the existing structure.

The second contribution of this study is to simulate reliable posterior distributions of the model parameters which will be useful for accurate reliability estimations. The testbed structure is a standard two-degree-of-freedom (DOF) isolated bridge pier used in Japan design specifications for highway bridges. Firstly, a numerical model of bridge pier and isolators with the nonlinear response characteristics were constructed using a Takeda model and a bilinear model respectively. Monitoring data was then simulated by adding white noise to the model outputs under assumed damage and undamaged conditions of the structure. Significant feature extraction was then implemented by GSA using Kriging metamodels. The procedure chooses significant response data from the long-term monitoring data for UQ implementation afterward. Finally, a sequential uncertainty quantification procedure of the structural parameters using the long-term monitoring data was constructed. The proposed procedure can derive optimal and efficient posterior distributions of the parameters. Moreover, the procedure allows the effective and efficient use of the long-term monitoring data in reliability analysis.

Acknowledgement

A research project is never the work of anyone alone. The contributions of many different people, in their different ways, have made this possible. I would like to extend my appreciation especially to the following individuals.

My deep gratitude to my supervisor, Prof. Mayuko Nishio, who has supported me thoughout my thesis with her patience, expertise and experience. I have been lucky to have an advisor like her to help me overcome many difficulties, personal and professional, throughout the duration of my study. I am also thankful to her for carefully reading and commenting on revisions of this thesis.

I wish to express my gratitude to Prof. Hitoshi Yamada, Prof. Hiroshi Katsuchi, prof. Yozo Fujino, Dr. Dionysius Siringoringo, Dr. Haeyoung Kim for their constructive comments and suggestions during my PhD progress. And I am also very grateful to my other committee member, Assoc. Prof. Mamoru Kikumoto for his great comments during my preliminary defense.

I would like to thank Dr. Yozo Fujino, professor of Yokohama National University and Dr. Katsuaki Konno, professor of Shibaura Institute of Technology, for sharing the monitoring data from the base-isolated building. The data acquisition was conducted by the Strategic Research Program of Japan Science and Technology (JST) in advanced integrated sensing technology (CREST) under the title 'Risk Monitoring and Disaster Management of Urban Infrastructure' (PI: Yozo Fujino). We are also grateful to Dr. Dionysius M. Siringoringo, associate professor of YNU, especially on implementing the system identification using the monitoring data and sharing the numerical model of the testbed building. Additionally, we thank Ms. Hiroko Fujii and Ms. Risa Kuroda, graduate students of YNU, for their contributions especially to the analysis of monitoring data.

My appreciation goes to my fellow lab-mates for the stimulating discussions, help and support during my three years in interesting topics related to my research. I also enjoyed lab trips, the parties, and hangouts with them at the weekend.

I would like to thank to The Ministry of Education, Culture, Sports, Science and Technology (MEXT), Japan for their financial support granted through my studies.

Last but not the least important, I owe more than thanks to my family members, my boyfriend Ekin Ozer for their encouragement throughout my study.

Contents

List of Tables

List of Figures

Chapter 1

Introduction

1.1 Background and Research Gaps

1.1.1 Health monitoring of existing structures

Structural health monitoring (SHM) aims to observe deterioration or damages of structures in situ and determine the structural property changes qualitatively and quantitatively. Nowadays, with the increasing development of advanced technologies, e.g., measurement sensors, innovated calculation methods, the structural changes can hence be identified or predicted by the analyses using the monitoring data. Based on analysis results, the structures can be retrofitted, repaired or replaced timely to prevent risks in the future.

Infrastructure systems including houses, buildings, bridges, roads, etc. are essential components of society and civilization. Therefore, their safety and integrity are priority all the time. However, the infrastructure is increasingly aging and may have potential damages in the future. Moreover, natural disasters such as strong wind, tsunami, flood, especially earthquake which is concerned in this study, can cause serve damages for the existing structures. To a certain extent, damaged structural components can be repaired or replaced by new ones; however, they are not always feasible to execute due to difficulties in financial problems, environment conditions, or structural complexity. Hence, continuous structural health monitoring of the existing structures over time is essential to predict future damages and increase their serviceable time as much as possible.

For seismic risk assessment of the existing structures related to structural performances, numerical modeling with considering parameter uncertainties related to its current structural conditions is required. The numerical models incorporating seismic response monitoring data is then applicable for uncertainty quantification and model updating. One of the influential factors to the seismic response is model parameter uncertainty due to unrecognizable property changes occurred in previous earthquakes.

These accumulated changes over time may cause damages in the future huge earthquakes. Therefore, diagnosing the abnormal structural changes is essentially required to fix them timely. Moreover, for future proper maintenance or renovation work, understanding structural responses, especially the relationship between input and output under future earthquakes is desired. For these purposes, a properly updated model is essential. However, existing structures with complex structural geometry require high degree-of-freedom models and nonlinear time-history response analyses. Moreover, the seismic risk assessment must consider not only the uncertainty of structural properties but loading history. The sensitivity analysis can estimate how much the variability of the inputs affect to the one of the output responses under any earthquakes. The sensitivity analysis thus takes a key role to construct a validated numerical model for such the seismic risk analysis of the existing structures.

To predict the consequence of damages, structural reliability estimation is essential as it supports to propose effective maintenance strategies, suggest more crucial repair and retrofit works in time. However, uncertainties such as loading history, deteriorating structural elements, boundary conditions, among others have been always challenging to accuracy of reliability estimates. Over decades, the integration of numerical models and monitoring data in reliability analysis has been expected to improve estimation results, e.g., fragility curve or failure probability, as closely as to real-life performances. Ajay Singhal et al. (Singhal and Kiremidjian, 1998) combine building damage data from past earthquakes with analytical ground motion to update fragility curve of the structure. Catbas F.N. et al. (Catbas, Susoy and Frangopol, 2008) and Frangapol D.N. et al. (Frangopol, Strauss and Kim, 2008) efficiently include monitoring data, e.g., strain measurement, to reduce uncertainties of prediction models in a probabilistic sense in the reliability estimation. Serdar Soyoz et al. (Serdar Soyoz, M.ASCE; Maria Q. Feng, M.ASCE; and Masanobu Shinozuka, 2010) and Ozer E. et al. (Özer and Soyöz, 2015) indicated that failure probability of the systems estimated using updated structural parameters based on measurement data, e.g., stiffness and damping, is higher than the one using non-updated parameters. Any false model updating which does not represent real response of the structures will lead to inaccurate reliability estimates. For this reason, the reliability of the updated model parameters considering uncertainties from both loading history and structural changes need to be considered carefully. Moreover, monitoring data of interest in this study is response data collected from rare earthquakes, hence the effective and efficient use of the long-term data to update the model parameters is also concerned.

1.1.2 Model uncertainty

The knowledge about the existing structures and their abnormal structural changes subjected to external loadings are always uncertain. The uncertainty is an unavoidable obstacle in modeling of the existing structures. In SHM, numerical models incorporating with sensing data is a common practice to understand the structural response characteristics and keep them updated in time. Updated structural parameters, e.g., stiffness, yield load, etc., in either a deterministic or probabilistic manner can be used to not only assess post-event damages, but also predict the damaging consequences on future structural performances via reliability estimations.

The uncertainty sources of the models are basically categorized into two sorts of aleatoric and epistemic uncertainties. The aleatoric uncertainty is defined for irreducible errors resulted from random effects of systems. The epistemic uncertainty is originated from systematic errors such as simplification of mathematical representatives, lack of knowledge on the model parameters. Structural damages due to external effects can be sorted to the epistemic uncertainty. Both uncertainties can be performed in a probabilistic framework. This study will focus on clarifying and quantifying the epistemic uncertainty which is deducible by the aid of the numerical models, the monitoring data and up-to-date methodologies.

1.1.3 Sensitivity analysis

Sensitivity analysis (SA) is a common tool to interpret the effect of input variability on output variability, and hence which parameters are more sensitive than others can be indicated. For simple linear models, local SA is efficient to point out prominently sensitive parameters with no interaction between variables is considered. Unlike local SA, global SA can quantify the uncertainty in the whole input space considering the simultaneous variability of all inputs. Monte Carlo simulation can be hence applied to calculate high-order sensitivity indices, i.e., main index and interactions. The complicated models struggle with high computational cost, which is the case in most civil engineering models.

Local SA focuses on the response variability of the system subjected to a small permutation around a designed point (Saltelli, 2008). With concerning sensitivity of local points, local SA will become important to have fast evaluations which commonly require low computational costs. When decisive evaluation in a whole picture of nonlinear systems is concerned, local SA is not recommended. However, many previous studies, e.g., (Lomas and Eppel, 1992), (Lam and Hui, 1996) opted this method for the sake of sensitivity analysis of building energy models because of its cheap computational cost.

Global sensitivity analysis (GSA) aims to describe how changes in model inputs affect model outputs, and hence can extract significant uncertain parameters. Some GSA techniques consist of: (i) variance-based methods such as Sobol' method (Sobol, 1990), and Fourier Amplitude Sensitivity Test (FAST) (Cukier *et al.*, 1973; Saltelli, 2008); (ii) screening-based method such as Morris's method (Morris, 1991; Heiselberg *et al.*, 2009); (iii) regionalized sensitivity analysis (RSA) (Spear and Hornberger, 1980); (iv) regression-based method, such as correlation/ regression coefficient (Helton, 1993). Sobol and FAST methods can apply for nonlinear models with correlated input parameters. Two famous measures of those methods include main and total sensitivity indices. Unlike first-order index, total index consider both main effect and the interaction between the parameters. Morris's method or called Elementary Effect Test (EET) in (Saltelli, 2008) aims to derives partially the model response at evenly-distributed points. The method can provide the information regarding the interaction between the concerned parameter to others.

One of GSA methods which is mostly used is variance-based SA (VBSA) (Saltelli, 2008). The advantages of VBSA include model independence, the provision of a complete picture of models considering simultaneous variations of all input parameters, and the ability to treat a group of variables as a scalar variable. The Sobol' indices (Sobol', 1993) which indicate variance-based sensitivity measures come from the Sobol' decomposition (Hoeffding, 1948). Generally, the Monte Carlo based sensitivity analysis method (MCSA) (Sobol', 2001) which known as the most robust has been used to estimate the indices. However, these sampling-based methods which require thousands of simulation runs are not desirable due to the operating incapability in complex models. Therefore, there is an increasing demand for developing alternative mathematical approximation models, metamodels or surrogate models to eliminate computational burden.

In recent decades, GSA methods using reduced models emerges as an efficient method for complicated models. However, the reliability of the methods strongly depends on how precise the reduced models can represent system responses. To estimate Sobol' indices, Chen et al. (2006) suggested tensor-product formulation to calculate the mean of Gaussian process models, while Oakley and O'Hagan (2004) applied the Bayesian formalism of Gaussian processes considering all the global stochastic models including mean and variance. The latter method has been known as Bayesian sensitivity analysis (BSA). The application of BSA in civil engineering is quite new. Several recent studies used BSA to identify parameter importance in building energy models, see a review (Tian, 2013). Becker et al. (2012) demonstrated efficient use of Gaussian process-based surrogates on large multi-variate models with significantly reduced computing cost through a nonlinear airship model. However, the performance of surrogates in BSA has not been verified

especially for structural dynamics of complex modeling structures with high DOF and nonlinearity.

1.1.4 Metamodeling

Surrogate modeling or metamodeling methods can be categorized into three approaches such as data-driven surrogates, projection-based methods, and multi-fidelity based surrogates as reviewed in Asher et al., 2015. Data-driven metamodels approximate the system response by artificial models which capture the input-output relationship mapping with the actual model. Projection-based models try to reduce the dimensionality of the system by projecting the alternative mathematical representatives into an orthogonal space. The multi-fidelity or called hierarchical models is known probabilistic based models. This method treats mathematical functions as stochastic responses.

Metamodels have been developed by statistical algorithms such as Kriging (Sacks *et al.*, 1989; Welch *et al.*, 1992; Kennedy and O'Hagan, 2001a), polynomial chaos expansions (Ghanem and Spanos, 1991; Xiu and Karniadakis, 2002), artificial neural networks (ANNs) (Schueremans and Van Gemert, 2005), radial basic functions (RBFs) (Regis and Shoemaker, 2005), sparse grid interpolation (Xiong *et al.*, 2010). Among these, Kriging metamodeling is most common and effective to construct reduced models based on Design-of-Experiments.

In this study, we focus on a method addressing multi-fidelity based surrogates, named Kriging or Gaussian Process Regression (GPR) (Rasmussen, 2006; Kennedy and O'Hagan, 2001). Kriging is a surrogate technique which first developed by (Krige, 1952) in the geo-statistics, then introduced in computer experiments by Sacks *et al.*, 1989; Welch *et al.*, 1992. GPR interpolates unknown values from prior covariances based on smoothness criteria. The prior covariances are built on input samples and corresponding outputs from the original model. Depending on acceptable accuracy level of surrogates, these models can then be used to calculate sensitivity indices and uncertainty quantification with much lower cost than the implementation of full models.

1.1.5 Uncertainty quantification

Model parameter uncertainty can be qualified and quantified by a good cooperation of sensitivity analysis and uncertainty quantification. Uncertainty quantification (UQ) following Bayesian inference can reduce the uncertainty of input model parameters for model updating. Uncertain sources can be modeling errors due to the lack of knowledge

on inputs or structural condition changes due to seismic damages under large earthquakes. Markov Chain Monte Carlo using Metropolis-Hastings algorithms (Metropolis *et al.*, 1953)(Besag *et al.*, 1995) is preferred to draw samples from non-symmetrical posterior pdfs. For high-dimensional dynamic models with multi-modal target distributions, the Differential Evolution Markov Chain algorithm (Ter Braak, 2006) can infer the posteriors precisely. Beyond that, there are some alternative methods without using MCMC sampling, e.g., optimal transportation theory (El Moselhy and Marzouk, 2012), variational strategies (Schwab *et al.*, 2012) (Franck and Koutsourelakis, 2017), and spectral likelihood expansions (Nagel and Sudret, 2016). However, the computational cost is concerned when dealing with those models by either Monte Carlo simulations or analytical calculations. Hence, metamodels which are constructed on training data are preferred to alternate the use of original models for SA and UQ efficiently.

The uncertainty degree of the parameters relates to the validity of the posteriors. Measured data can constrain the posteriors of the parameters which have high sensitivity with considerably reduced uncertainty. The ranking sensitivity of the parameters about a single output feature incorporating with UQ is often applied in the literature (Higdon *et al.*, 2008)(Sraj *et al.*, 2014)(Abdel-Khalik *et al.*, 2008). However, the ranking of multiple input parameters considering multiple features subjected to various seismic levels has not been noticed so far. This is necessary to obtain well-defined posteriors with effectively reduced uncertainty since different seismic levels cause a dissimilar impact on the variance of the outputs.

1.2 Motivation of Study

One of the influential factors to the model response is parameter uncertainty due to unrecognizable property changes occurred in previous earthquakes. These accumulated changes over time may cause damages in the future huge earthquakes; therefore, diagnosing the abnormal structural changes is essentially required to fix them timely. Moreover, for future proper maintenance or renovation work, understanding structural response characteristics, especially the relationship between input parameters and output responses under future earthquakes is desired. For these purposes, a properly updated model is essential. However, the seismic risk assessment related to structural performances must consider not only the uncertainty of structural properties but also the variability of input seismic loads, i.e., structural changes due to external forces and loading history. With complicated structures, high degree-of-freedom (DOFs) and asymmetric geometry, sensitivity analysis plays an important role to indicate critical uncertain parameters and extract significant response features in model updating, towards constructing validated numerical models of the existing structures.

Model updating aims to calibrate unknown parameters or functions to best fit with observed data. The result can be either new deterministic values or probabilistic distributions of model parameters. Deterministic model updating is often based on constrained optimization problems between model outputs and measurement, while probabilistic one involves uncertainties into inverse problems. The later method gains advantage over the deterministic one due to the inherent uncertainty of simulations and observed data. Bayesian uncertainty quantification (UQ) is a common practice to update the model parameters which are inferred from the combination of prior distributions, observed data and likelihood functions. Sensitivity analysis is often used to extract significant response features and rank the importance of the parameters before UQ is applied. The parameters are more sensitive to simulated outputs, the posterior uncertainty is more reducible. Therefore, the validity of resulting posterior distributions strongly depends on how sensitive each parameter is on the output responses. Unfortunately, sensitivity degree significantly varies under different seismic loadings, and therefore has an unneglectable impact on the validity of the distributions. As a result, not all the uncertain parameters can be always quantified effectively and precisely by using the observed response data under a certain earthquake event. This may require data of more than one event to accomplish an uncertainty quantification procedure. Hence, uncertainty quantification of the model parameters using the long-term monitoring data based on sensitivity analysis is expected to increase the reliability of the updated model parameters.

The precision of the posteriors directly affects to the accuracy of reliability estimations of the existing structures. Until today, no research work has been carried out to explain the uncertainty of updated structural parameters under different seismic characteristics, especially no consideration regarding the reliability of using these updated parameters in the reliability analysis. Henceforth, the current research work performed here is significant as it deals with two-folds: (1) evaluating sensitivity for uncertain model parameters of an existing complex structure under an “unhealthy” structural condition, (2) proposing an approach to simulate more reliable posterior distributions of the model parameters.

1.3 Aims and Scope

This study aims to generate optimal and efficient posterior distributions of the uncertain model parameters and realize the seismic risks of the existing structures using the properly updated numerical model. To reach the goal, sensitivity analysis and uncertainty quantification was conducted for numerical models under different seismic characteristics. The models that must be dealt with in this study include: (1) a base-isolated asymmetric building with the large number of DOFs to represent a complex

geometry; (2) a seismically isolated bridge pier desinged in Japan Design Specifications of Highway Bridges. Both structures require nonlinear response analysis under large seismic excitations. Sensitivity analysis of the model parameters of the existing base-isolated building can indicate potential risks which require paying attention to ensure the structure safety. Uncertainty analysis of the inferred posterior distributions using seismic response data was conducted on the isolated bridge pier. As a result, a sequential uncertainty quantification procedure using the long-term monitoring data was proposed. The procedure is expected to be applicable for any civil structures, such as buildings or bridges. Moreover, monitoring data of interest in this study is response data collected from rare earthquakes, hence the effective and efficient use of the long-term data to update the model parameters is also concerned.

1.4 Thesis layout

The current thesis is outlined as follows. After the introduction presented, including background, motivation, and the study goal in chapter 1. Chapter 2 presents theoretical descriptions about Kriging metamodeling, global sensitivity analysis, and Bayesian uncertainty quantification. The following texts presents the major work in this thesis. Firstly, seismic input and data acquisition, the configuration description of two structures, an existing base-isolated building and an isolated bridge pier in Japan Design Specifications of Highway Bridges are presented in chapter 3. For each structure, seismic response analysis, artificial monitoring data, and structural changes due to large earthquakes are presented at length. Later, chapter 4 is dedicated to applicability of Bayesian sensitivity analysis (BSA) to linear and nonlinear structures. Also, BSA is then applied on the existing building. Monte Carlo sensitivity analysis (MCSA) is introduced in chapter 5. This chapter includes Kriging metamodeling and MCSA for the isolated bridge pier under different seismic characteristics, magnitudes and frequency content. In chapter 6, uncertainty quantification using Markov Chain Monte Carlo and Differential Evolution Adaptive Metropolis algorithm is shown. At last, the author contributes to the civil engineering field with major conclusions.

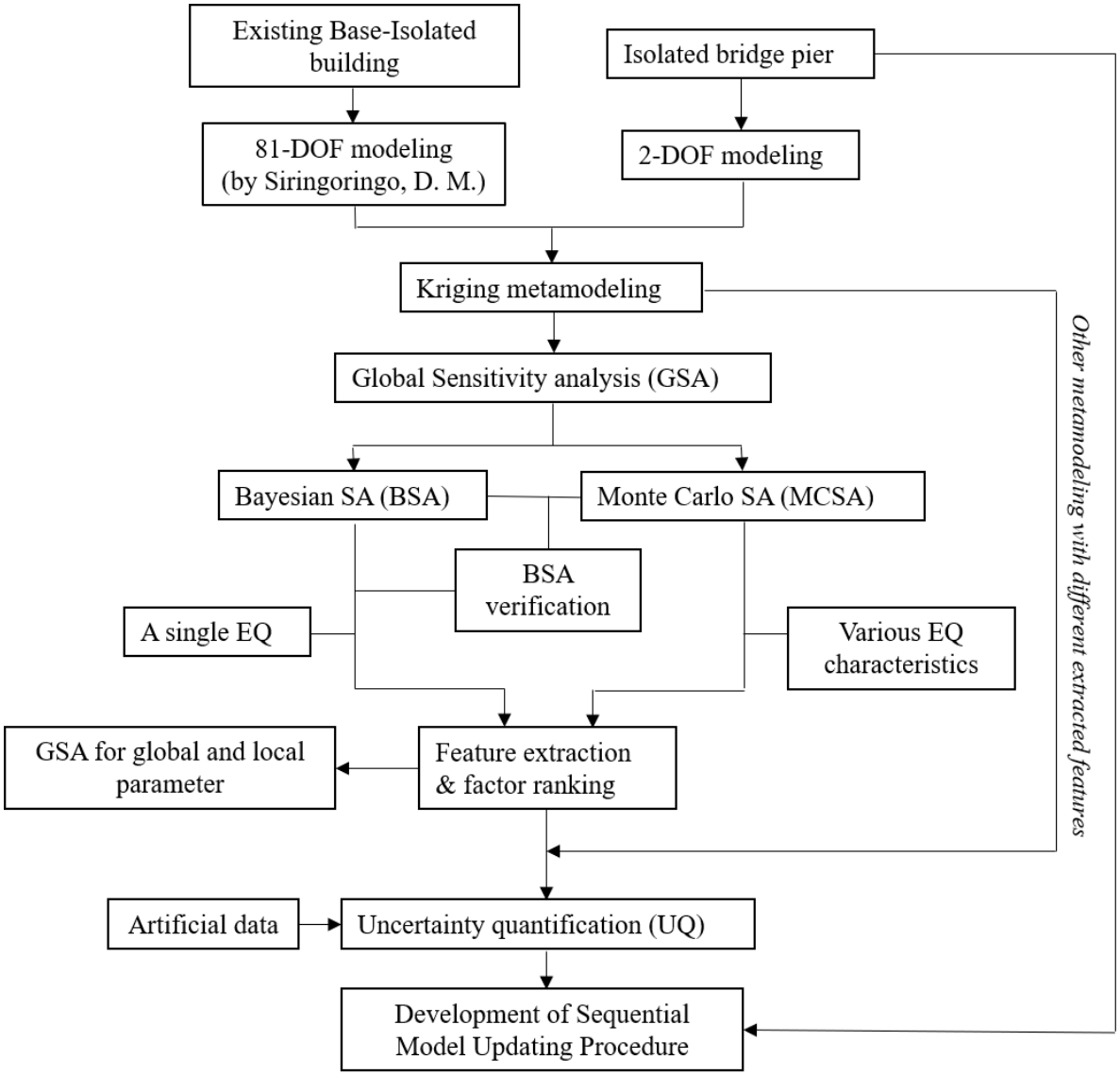

Fig. 1.1 Summary of the study procedure of sensitivity analysis and uncertainty quantification

Chapter 2

Methodologies

Bayesian statistics is adopted in inverse propagation problems of the uncertainty of model parameters. The combination of sensitivity analysis and uncertainty quantification can enhance the reliability and efficiency of posterior distribution estimations. Since the expense to calculate those estimations may exceed serviceable computing capacity, reduced models, i.e., metamodels or surrogates, are supposed to alternate original models (full models). In this chapter, Bayesian uncertainty quantification, sensitivity analysis, surrogate models, and implementation methods of integrated formula in the Bayesian framework are briefly introduced.

2.1 Kriging metamodeling

Kriging is a metamodeling technique which considers true model responses as realizations of a Gaussian process. Suppose $y = f(\mathbf{x})$ is a function representing the relationship between input and output of a numerical model. A d-dimensional input vector $\mathbf{x} = (x_1, x_2, \ldots, x_d)$ of concern is experimentally designed into a sample $\mathbf{X}s = (\mathbf{x}_1, \mathbf{x}_2, ..., \mathbf{x}_n)$, and a corresponding output matrix is $\mathbf{Y}s = f(\mathbf{x}_1, \mathbf{x}_2, \ldots, \mathbf{x}_n)$. The target is to construct the function $f(x)$ for any untried inputs; therefore, the pair of ($\mathbf{X}s$, $\mathbf{Y}s$) can be considered as a training data set D. A Gaussian process (GP) can interpolate an output of a certain input in conjugation with the learning data via covariance functions, and defined as follows:

$$f(\mathbf{x}) = m(\mathbf{x}) + e(\mathbf{x}) = \sum_{j=0}^{k} \beta_j h_j(\mathbf{x}) + e(\mathbf{x}), \text{ with } k \text{ basic functions.} \tag{2.1}$$

Without prior knowledge about the input-output relationship, $m(\mathbf{x})$ can be simplified as a one-degree polynomial with $(d+1)$ basic functions (also called trend), $\boldsymbol{\beta} = \left[\beta_0, \beta_1, ..., \beta_d\right]^T$ is the unknown regression vector, and $\mathbf{h}(\mathbf{x}) = \left[1, x_1, ..., x_d\right]$ is the known corresponding function vector. The stochastic part $e(\boldsymbol{x})$ is assumed as a zero-mean Gaussian process characterized by covariance function, possible formula given by

$$c(\mathbf{x},\mathbf{x}^{'}) = \sigma^2 R(\mathbf{x},\mathbf{x}',\theta) = \sigma^2 \exp(-\left|\sqrt{\sum_{i=1}^{d}(\frac{x_i - x'_i}{\gamma_i})^2}\right| / \gamma_i) \quad (2.2)$$

or $$c(\mathbf{x},\mathbf{x}^{'}) = \sigma^2 r(\mathbf{x}-\mathbf{x}^{'}) = \sigma^2 \prod_{i=1}^{d} \exp\left\{\gamma_i (\mathbf{x}_i - \mathbf{x}_i^{'})^2\right\} \quad (2.3)$$

with $\theta_j \geq 0$ is roughness parameters, and σ^2 is Gaussian process variance (Rasmussen, 2006). Hyperparameters can be estimated using the maximum likelihood. Note that the choice of covariance function is flexible depending on which approach we use. For instance, the approach using metamodels independently with the Bayesian inference, the function in Eq. (2.2) is used, while Eq. (2.3) is adopted using random walk Metropolis-Hasting updates.

The function $f(\mathbf{x})$ in Eq. (2.1) can be expressed via GP with a mean and covariance kernel instead. A GP conditional on the learning data can be denoted as follows:

$$F_n(\mathbf{x}) \sim GP(m_n(\mathbf{x}), s_n^2(\mathbf{x},\mathbf{x}^{'})), \quad (2.4)$$

where

$$m_n\left(\mathbf{x}\right) = E\left(Y \middle| \mathbf{Y}_S, \mathbf{X}_S, \beta\right) = m(\mathbf{x}^{'}) + k(\mathbf{x}^{'})^T \Sigma_s^{-1}\left(Y_s - m_s\left(\mathbf{x}\right)\right)$$

$$s_n^2\left(\mathbf{x},\mathbf{x}^{'}\right) = Cov\left(Y(\mathbf{x})Y(\mathbf{x}^{'}) \middle| \mathbf{Y}_S, \mathbf{X}_S, \sigma^2, \gamma\right) = \sigma^2 r(\mathbf{x}-\mathbf{x}^{'}) - k(\mathbf{x})^T \Sigma_s^{-1} k(\mathbf{x}^{'})$$

and

$$k(\mathbf{x})^T = \left(c(\mathbf{x},\mathbf{x}_1),...,c(\mathbf{x},\mathbf{x}_n)\right)$$

where $\mathbf{x}^{'}$ is the new point; x and x$^{'}$ are over standardized input space $[0, 1]^d$.

For more information, the procedure of developing an emulator combining the training data following Bayesian approach is described in Kennedy and O'Hagan, 2001; Higdon et al., 2008. Separate emulators can be considered for multiple outputs. The emulator $F_n(\mathbf{x})$ is a statistical distribution which will be another GP for any input x'. A Kriging metamodel can estimate predictions from posterior Gaussian process conditional on the training dataset. This metamodel can be used as an empirical model for variance-based sensitivity analysis, Bayesian uncertainty quantification which are presented in next section.

2.2 Variance-based sensitivity analysis

In this section, the general definitions of Sobol' sensitivity indices (SIs) based on Analysis-of-Variance (ANOVA) theorem are firstly introduced, and the theoretical descriptions of two methods to calculate sensitivity index; Bayesian sensitivity analysis (BSA) and Monte-Carlo sensitivity analysis (MCSA).

2.2.1 ANOVA theorem

The Sobol' sensitivity indices are briefly introduced in this section. Readers can refer more background information in the previous study (Sobol', 1993). Suppose a mathematical model that shows the relationship between input and output by a function $Y=f(x_1, x_2, \ldots, x_k)$, with k uncorrelated input factors. Theory of variance decomposition is represented as follows:

$$V(Y)=\sum_{i}^{k}V_i+\sum_{i}^{k}\sum_{j>i}^{k}V_{ij}+\ldots+V_{12\ldots k}\ , \tag{2.5}$$

where

$$V_i=V[E_{x_{\sim i}}(Y|x_i)]\ ,$$

$$V_{ij}=V[E_{x_{\sim ij}}(Y|x_i,x_j)]-V_i-V_j\ ,$$

…,

with x_i is i-th input variable, $x_{\sim i}$ denotes all inputs except for x_i, $E(Y|.)$ is the conditional expected value, $V(Y)$ is summary of all partial variances including main variance contributions V_i and interaction variance contributions V_{ij}, …, $V_{12\ldots k}$ due to the interaction between two or more factors to the variance of Y.

All above variance contributions can be nominalized by dividing them with $V(Y)$ and defined as the sensitivity indices. Equation (1) becomes

$$S=\sum_{i}^{k}S_i+\sum_{i}^{k}\sum_{j>i}^{k}S_{ij}+\ldots+S_{12\ldots k} \tag{2.6}$$

First-order indices and total indices are commonly used for two reasons: (1) limited calculation capacity for higher-order sensitivities, (2) the ability to provide sufficiently necessary information for most concerned issues.

- First-order sensitivity index or main effect index (main SIs)

$$S_i = \frac{V_i}{V} = \frac{V[E_{x_{\sim i}}(Y|x_i)]}{V(Y)} \tag{2.7}$$

- Total sensitivity index or total effect index (total SIs)

$$S_i^T = \frac{V_i^T}{V} = \frac{E[V_{x_i}(Y|x_{\sim i})]}{V(Y)} \tag{2.8}$$

2.2.2 Monte Carlo sensitivity analysis (MCSA)

The method shown in this section was proposed by Saltelli (2002), extended by the original papers (Sobol', 1993; Homma and Saltelli, 1996). Let us consider two independent random matrices of d input variables, simplified by $\Pi_1(\alpha_1, \alpha_i, \alpha_d)$ and $\Pi_2(\beta_1, \beta_i, \beta_d)$ with i = 2:(d-1) and the size of (N, d) for each. The first-order sensitivity index in Eq. (2.6) of variable x_i can be interpreted as the reduction of output variance as x_i set constant. Therefore, Eq. (2.7) can be computed as follows:

$$S_i^{(MC)} = \frac{(1/N)\sum_j^N f(\Pi_1) f(\beta_1, \alpha_i, \beta_d) - f_0^2}{(1/N)\sum_j^N f^2(\Pi_1) - f_0^2} \tag{2.9}$$

Total sensitivity index in Eq. (2.8) represents the variability of the outputs as x_i varies and others set constant.

$$S_i^{T(MC)} = \frac{(1/N)\sum_{j=1}^N f(\Pi_2) f(\beta_1, \alpha_i, \beta_d) - f_0^2}{(1/N)\sum_{j=1}^N f^2(\Pi_1) - f_0^2}, \tag{2.10}$$

with

$$f_0^2 = \left(\frac{1}{N}\sum_{j=1}^N f(\Pi_1)\right)^2.$$

The calculation of the Sobol' indices based on random input sampling which depends on properties of random generation will have uncertainty to some degrees. MCSA thus needs to analyze convergence to gain precise results. Unfortunately, traditional Pseudo-random samples often have clusters and gaps which will slow convergence rate of SIs. Hence, Sobol' (1976) recommends using low-discrepancy (or quasi-random) sequences to enhance the rate. The method is also known as quasi-Monte Carlo. In this study, we prefer to use this sampling to enable available computation capacity.

Errors associated with SIs estimates can be evaluated using the probable error which equals to 0.6745 times the standard error (Homma and Saltelli, 1996). 95% confidence interval corresponding to 1.96 times the standard error can also be considered for more general evaluation.

$$err = 1.96\sqrt{\frac{F - I^2}{N}}, \tag{2.11}$$

with

$$F = \frac{1}{N}\sum_j^N f^2(\Pi_1) f^2(\beta_1, \alpha_i, \beta_d),$$

$$I = \frac{1}{N}\sum_j^N f(\Pi_1) f(\beta_1, \alpha_i, \beta_d).$$

Equation (2.11) is proposed for errors of main SIs. Similarly, $f(\Pi_2)$ can be used to replace $f(\Pi_1)$ in Eq. (2.11) to estimate standard errors of total SIs. In general, convergence analysis and standard error estimation are required for achieving reliable SIs results. MCSA on full models is expected to give more reliable results than BSA which is based on surrogate models.

2.2.3 Bayesian sensitivity analysis (BSA)

Calculation of Sobol' indices

Sensitivity indices including first-order indices and total indices can be computed from the posterior distributions described above considering both mean and covariance structures of the GP model. The variance of $m_n(\mathbf{x})$ in Eq. (2.4) conditional on an input of interest x_i normalized by a total variance of emulated response F_n can be used to measure first-order sensitivity index and given by:

$$\tilde{S}_i = \frac{Var_{x_i}\left[E_{x_1,\ldots,x_d}\left(F_n \mid x_i\right)\right]}{E_\Omega\left[Var_{x_1,\ldots,x_d}\left(F_n\right)\right]}, \text{ for } i = 1, \ldots, d, \tag{2.12}$$

with Ω is the probabilistic space where Gaussian process $F(\mathbf{x})$ lies.

We can consider mean and variance of a random variable $\tilde{S}_i$ for estimating sensitivity measures and their accuracy, respectively, and shown as follows;

$$\mu_{\tilde{S}_i} = \frac{E_{\Omega} Var_{x_i}\left[E_{x_1,\ldots,x_d}(F_n|x_i)\right]}{E_{\Omega}\left[Var_{x_1,\ldots,x_d}(F_n)\right]} \tag{2.13}$$

$$\sigma^2_{\tilde{S}_i} = \frac{Var_{\Omega} Var_{x_i}\left[E_{x_1,\ldots,x_d}(F_n \mid x_i)\right]}{E^2_{\Omega}\left[Var_{x_1,\ldots,x_d}(F_n)\right]}, \text{ for } i = 1, \ldots, d. \tag{2.14}$$

Similarly, an alternation of $x_{\sim i}$ in place of x_i in (2.12) can measure total sensitivity index of x_i.

Sensitivity measures can be quantified based on the posterior distributions of input parameters, and the predictive distributions of outputs through surrogate models using MCMC algorithms (Robert and Casella, 2004). The GPM/SA package developed by Los Alamos National Laboratory is adopted for constructing the emulator and estimations (Higdon *et al.*, 2008). It is noted that the emulator in this paper constructed by physical features of output simulations instead of using a reduced dimension model as described in Higdon et al. (2008). The package is modified by the authors to reach further results regarding uncertainty estimation of sensitivity indices in Eq. (2.14).

2.3 Uncertainty quantification

Two approaches to quantify the uncertainty of model parameters following Bayesian statistics are used in this study.

(1) Embed metamodeling process into a larger framework of Bayesian inference which implemented by Markov Chain Monte Carlo (MCMC) using random walk Metropolis-Hasting updates, encoded by GPM/SA software (Higdon *et al.*, 2008).

(2) Adopt complete metamodel as a basic model for Bayesian inference using enhanced algorithms of Differential Evolution Adaptive Metropolis (DREAM) (Vrugt, 2016).

Both approaches use the reduced models instead of the original models to simulate outputs from untried input settings. Some pros and cons of two approaches are as follows:

(1) ***Pros*:**

- Numerical modeling errors are accounted in complicated mathematical functions through discrepancy between model predictions and measurements.
- Enable to solve multiple variable integrations of complicated mathematical functions via MCMC.

***Cons*:**

- Convergence diagnostics of the metamodels and MCMC to obtain stable posterior distributions is unclear due to embedded modeling process of the reduced models into GPM/SA coding.
- Aleatory uncertainty due to random effect cannot be avoided.
- Computational cost is of concern for high-dimensional complicated models

(2) ***Pros*:**

- The metamodels are constructed independently before Bayesian inference process is implemented, and hence it is better to evaluate the precision of the reduced models.
- DREAM algorithm enables to run parallel chains, and hence allows multi-chain convergence diagnostics, and reduce the computational cost.
- Enable to draw samples from multi-modal, non-symmetric posterior distributions.

***Cons*:**

- High computation expense for convergence analysis of metamodels and posteriors via DREAM implementation.
- Aleatory uncertainty due to randomness effect cannot be quantified.

2.3.1 Bayesian inference using random walk Metropolis-Hasting updates

A brief description of Bayesian inference implementation from Kennedy and O'Hagan, 2000 for the univariate case and Higdon *et al.*, 2008 for the multivariate case is given in this section. The inference was implemented via MCMC using random walk Metropolis-Hasting updates. This method was applied for uncertainty quantification of uncertain input parameters on the existing base-isolated building.

At an input setting $\mathbf{x}_i$ corresponding to observations y_j (j = 1:m), with m is experiment or field measurement numbers, the observations are displayed as follows:

$$y(x_j) = \varsigma(x_j) + \varepsilon(x_j), \tag{2.15}$$

where $\varsigma(x_j)$ denotes actual responses, $\varepsilon(x_j)$ stands for observation errors. Herein, general notations of x_i and y_j signify for inputs and observations, respectively, in both univariate and multivariate cases. Input x_i can be a scalar variable or a vector of variables. The observations can be statistically modeled by the simulator $\eta(x_j)$ and the discrepancy $\delta(x_j)$ between the simulated response $\eta(x_j)$ and the reality $\varsigma(x_j)$.

$$y(x_j) = \eta(x_j) + \delta(x_j) + \varepsilon(x_j), \tag{2.16}$$

Equation 2.16 indicates that modeling error can be involved in building the relationship between the experimental observations and simulations. The discrepancy term can stem from systematic errors in modeling process such as the approximation of mathematical representations, the lack of knowledge on input values, etc. The simulator $\eta(x_j)$ can be outputs from a full model. i.e., an original parametric model, or from reduced models or metamodels. In this study, a Gaussian process or Kriging in section 2.1 is adopted to build the surrogates. The metamodeling process occurs unknown hyperparameters which can be embedded in the inference process.

The inference process is to quantify the uncertainty using Bayesian formalism. The Bayesian theorem can predict posterior distributions of model parameters by incorporating observed system responses and belief or prior knowledge (Kennedy and O'Hagan, 2000). The distributions of model parameters θ can be derived following Bayes' theorem:

$$p(\theta|\tilde{Y}) \propto p(\theta) f(\tilde{Y}|\theta), \tag{2.17}$$

the Eq. (2.17) can be normalized as:

$$p(\theta|\tilde{Y}) = \frac{p(\theta) f(\tilde{Y}|\theta)}{\int_{\Theta} p(\theta) f(\tilde{Y}|\theta)}, \tag{2.18}$$

where $p(\theta)$ and $p(\theta|\tilde{Y})$ describe prior and posterior distributions of the uncertain parameter θ, $f(\tilde{Y}|\theta)$ is likelihood estimation which quantifies the probability of the data $\tilde{Y}$ for a given value of θ, Ω is input parameter space. To rephrase, the prior $p(\theta)$ can be an informative distribution which poses less variance and better density shapes compared with noninformative one. When the parameters are nearly unknown, a uniform prior can be assumed. The likelihood density function $f(\tilde{Y}|\theta)$ can be considered as the probability of θ when the data is fixed.

To derive the posterior in Eq. (2.18), further hyperparameters associated with the modeling process need to integrate out. However, it is not realistic to integrate the posterior analytically, especially in multi-dimensional variable space. Hence, sampling methods are desired to approximate target distributions. Markov Chain Monte Carlo using random walk Metropolis-Hasting updates (Robert and Casella, 2004) is adopted to draw samples from the posterior distribution. Expected results are stable distributions which are ideally considered as pseudo-random in the target posteriors. The GPM/SA package developed by Los Alamos National Laboratory is used for this study.

2.3.2 Bayesian inference using Differential Evolution Adaptive Metropolis algorithm

A Differential Evolution Adaptive Metropolis (DREAM) algorithm proposed by Vrugt *et al.*, 2008; Vrugt *et al.*, 2009 is used in this study. The algorithm based on a simple adaptive random walk Metropolis developed by Ter Braak, 2006 with the enhancement of using subspace sampling and the correction of chain outlier to accelerate convergence rate of the posterior distributions. The DREAM algorithm has an advantage over the random walk Metropolis in section 2.3.1 at the ability of automatically tuning the scale and orientation of proposal distributions forward to the target distributions. Moreover, the DREAM also allows to parallelly running multi-chains, and hence significantly reduce computation time and improve the robustness of convergence analysis. This algorithm can solve inverse problems involving multimodality, high dimensionality, the nonlinearity of complicated dynamic models.

Let define the vector of model parameters is $\boldsymbol{\theta} = (\theta_1, \theta_2, ..., \theta_d)$ in the space of *d*-dimension. *K* Markov chains can be run parallelly. Each chain generates a vector $\boldsymbol{\theta}^{(i)}$ (*i*=1:*K*). The algorithm DREAM is briefly introduced as follows:

(1) For each chain *ith,* an initial sample is drawn from the prior distribution as a starting point for a jumping series of N iterations.

(2) Calculate model response for initial samples of multiple chains. The Bayes' theorem is applied to infer the posterior densities using the data $\tilde{Y}$. The density $p(\theta_j^{(i)} \left| \tilde{Y} \right.)$ is then attained:

$$p(\theta^{(i)} \left| \tilde{Y} \right.) \propto p(\theta^{(i)}) f(\tilde{Y} \left| \theta^{(i)} \right.),$$

where *i* denotes each chain.

(3) For next draws $\boldsymbol{\theta}_j^{(i)}$ (*j* = 2:*N*), where *N* is the total number of draws for obtaining stable posterior distributions, the proposal $\boldsymbol{\theta}_p^{(i)}$ in the chain *i*th is proposed based on a jump interval $\boldsymbol{d\theta}^{(i)}$. This interval is calculated by collecting samples from the chains in a subspace Ω of only d^*-dimensions of model parameters. The whole space is in d-dimensions of inputs as defined in section 3.1.

$$\boldsymbol{\theta}_p^{(i)} = \boldsymbol{\theta}_{j-1}^{(i)} + d\boldsymbol{\theta}^{(i)} = \boldsymbol{\theta}_{j-1}^{(i)} + \varsigma_{d^*} + (1 + \lambda_{d^*}) \gamma(\delta, d^*) \sum_{j=1}^{\delta} (\theta_\Omega^a - \theta_\Omega^b) ,$$

where

$$\gamma(\delta, d^*) = \frac{2.38}{\sqrt{2\delta d^*}},$$

and ς_{d^*}, λ_{d^*} are sampled from normal and uniform distributions, respectively; $\theta_{\Omega}^{a}, \theta_{\Omega}^{b}$ are drawn from the other chains except the *i*th chain in the subspace Ω $(a \neq b \neq i)$.

(4) Repeat the step (2) for the new candidate $\boldsymbol{\theta}_j^{(i)}$ at the *j*th iteration.

(5) Accept or reject each proposal based on Metropolis probability ratio. If P = min [1, p($\boldsymbol{\theta}_p^{(i)}$)/p($\boldsymbol{\theta}^{(i)}$)] larger than a random draw from a uniform distribution in [0, 1], then the current sample point is accepted. Otherwise, it is rejected and kept at the last accepted sample. The iteration is continued until obtaining the limiting distribution.

In general, both above methods are based on the generation of MCMC. Specifically, the DREAM is modified with the enhancements to enable to solve inverse problems involving multimodality, high dimensionality, the nonlinearity of complicated dynamic models. To sum up, two algorithms were applied on different structures to demonstrate the advantages and disadvantages of each method for simulating robust posterior distributions. The traditional MCMC was implemented to derive the posterior distributions of the uncertain inputs on the existing base-isolated building, while the DREAM was applied for the isolated bridge pier. The summary of theoretical methods applied on each structure is presented in Table 1.

Table 1. Summary of content of thesis

Chapter #	Theory	Test-bed structures
Chapter 2	Kriging metamodeling Bayesian sensitivity analysis (BSA) UQ using random walk Metropolis-Hasting updates	Isolated building
	Kriging metamodeling Monte Carlo sensitivity analysis (MCSA) UQ using DREAM	Isolated bridge pier
Chapter 3	Test-bed structures	Isolated bridge pier Isolated building
Chapter 4	Bayesian sensitivity analysis (BSA)	Isolated building
Chapter 5	Monte Carlo sensitivity analysis (MCSA)	Isolated bridge pier
Chapter 6	UQ using random walk Metropolis-Hasting updates	Isolated building
	UQ using DREAM	Isolated bridge pier

Chapter 3

Test-bed structures

Two seismically isolated structures, an existing base-isolated building and an isolated bridge pier following Japan specification of highway bridges are introduced. The choice of these structures is motivated by the ability to consider sensitivity evaluations and uncertainty quantification for different sorts of the structures under various earthquakes. Moreover, a collection of available measured data is advantageous to assess the safety of existing structures which is objective in this study. In this chapter, description of seismic input data, observed data, and the configuration of the base-isolated building and the isolated bridge pier are introduced. Numerical modeling and seismic response analysis are then presented.

3.1 Seismic input data

Three large earthquakes with different characteristics in magnitude and frequency content including Great East Japan (Tohoku) earthquake on 11th March 2011, Mid-Niigata earthquake in 23rd October 2004, and Kobe earthquake in 16th January 1995 are used in this study. Earthquake information including station site, direction, moment magnitude, JMA seismic intensity, epicenter depth, peak ground acceleration (PGA), and occurred time and location of these large earthquakes are shown in Table 2. The Great East Japan earthquake is an undersea megathrust type off the coast of Japan that has a moment magnitude of 9.1 and JMA intensity of less than five at record site of Shibaura Institute of Technology. Kobe or Great Hanshin earthquake has a strike-slip mechanism with M.w. 6.9, JMA intensity of 6.5 at the site of Japanese Railway Takatori station. Mid-Niigata earthquake has reverse fault type with M.w. 6.8 and JMA intensity of 6.2 at Tohkamachi site. Those data are collected from K-NET/ /National Research Institute for Earthquake Science and Disaster Prevention, Japan.

Elastic response spectra and standard design spectra for three large earthquakes recorded at stations are discussed. Figure 3.1 shows that Tohoku earthquake has a dominant frequency range of 0.7-1.4s with a peak value of 1s. While Kobe earthquake dominates in a wide range of 0.1-2.5s period with a peak value at 1.25s, Mid-Niigata earthquake has low vibration period in a predominant range of about 0.03-0.7s with a

peak value of 0.22s. These spectra are computed for elastic systems with 5% damping. Standard design response spectra are figured out by smooth designs of seismic performance level 2 for two ground motion types I and II and three soil classifications, stiff, medium, and soft conditions. Those standards are defined in Japan Specifications for Highway Bridges, part V Seismic Design by Japan Road Association 2012 (JRA, 2012). Level 2 consists of two design ground motion types, type I for interplate-type earthquakes and type II for inland-nearfield-type earthquakes. Type II is applied for Mid-Niigata and Kobe earthquakes that are near-field earthquakes, type I is for Tohoku earthquake that is a far-field earthquake. Table 3 summarizes soil conditions and design ground motion types applied. Figure 3.1 (a) indicates that the acceleration response of Tohoku earthquake is far below the designed spectrum termed by Level 2-Type I-Group 2/Group 3. Considering Kobe earthquake, the spectral response is relatively consistent with the smooth line defined by Level 2-Type II-Group 3 in general, as shown in Fig. 3.1 (b). The spectrum of Mid-Niigata earthquake implies stiff soil condition at the site of record. This very large earthquake may cause severe damage for structures having a low period of smaller than 0.22 s or higher frequency of 4.5 Hz since the performance of spectral design standard (Level 2-TypeII-Group 1) is far lower than its spectral response, see Fig. 3.1 (b). To sum up, structures having fundamental natural frequencies out of the range of ground motion deems to suffer less damage or no damage than the ones that two frequency ranges coincide.

Figure 3.2 depicts acceleration time history and its Fourier transfer for three earthquakes. The excitation duration of Mid-Niigata, Kobe, and Tohoku earthquakes are 30s, 40s, and 600s, respectively, with peak ground acceleration (PGA) for each given in Table 2. The maximum ground acceleration of these three earthquakes reaches 1715, 599, and 168 cm/s^2 at 6, 7 and 132 s, respectively. Figure also points out predominant frequency ranges for three large earthquakes. Fourier transfer points out different predominant frequency ranges, 3.5-5 Hz, 0.47-1Hz, and 0.7-1.3Hz for Mid-Niigata, Kobe, and Tohoku earthquakes, respectively.

Table 2.Characteristics of large ground motions

Earthquake	Station site	Direction	Moment Magnitude (Mw)	JMA seismic Intensity	Epicenter Depth (km)
Great East Japan, 2011 (Tohoku)	Shibaura Institute of Technology	EW, N-S, U-D	9.1	5-	24
Mid-Niigata, 2004	Tohkamachi	N-S	6.8	6.2	21
Kobe, 1995	JR Takatori	N-S	6.9	6.5	17.9
Earthquake	Date and Time (JST)	Source Coordinate		PGA (gal)	
Great East Japan, 2011	2011/03/11, 14:47	38.103N, 142.860E		168	
Mid-Niigata, 2004	2004/10/23, 17:56	37.128N, 138.74E		1715	
Kobe, 1995	1/16/1995, 20:46	34.594N, 135.012E		599	

Note: E-W, N-S, U-D are East-West, North-South, Up-Down directions, respectively.

Table 3. Ground motion types and soil conditions at record sites

Earthquake	Ground motion type	Soil condition	Soil property
Great East Japan, 2011 (Tohoku)	Interplate far-field (type I)	Group 2, 3	Medium/Soft soil
Niigata, 2004 (Tahkamachi)	Near-field (type II)	Group 1	Stiff soil
Kobe, 1995 (Takatori)	Near-field (type II)	Group 3	Soft soil

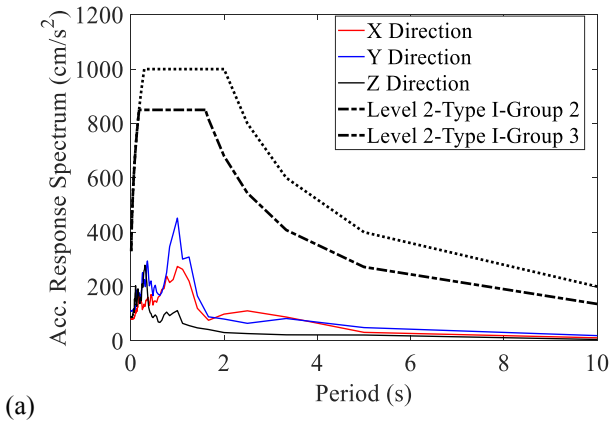

(a)

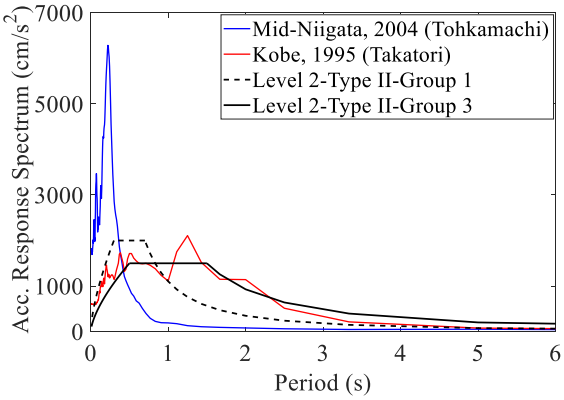

(b)

Fig. 3.1 Response acceleration spectra of original ground motions (a) 3 directions X, Y and Z of Tohoku earthquake, (b) the N-S component of Mid-Niigata and Kobe earthquake at record sites.

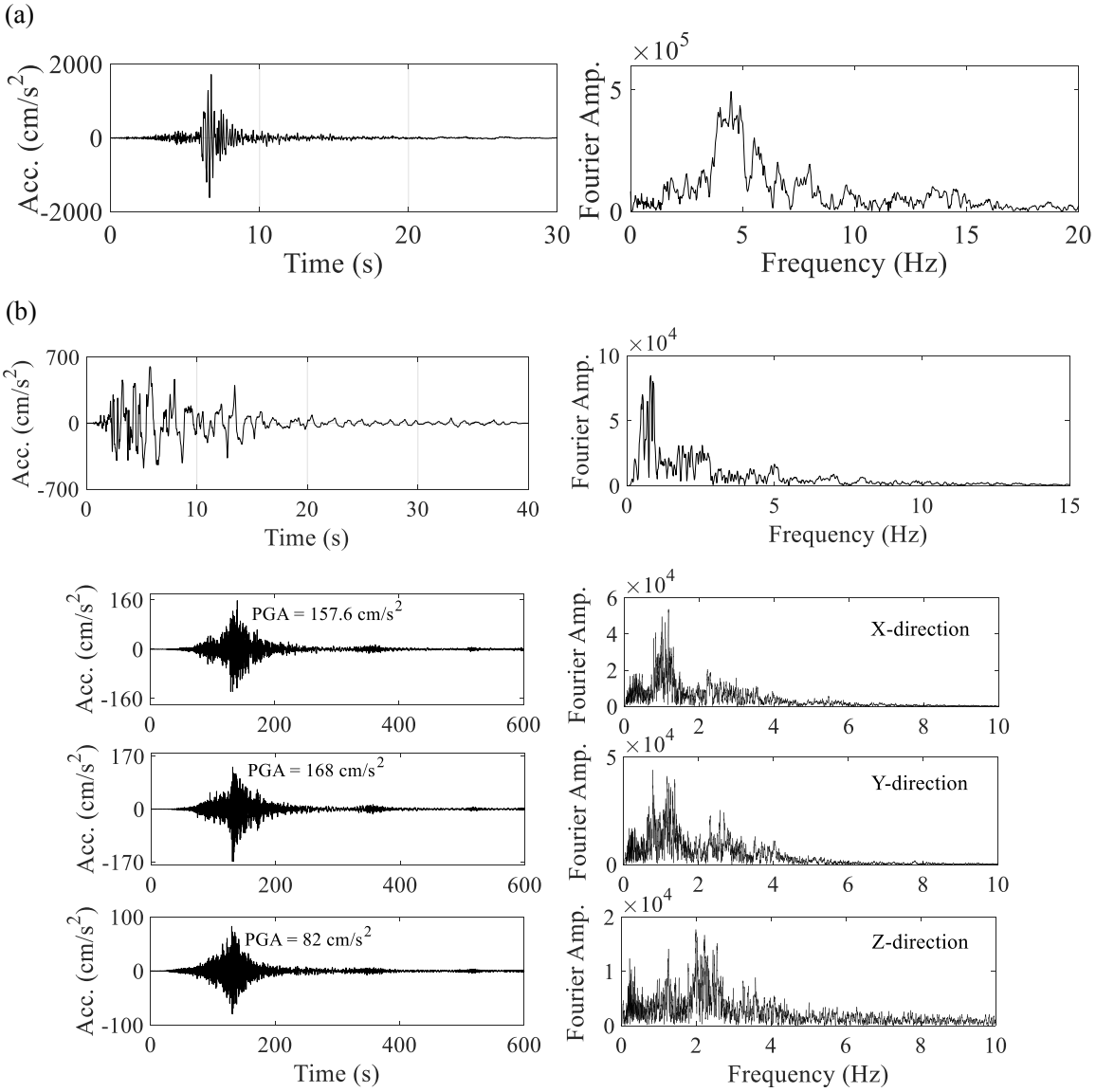

Fig. 3.2 Acceleration time history and its Fourier transfer of (a) Mid-Niigata earthquake, (b) Kobe earthquake, (c) Tohoku earthquake.

3.2 Existing base-isolated building

An existing base-isolated asymmetric building located in Tokyo Bay area, Japan is described in this section. A large-scale sensor network has been installed since 2005 and has acquired seismic response data including the response in the Great East Japan Earthquake, occurred off the Pacific Coast of Tohoku zone in March 11, 2011 (Nishikawa et al., 2014). For seismic response analysis of the existing building, the authors basically followed previous studies by Siringoringo and Fujino (2014), (2015) to explain the interest structure, installed a monitoring system, dynamic properties, and modeling. We then conducted additional analyses by applying the system identification method and developing transfer functions to predict error sources between recorded and simulated results of the building under various shaking levels.

3.2.1 Building description and data acquisition

The existing building is an L-shaped reinforced concrete base-isolated building with the main structure made of braced steel frames. The building consists of two parts: a 7-story building (building B) and a 14-story building (building C) connected by common elevator shaft and paths. A vertical opening in the middle of building C from the 2nd floor to 7th floor divides it into two sections named section Ca and section Cb, as shown in Fig. 3.3 (a), (b). All parts of the building are connected by a unique concrete slab placed on the top of the base isolation system. The base isolation system consists of a total of 146 isolators and dampers units: 59 natural rubber bearing (NRB) units, 26 sliding bearing (SB) units, 28 lead damper (LD) units, and 33 U-shaped steel dampers (SD) units.

In 2011, the huge earthquake with Mw 9.0 off the Pacific Coast of Tohoku zone attacked North-eastern Japan (hereafter referred to as the main shock). At the site of the base-isolated building in Tokyo, the peak ground acceleration (PGA) recorded 157.6 gal in the X direction and 167.9 gal in the Y direction. Before and after the main shock from 2010 to 2012, there were five large earthquakes with PGA from 25 to 160 gal, and many small events including aftershocks less than 25 gal. Note that the building survived in the main shock without visible structural damage. The high-density seismic monitoring system provides 3-axis accelerations of the superstructure and the basement, and the relative displacements of the base-isolation floor with the sampling frequency of 100 Hz. The locations of sensors are illustrated in Fig. 3.3 (c). The system successfully recorded more than 140 earthquakes for 3 years from 2010 to 2012. The detail of the seismic monitoring system is given in the literature (Nishikawa et al., 2014).

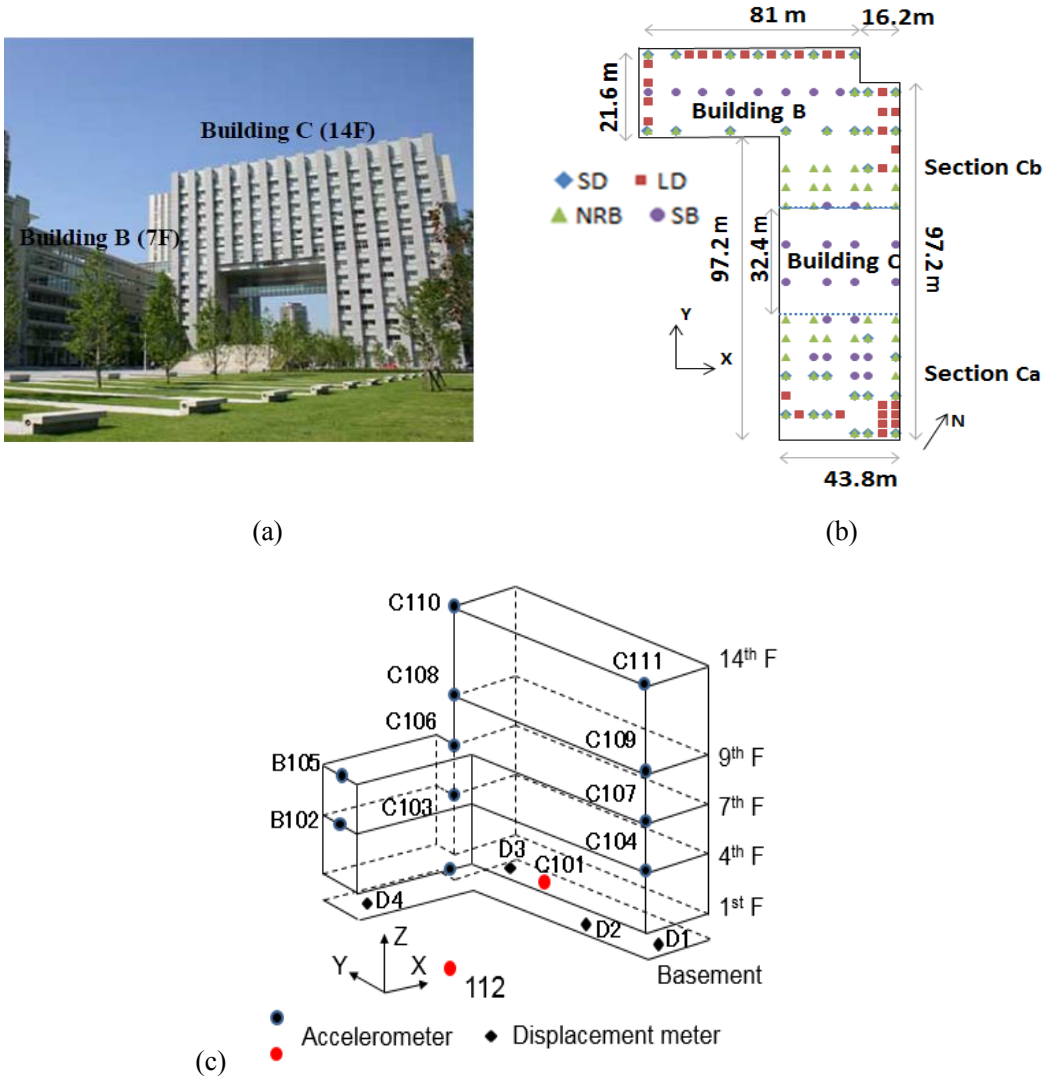

Fig. 3.3 The base-isolated building and the monitoring system: (a) the building, (b) layout of the isolation system, (c) sensor layout.

3.2.2 Long-term variability of resonant mode characteristics

System identification

Here, the MIMO time-variant SRIM system identification (Juang, 1997) was adopted to extract the resonant modes from each earthquake record. The system identification of the target structure was successfully performed by the same method by Siringoringo and Fujino (2015). We first identified the first three resonant modes of the building by applying the SRIM method to records of the main shock, as shown in Fig. 3.4. Here, the first mode is the translational mode that has a large horizontal modal displacement at the isolator layer and smaller modal displacement at the upper structure, identified at about

0.45-0.58 Hz. Although the base isolation system functions well at the first mode, Fig. 3.4 also indicates large displacements of upper floors. It is because the building has an asymmetric geometry which can amplify the response of the upper structure. The second and third modes are torsional responses with large modal displacements at the corner of building Cb in a range of 0.58-0.68 Hz and building B from 0.68 to 1 Hz respectively. Similarly, frequency ranges of the first mode, the second mode, and the third mode for small earthquakes were approximated at 0.55-0.5 Hz, 0.7-0.8 Hz, and 1.1-1.2 Hz, respectively.

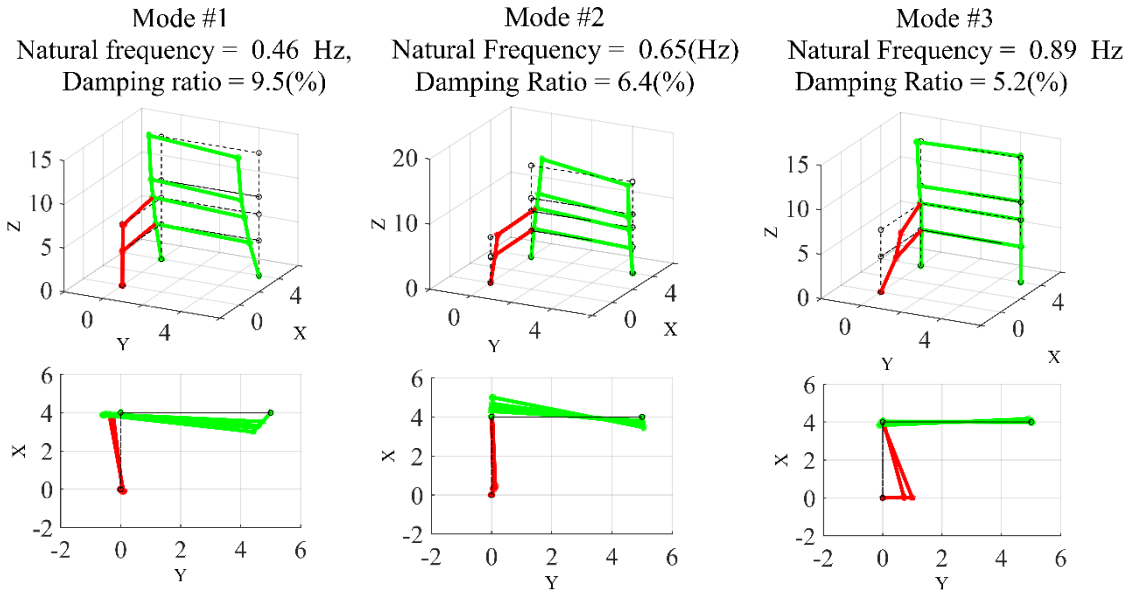

Fig. 3.4 First three mode shapes of the base-isolated structure under the main shock produced from the SRIM system identification.

Variability of resonant frequencies during the long-term data observation

Sequential variability of resonant frequencies of the first three modes during the long-term earthquake observation is shown chronologically in Fig. 3.5. A set of 42 earthquakes including 10 events before the main shock and 31 events after the main shock was used to investigate the variability. The response of one event can be divided into time segments of 50s each. For instance, considering the first mode under the main shock on March 11, 2011, the resonant frequency starts from a low value at the beginning of the excitation and increases gradually towards the end. Figure 3.5 reveals that the frequencies of the first three modes under events after the main shock are generally lower than those before the main shock. The decrease in the frequencies of events after the main shock is clearest in mode #3 and less explicit in mode #1. Figure also indicates that the first mode's frequency can recover after four months from the main shock in comparison with its value

before the shock. It is because a stiffness reduction due to Mullin's effect of base isolators has a temporary and recoverable characteristic in modulus under strain cycling of rubber isolators. This can be demonstrated in section 3.2.4. However, the recovery does not happen to mode #3 which signify the torsional response of the superstructure. Hence, it is predicted that there was the possibility of structural changes inside the superstructure, especially large displacement parts in mode #3.

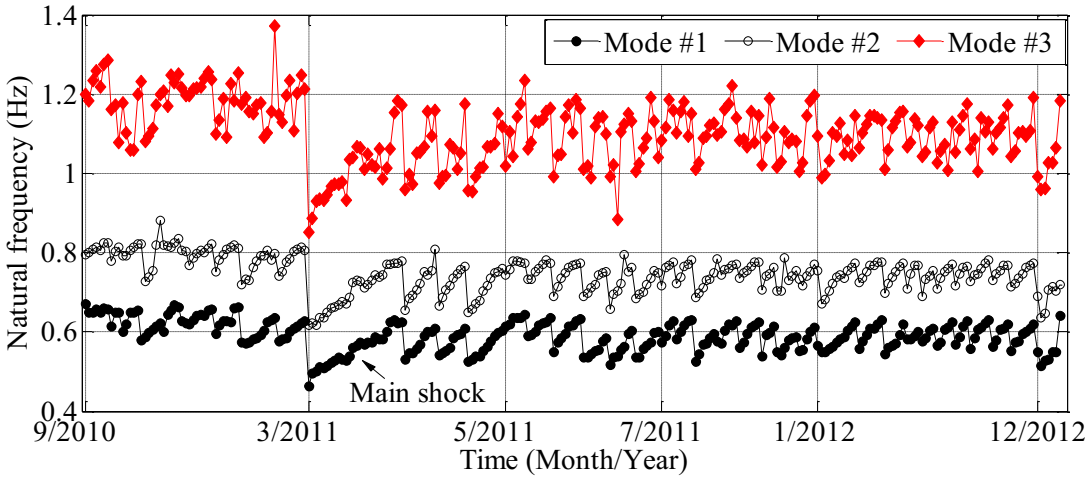

Fig. 3.5 The long-term sequential variability of dominant frequencies corresponding to the first three modes of the building over time.

3.2.3 Numerical model verification

Modeling

The numerical model of the target base-isolated building, which the authors used in this study, was the one constructed in the previous study by Siringoringo and Fujino (2014). The building consists of 26 floors and one rigid base slab. Here, 81 degrees of freedom (DOF) were adopted to construct a lumped-mass model as shown in Fig. 3.6 (a). The general formula of the motion equation can be described by the following formula:

$$\mathbf{M\ddot{u} + C\dot{u} + Ku} = \mathbf{-MR}(\ddot{\mathbf{u}}_{\mathbf{b}} + \ddot{\mathbf{u}}_{\mathbf{g}}) \tag{3.19}$$

where **M** is a diagonal mass matrix of the structure, **C** is the damping coefficient matrix, **K** is the stiffness matrix, and **R** is input influence coefficient matrix. Denotations $\ddot{\mathbf{u}}$, $\dot{\mathbf{u}}$, and **u** present floor acceleration, velocity and displacement vectors relative to the base, $\ddot{\mathbf{u}}_{\mathrm{b}}$ is a base acceleration vector relative to the ground, $\ddot{\mathbf{u}}_{\mathrm{g}}$ is ground acceleration vector. Stiffness **K** and mass **M** were constructed based on design parameters while damping ratios ξ, which was used to construct the Rayleigh damping matrix **C**, was assumed to be 0.02 for the superstructure and 0.05 for the base. For base isolation units, bilinear models were applied to calculate the first stiffness and the second stiffness for each. The stiffness matrix of the base was approximated as the summary of the stiffness of all isolator units in each of *X*, *Y*, *Z* direction-oriented following to the building's main directions.

Numerical calculations were conducted for some significant earthquake inputs, large and small earthquakes, for validating the model. Figure 3.6 (b) shows a good agreement between the numerical output and the recorded data in both time domain and frequency domain under the main shock. The small discrepancy between simulation results and measurements can be considered as acceptable errors because of the complexity of the real structure and the assumed simplification of the numerical model. However, there is not good agreement in the response of small earthquakes before and after the main shock especially in the frequency range of 0.7-1.2 Hz, for example in Fig. 3.6 (c). This specified frequency range dominates the torsional responses of the building. The model can hence be updated through response analysis of the superstructure modes.

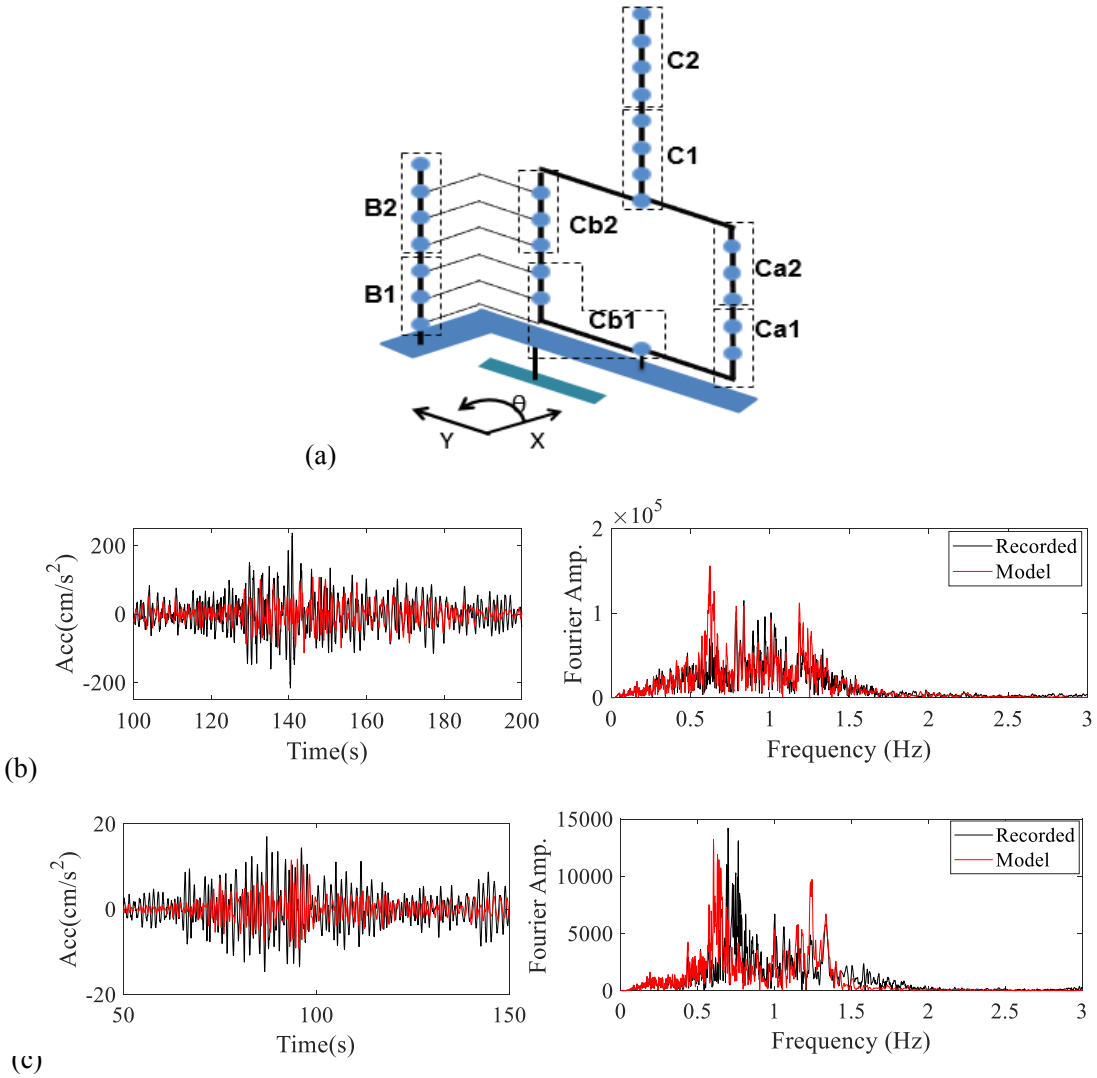

Fig. 3.6 (a) 3D lumped-mass model of the base-isolated building; dynamic performances of the structure overlayed between simulated and recorded accelerations of sensor C110 in X-direction under (b) the main shock on March 11, 2011, and (c) the foreshock on March 9, 2011.

Prediction errors under various earthquakes

This section considers the relationship between the percentage of RMSE of normalized prediction errors regarding response accelerations and PGA of a variety of earthquakes with different intensities. A set of 93 earthquakes including 26 foreshocks, 66 aftershocks, and one main shock on March 11, 2011, was chosen to develop this relationship. The percentage of RMSE is defined as follows:

$$RMSE(\%) = \sqrt{\frac{1}{N}\sum_{i=1}^{N}\left(\frac{X_{i\,\mathrm{model}} - X_{i\mathrm{data}}}{X_{i\mathrm{data}}}\right)^2} \times 100\ , \tag{3.20}$$

where $X_{i\text{model}}$ is numerically calculated acceleration, $X_{i\text{data}}$ is recorded acceleration. Figure 3.7 points out that there is a tendency that larger earthquakes give smaller RMSE. Large RMSE are found in small earthquakes, especially events after the main shock. Moreover, even small earthquakes with same PGAs also give a wide range of various RMSE percentages. Therefore, error sources causing this should be clarified, and the model of the existing structure needs to be updated with time.

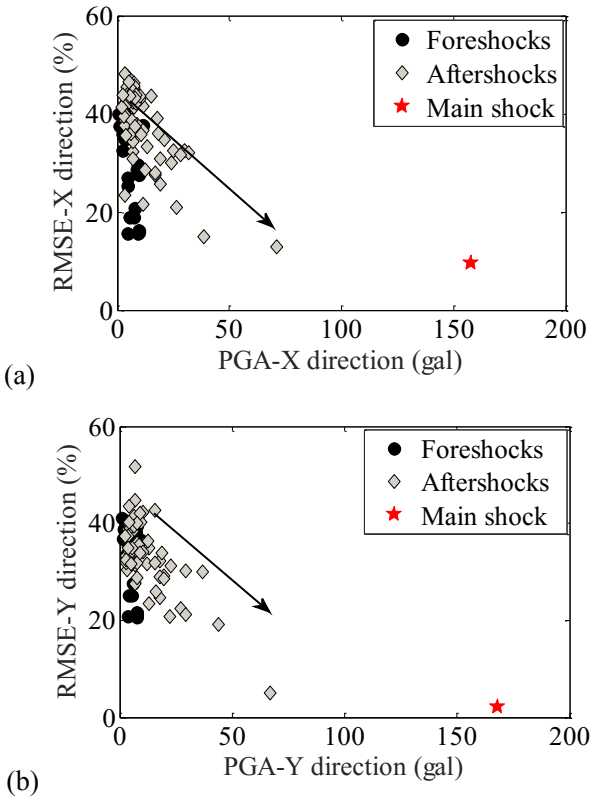

Fig. 3.7 The relationship between peak ground acceleration (PGA) and RMSE (%) of the prediction errors between simulated and recorded accelerations of (a) sensor C111 in X-direction and (b) sensor B105 in Y-direction under various earthquakes.

3.2.4 Detail analysis of structural property changes

In this section, an explicit investigation of structural property changes was implemented by developing the transfer functions in terms of floor accelerations and the variability analysis of equivalent effective stiffness of the isolation system over time.

Transfer functions of the superstructure

The transfer functions represented transfer ratios between specified floors of the building, i.e., the ratios between the top and the 4th floor, the 4th floor and the upper base layer of building B; the top and the 9th floor, the 9th floor and the base layer of building C, with respect to translational floor accelerations on their respective weak axes. Spectra of transfer functions were constructed by a set of 65 recorded earthquakes before and after the main shock from 2010 to 2011. Most of these events were small earthquakes. The set was divided into two subsets including 25 foreshocks and 40 aftershocks. Their performance analysis can be conducted through evaluating mean and standard deviation, as shown in Fig. 3.8. Figure shows that the transfer functions of seismic forces from the ground to upper floors decreases following floors' height development. The lower floors have clear peaks with higher transfer ratios than the ones of upper floors in their dominant torsional frequency ranges. By comparing the magnitudes of these peaks, Fig. 3.8 also indicates that the transfer ratios of the aftershocks were higher than the ones of the foreshocks. That is, the behavior of the structure in the aftershocks became more flexible than they were in the foreshocks. It thus can be concluded that there was the possibility of structural stiffness reduction after the main shock. These results were consistent with the previous indication in section 3.2.2 as considering the long-term changes of the modal responses.

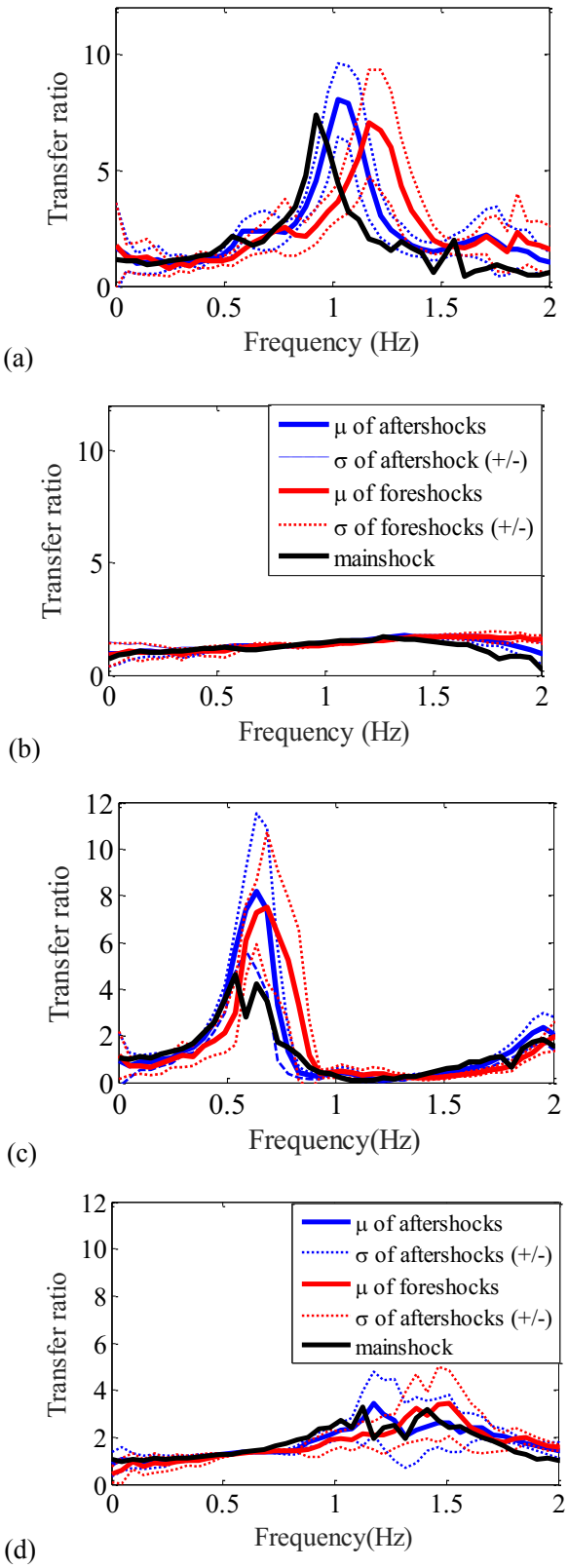

Fig. 3.8 Transfer functions of floor accelerations: (a), (b) the 4th floor/ the upper base layer and the 7th floor/ the 4th floor of building B; (c), (d) the 9th floor/ the upper base layer and the 14th floor/ the 9th floor of building C, respectively.

The equivalent stiffness of isolators over time

An approximation of equivalent stiffness through recorded accelerations and displacements was conducted to assess the possibility of the stiffness changes of the isolation system after the main shock. The force-deformation relationship of the system can be approximated through the equivalent hysteretic loops of the accelerations and the displacements. The equivalent stiffness was calculated through the ratio between the discrepancy of maximum and minimum accelerations and that of respective displacements, simply illustrated by the straight line on the hysteretic loop of a natural rubber bearing, as shown in Fig. 3.9 (a). The variability of the approximated effective stiffness of the isolation system over time is shown in Fig. 3.9 (b). The stiffness decreases gradually from the foreshock on February 5, 2011, towards the lowest value at the main shock on March 3, 2011 and recovers again on July 15, 2011. The recovery happened in 4 months after the main shock. The delay can be explained to be due to the stiffness reduction of isolator devices as a characteristic of Mullin's effect. The Mullin's effect is known as the property of temporary and recoverable reduction in modulus under strain cycling of rubber isolators. The delay is understandable to be because consecutive events after the main shock caused a prolonged effect on the effective modulus recovery of the isolators.

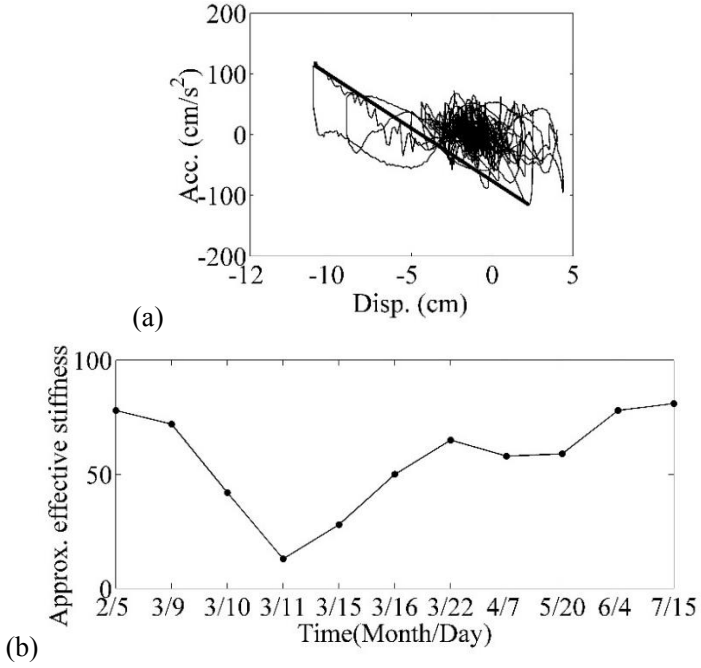

Fig. 3.9 (a) The hysteretic loop of a natural rubber bearing located at the base of building Cb under the main shock, (b) approximated effective stiffness of the base-isolated system for earthquakes in 2011.

3.3 Seismically isolated bridge pier

The test-bed structure is a seismically isolated bridge pier based on Japan design specifications of highway bridges (JRA, 2012). This structure is commonly used for verifying the applicability of seismic isolation techniques in Japan. In this study, it is used for analyzing and quantifying the uncertainty of numerical models under structural change conditions subjected to seismic excitations. This section presents modeling process, nonlinear seismic response analysis of the bridge under different earthquake characteristics, artificial monitoring data supply.

3.3.1 Seismic input data

Input ground motion for nonlinear seismic analysis for the seismically isolated bridge pier is records from 1995 Kobe earthquake Mw 6.9 at JR Takatori station with 40s duration and 2004 Mid-Niigata earthquake at Tahkamachi station. These two earthquakes have different magnitude and frequency content as presented in section 3.1. Kobe earthquake has PGA of 600 gal dominated in the range of 0.47-1 Hz while Mid-Niigata earthquake has PGA of 1715 gal with the high-frequency range of 3.5-5 Hz. The N-S component of these earthquakes was adopted to excite the bridge in its longitudinal direction.

For examining input parameter sensitivity, 20 levels of earthquake magnitudes corresponding to 20 percentage scales of the real time-history records was assumed for both Kobe and Mis-Niigata earthquakes, see Table 4. Different scales were designed to have approximately equal magnitudes for the sake of comparison of parameter sensitivity under varying seismic characteristics. Herein, seismic magnitudes are considered by peak ground acceleration (PGA).

Spectral acceleration response of various levels of Kobe and Mid-Niigata ground motions are shown in Fig. 3.10, Fig. 3.11. Type 2-Type II-Group 3 stands for Kobe earthquake under the soft soil condition. Mid-Niigata earthquake measured at Tahkamachi site is categorized for Type 2-Type II-Group 3 in Japan design specifications of highway bridges (JRA, 2012). Figure 10 indicates that the spectra of earthquake levels owning PGA of larger than 480 gal are over the design standard. These seismic levels are more susceptible to be damaged. Similarly, the response spectra of Mid-Niigata earthquake levels, shown in Fig. 3.11, points out that earthquakes with PGA more than 500 gal are susceptible to be damaged than the ones under the smooth line. Collapsed structures subjected to very large earthquakes can be ignored in SA due to practical usage.

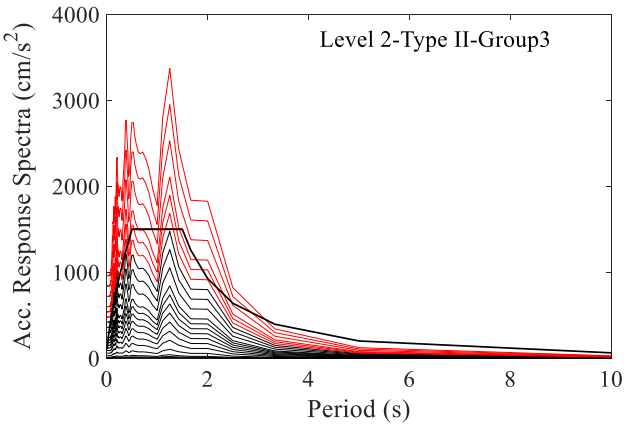

Fig. 3.10 Spectral acceleration of Kobe earthquake recorded at Takatori station. Red lines define earthquake levels with PGA > 480 gal, black lines are earthquake levels with PGA < 420 gal, Level 2-Type II-Group 3 termed the design spectrum of the inland-nearfield earthquake at soft soil site.

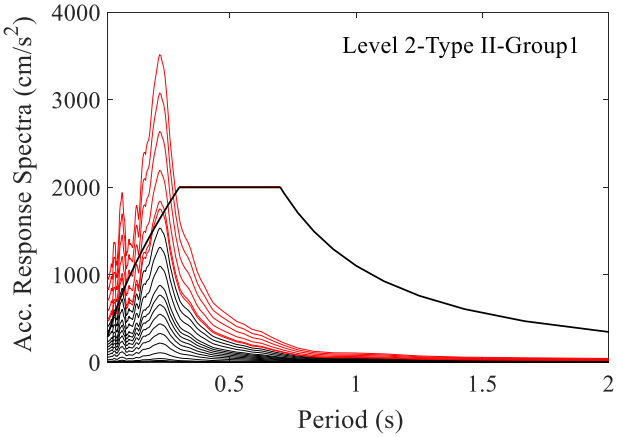

Fig. 3.11 Spectral acceleration of Mid-Niigata earthquake recorded at Tahkamachi station. Red lines define earthquake levels with PGA > 503 gal, black lines are earthquake levels with PGA < 480gal, Level 2-Type II-Group 1 termed the design spectrum of the inland-nearfield earthquake at stiff soil site.

Table 4 Earthquake scales by percentages of the original ground acceleration.

PGA (cm/s^2)	Kobe earthquake, scale (%)	Mid-Niigata earthquake, scale (%)
3	0.5	0.17
6	1	0.35
12	2	0.7
30	5	1.75
60	10	3.5
90	15	5.25
120	20	7
150	25	8.74
180	30	10.5
210	35	12.2
240	40	14
300	50	175
360	60	21
420	70	24.4
480	80	28
503	90	29.3
600	100	35
720	120	42
840	140	49
960	160	56

Table 5 Configuration of the isolated bridge pier

Member	Component	Value
Superstructure	Span (mm) x the number of spans	40000 × 5
	Mass (ton)	604
RC pier	Section (mm x mm)	5000 × 2200
	Height (mm)	10000
	Mass (ton)	346.3
Isolator (LRB)	Section (mm x mm)	600 × 600
	Total thickness of LRB (mm)	154
	Diameter (mm) and the number of lead plugs	85 × 4

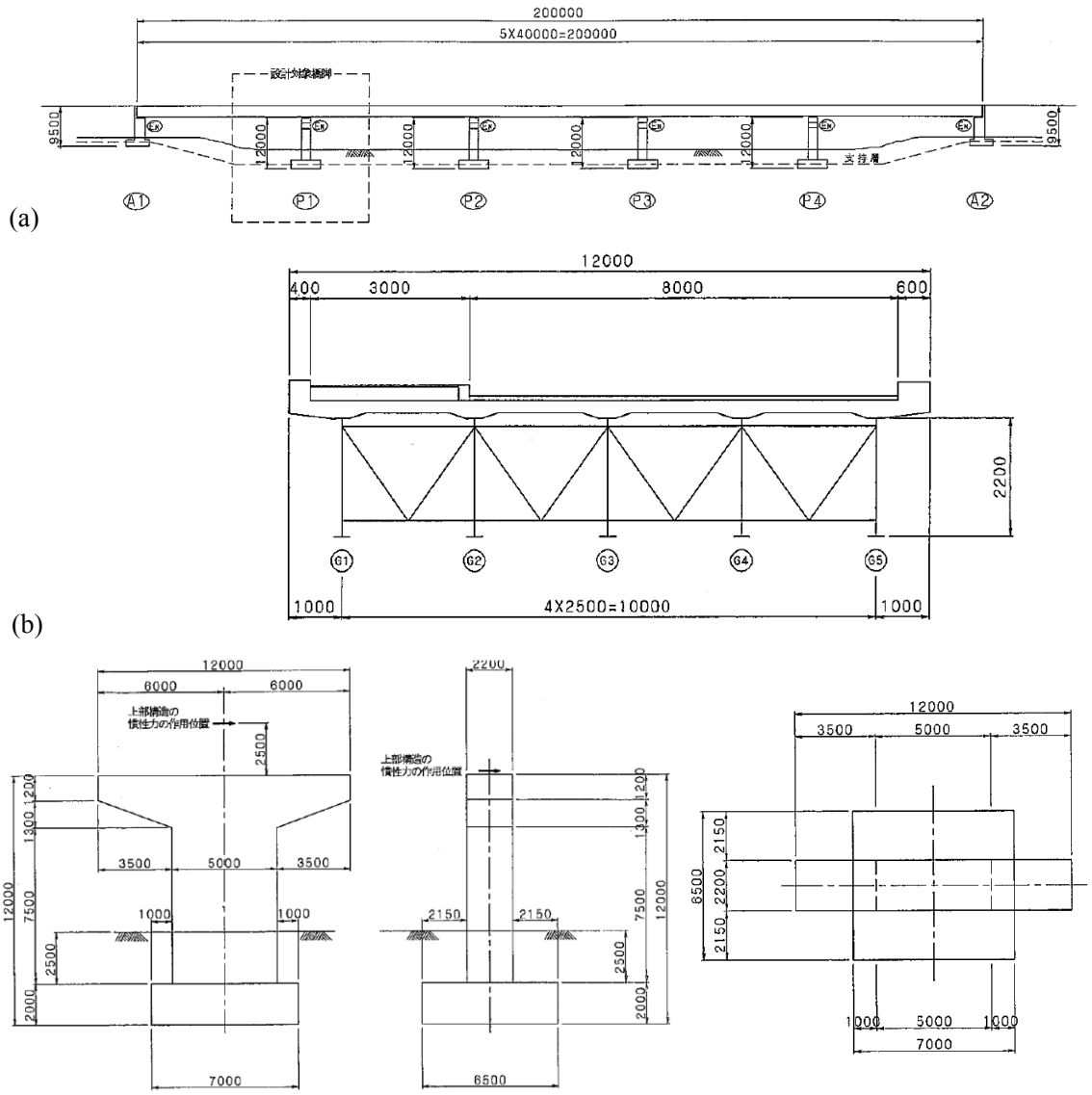

Fig. 3.12 Configuration of the isolated bridge pier (unit: mm): (a) side view of the longitudinal direction bridge, (b) cross-section of the superstructure, (c) front view, side view, and plan view of the pier in the order from left to right.

3.3.2 Description of the seismically isolated bridge pier

The design of the target seismically isolated bridge pier is based on Japan design specifications and bearing manual of highway bridge (JRA, 2012)(JRA, 2004), as shown in Fig. 3.12. The structure consists of reinforced concrete pier, steel girders and five laminated lead rubber bearings (LRB) at the top of a pier, as shown in Table 2. Figure 3.12 (a) shows longitudinal direction view or side view of the bridge including five spans with 40 m for each. The total length is 200m. The height of each column is 10 m, one of abutments is 8.15 m, the foot height of columns is 2 m. Figure 3.12 (b) and (c) show the cross-section of the superstructure and the pier, respectively.

3.3.3 Numerical modeling of the RC bridge pier and seismic isolation bearing

A numerical analysis is crucially required for sensitivity analysis and uncertainty quantification. The isolated bridge pier was modeled as a 2-DOF lumped mass system. The force-deformation relationships of isolators and pier were idealized by hysteresis loops using a Takeda hysteresis model (Takeda, Sozen and Nielsen, 1970) and a bi-linear model, respectively, as shown in Fig. 3.13. Takeda model is broadly used in the nonlinear seismic analysis of reinforced concrete structures. In this study, a modified Takeda model with the unloading stiffness degrading parameter, $\alpha = 0.3$; and the reloading parameter, $\beta = 0.6$ was chosen. These parameters directly influence the Takeda loop shape, i.e., energy dissipating capacity of seismic pier responses. Based on previous experiments (Tyler and Robinson, 1984), (Robinson, 1982), the bilinear model is suitable for approximating hysteresis loop of the lead rubber bearing. A Newmark-beta method incorporating Newmark Raphson iterations was used to integrate numerically 2-DOF motion equations with 0.001s time increment. Here, Rayleigh damping was applied with the assumption of 2% and 0% for damping ratios of the pier and isolators, respectively. In numerical integration process, the stiffness of the bearing and pier is updated for each time step. Numerical results deem to be accurate since the time increment taken small enough that is smaller than one-tenth of the highest fundamental natural period of the bridge. The detailed presentation of modal analysis will be presented later in this subsection. The integration time increment is also smaller than the time interval of the input ground motion records of Kobe and Mid-Niigata earthquakes.

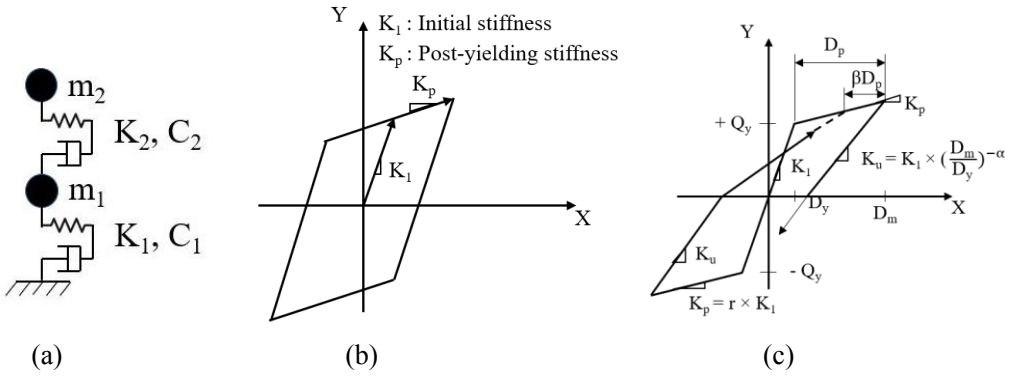

Fig. 3.13 Hysteresis loops of the isolators and the bridge pier approximately modeled by (a) 2-DOF isolated bridge pier (b) bi-linear model, (c) Takeda degrading model (K1, first stiffness; Kp, post-yielding stiffness; Ku, unloading stiffness; Dy, yield deformation; Dm, max deformation; Dp, plastic deformation; α, unloading stiffness degrading parameter; β, reloading parameter; r, ratio between post-yielding stiffness and initial stiffness; Qy, yield force).

3.3.4 Nonlinear seismic response analysis under original earthquakes

The nonlinear response analysis of structural elements of the isolated bridge pier was conducted under two earthquakes with different seismic characteristics, Kobe earthquake with the dominant frequency in 0.47-1 Hz and high-frequency Mid-Niigata earthquake in the range of 3.5-5 Hz. Figure 3.14 shows acceleration time-history and its Fourier transfer of the pier and superstructure under Kobe earthquake. The peak accelerations of the pier and superstructure are 870 cm/s^2 and 981 cm/s^2 at 3s and 6s, respectively. The overlay time-history between the acceleration of the pier and superstructure indicates the longer period response of the isolators than that of the pier. The seismically isolated function of the isolators was well-engaged with no critical time lag between their response and the ground motion during the earthquake. Dominant frequencies of the pier and isolators are nearly 2.7 Hz and 0.8 Hz, respectively. Figure 3.15 shows acceleration time-history and its Fourier transfer of the structural components under Mid-Niigata earthquake. The peak accelerations of the pier and superstructure are 2583 cm/s^2 and 1780 cm/s^2 at 3s and 6s, respectively. The response acceleration of the pier reaches 2583 cm/s^2 that is nearly one and a half times than the one of the superstructures. Moreover, the excitation period of these components is almost the same to each other. The isolation system is concluded to be not well-functioned under Mid-Niigata earthquake.

Fundamental natural frequencies of the structure are 1.08 Hz and 3.3 Hz corresponding to the 1st mode and second mode of the structure, as shown in Fig. 3.16. These free vibration frequencies were calculated using the initial stiffness of the pier and superstructure. The two frequencies are in the predominant range of Kobe earthquake but are lower than the one of Mid-Niigata earthquake. The effect of these two earthquakes can be indicated via nonlinear response models of the pier and isolators in Fig. 3.17.

Although PGA of Mid-Niigata earthquake is mostly more three times than the one of Kobe earthquake at station sites, relative displacement of the pier with the ground and the isolators with the pier under Kobe earthquake is much larger than under Mid-Niigata earthquake. It is recognized that large earthquakes with a high-frequency range that is out of the range of the structure may cause little effect on the structure.

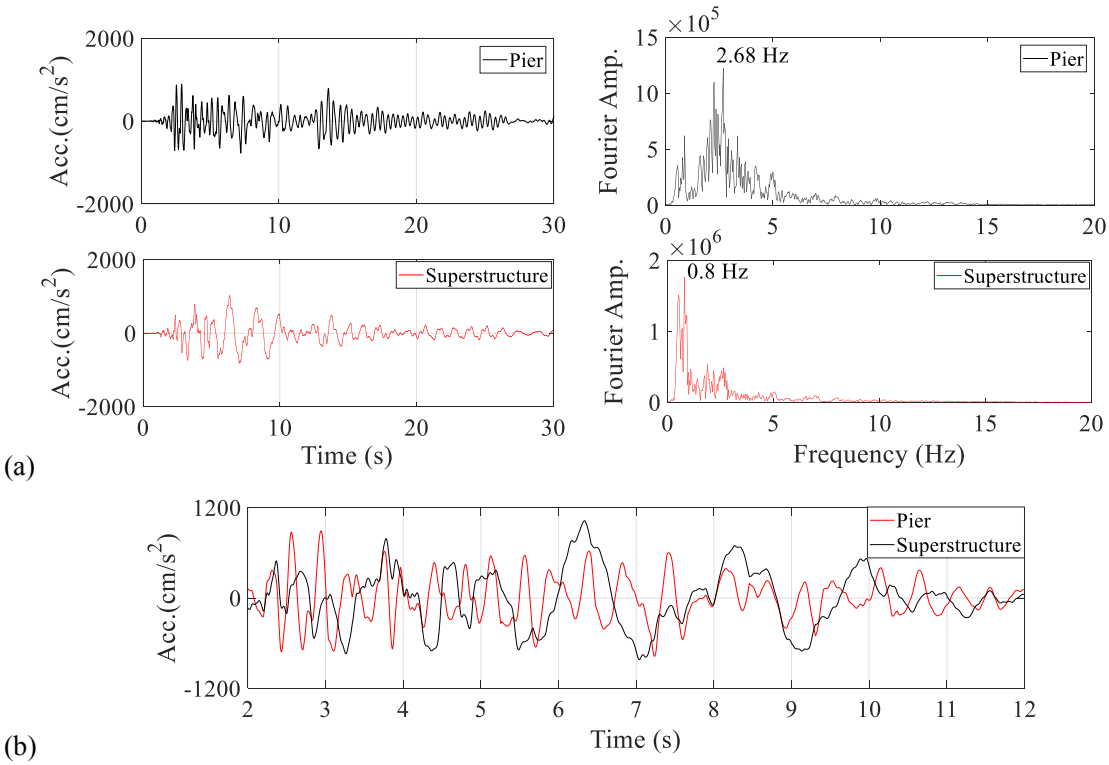

Fig. 3.14 Simulated response time histories and Fourier transfer of acceleration during Kobe earthquake; (a) 30s full-time duration of excitation, (b) enlarged time-history from 2 to 12s.

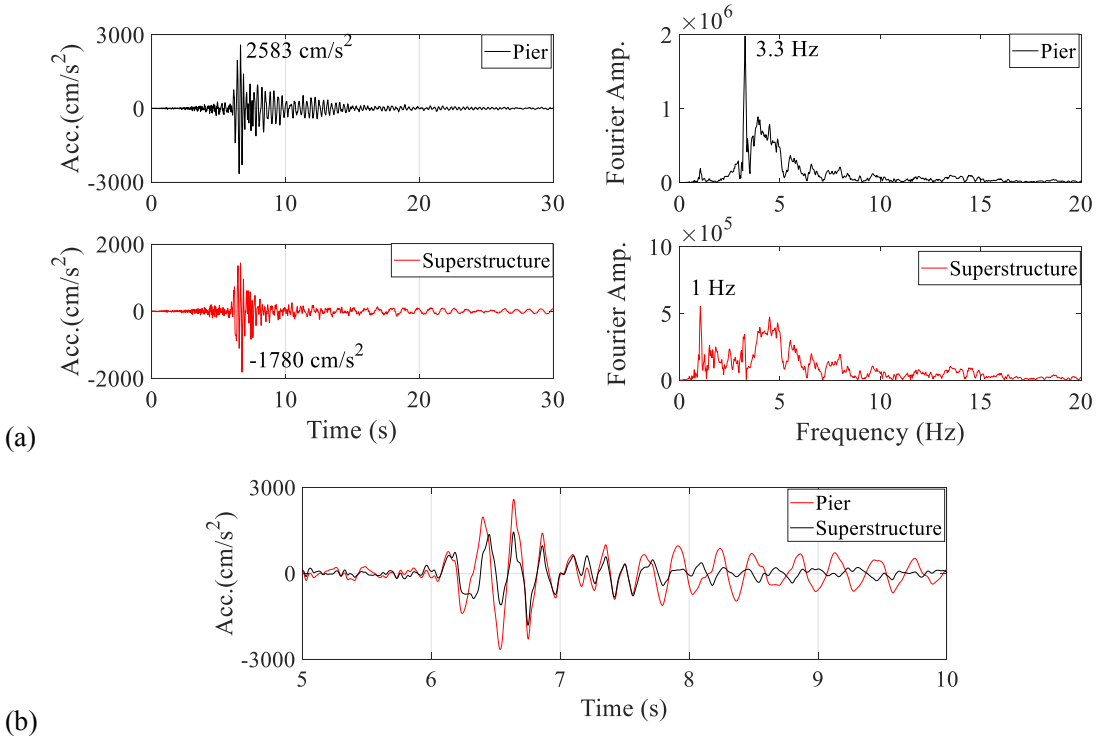

Fig. 3.15 Simulated response acceleration time-histories and Fourier transfer during Mid-Niigata earthquake; (a) 30s full-time duration of excitation, (b) enlarged time-history from 5 to 10s.

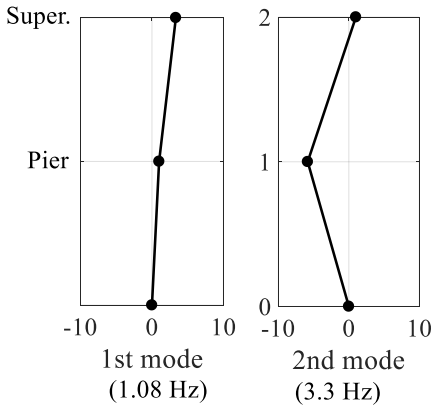

Fig. 3.16 Mode shapes of the isolated bridge pier at fundamental natural frequencies.

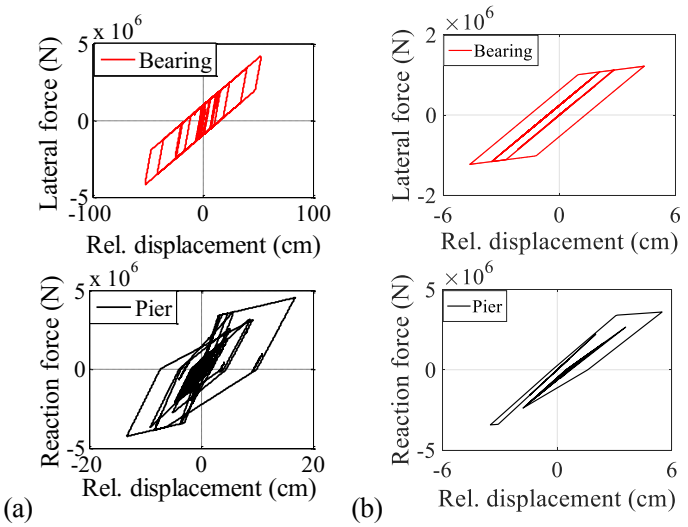

Fig. 3.17 Hysteresis loops of the bridge pier and bearings under (a) Kobe EQ and (b) Mid-Niigata EQ

3.3.5 Nonlinear seismic response analysis under various earthquake levels

Linearity and nonlinearity in the response of the structure depending on various seismic characteristics are demonstrated in this section. Structural dynamic behavior is examined for different seismic levels by taking various percentages of the original records, Kobe and Mid-Niigata earthquakes.

Kobe record at Takatori station

Different earthquake levels are categorized into three groups in terms of PGA; group I, small EQs, 0-30 gal (0.5-5% levels); group II, large EQs, 30-210 gal (10-35% levels); and group III, very large EQs, more than 210 gal (40% level). The levels and corresponding PGA are presented in Table 4. These groups are classified based on different dynamic response characteristics of the isolators and the bridge pier, as shown in Fig. 3.18. The responses of the pier and bearings are perfectly linear in small EQs; however, nonlinearity occurs in the response of the bearings from 10% level in large EQs and in both the ones of the bearings and pier in very large EQs.

Mid-Niigata record at Tahkamachi station

Different levels of Mid-Niigata earthquake, as shown in Table 4, are adopted to examine structural behaviors. For comparison, these scales of Mid-Niigata earthquake were chosen to have the same PGA values with the ones of Kobe earthquake. The transform of response characteristics of the structural elements from linearity to nonlinearity is depicted in Fig. 3.19. However, this transform is not significant since the impact of this earthquake with high frequency content on the structural behavior is little even with very large magnitudes (PGA).

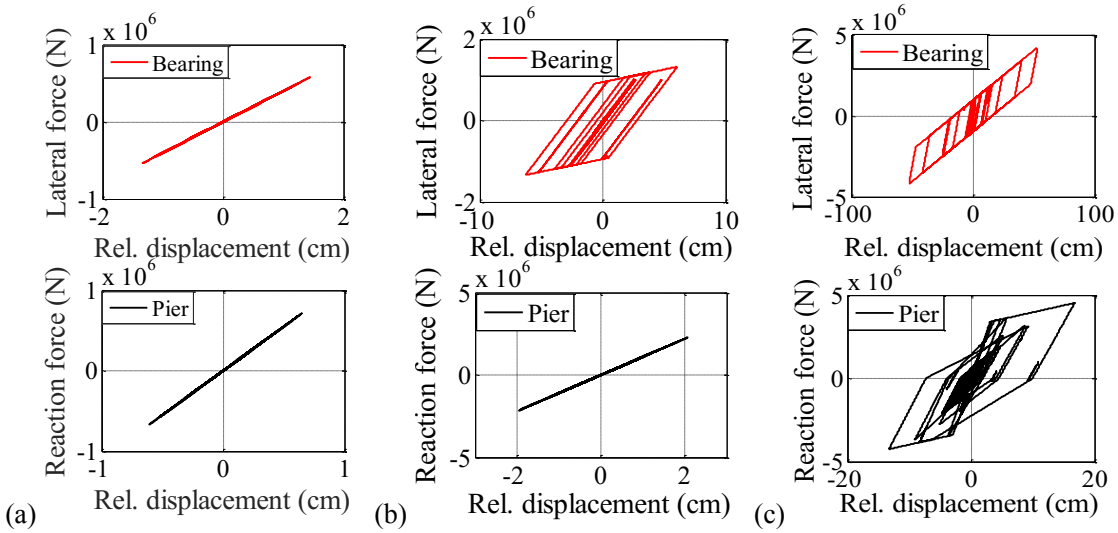

Fig. 3.18 Hysteresis loops of the bridge pier and bearings under three different Kobe earthquake levels of 5%, 25% and 100% levels corresponding to categorized in 3 groups: a) small earthquakes, b) large earthquakes, c) very large earthquakes, respectively.

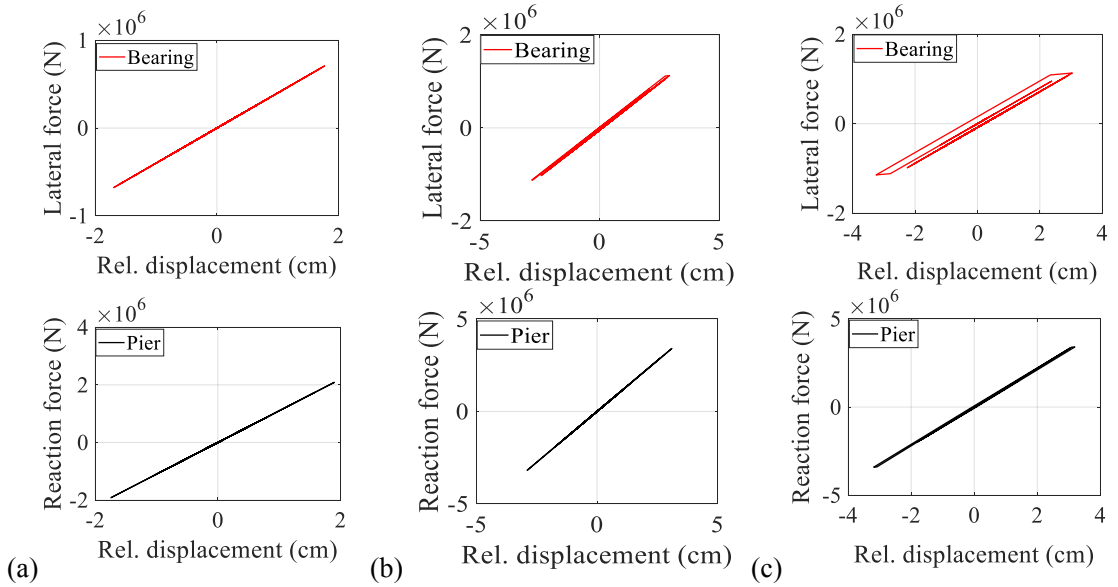

Fig. 3.19 Hysteresis loops of the bridge pier and bearings under three different Mid-Niigata earthquake levels of 29.3%, 49% and 56% levels corresponding to 600, 720, and 840 gal, respectively.

3.3.6 Monitoring data

Monitoring data is essentially required for the uncertainty quantification of model parameters. In this study, an artificial data set is created by adding zero-mean Gaussian noise to simulated time-history responses of the structure. A high signal-to-noise (SNR) of 80 dB, i.e., RMS amplitude of the signal being 10000 times that of noise, was assumed for acceleration responses.

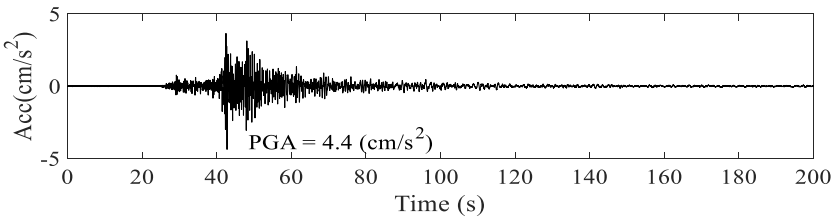

Fig. 3.20 Acceleration time-history of the earthquake measured on 21 Sep., 2011 at ground level from sensor 112.

Chapter 4

Bayesian sensitivity analysis to an existing base-isolated building

4.1 Applicability of Bayesian sensitivity analysis to linear and nonlinear dynamic responses

The applicability of the BSA on nonlinear dynamic responses under seismic excitations is verified by comparing with MCSA. Here, an experimental three-story shear building, which was worked on by one of the authors at the Los Alamos National Laboratory (Nishio et al., 2016), is used for the verification.

4.1.1 Small-scaled structure and data acquisition

The test-bed structure was the three-story shear building structure as shown in Fig. 4.1 (a). Its numerical model and measurement data were already worked on in the previous study (Nishio et al., 2016). Notice that the structure, the experimental data, and the numerical model here belong to Los Alamos National Laboratory. The structure was assembled using aluminium columns (0.177 × 0.025 × 0.006 m) and floors (0.305 × 0.305 × 0.025 m) via bolted joints. The structure could slide on the rails in the uniaxial direction. An additional centered column (0.150 × 0.025 × 0.025 m) suspended from the top floor and a bumper attached on the 2nd floor was to create a nonlinear response mechanism under random excitations. The gap between column and bumper could be adjusted to obtain different response levels, i.e., the nonlinearity could be obtained by reducing the gap from 10 mm to approximately 0.1 mm. Notice that the entire system is placed on a rigid foam. For data acquisition, a force transducer was attached at the end of the stinger to measure input forces transferring from the shaker to the structure, and four accelerometers placed on the four floors including the base to measure accelerations for each. The shaker creates only lateral vibrations along the centreline of the structure. Analog signals were discretized at 4096 points with the sampling frequency of 640Hz.

Two random excitation levels, 1.5V RMS and 2.5V RMS, were generated for the linear and nonlinear cases, respectively.

4.1.2 Numerical model verification

A numerical analysis was crucially required for the variance-based sensitivity analysis. The structure was modelled as a 4-DOF lumped-mass system with nominal input parameters, for mass, M_i (i = 1, …,4); stiffness, K_i (i = 1, …,4); and damping ratios, C_i (i = 1, …,4). The equation of motion was described as follows:

$$\mathbf{M}\ddot{\mathbf{x}} + \mathbf{C}\dot{\mathbf{x}} + \mathbf{K}\mathbf{x} = \mathbf{F}(t) \tag{3.21}$$

where **M**, **K**, and **C** are the mass, stiffness, and damping matrices, respectively; **x** is a displacement vector, and **F**(t) is input force vector. The mass M_i in **M** is determined from actual measurement of structural elements of each story. The stiffness K_i (i = 2,3,4) in **K** is the sum of bending stiffness of four columns; however, K_1 was assigned with a relatively small value of 0.1 N/cm because of neglectable friction between the base and the rails. The damping **C** was constructed in uncoupled motion equations with modal values of mass, frequency, and damping ratios estimated from experimental data. The Runge-Kutta numerical integration incorporating Rayleigh damping was applied to solve Eq. (12) with 0.001s time increment. Figure 4.2 shows the four resonant modes of the 4-DOF structure. The first mode is the rigid body mode due to low stiffness for modeling rail performance, and the three later modes were the modes of the superstructure with identified frequencies of 28.8 Hz, 55.2 Hz, and 71.5 Hz, respectively.

A comparison between calculated and experimental results was performed for the model validation. The model accuracy to some extent is qualitatively evaluated via the overlay in Fig. 4.3 since very high-dimensional features of time history results are hard to quantify adequately in the same dimension. Figure 4.3 shows relatively good agreement between simulated and measured results in both time domain and frequency domain.

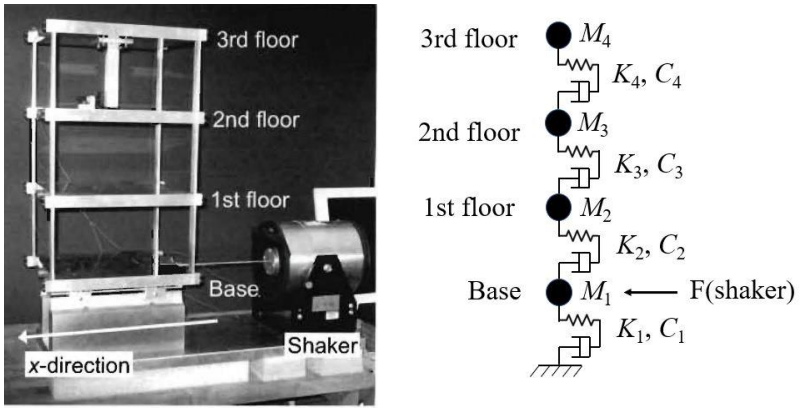

(a) Three-story building (b) 4-DOF model

Fig. 4.1 Test-bed structure and 4-DOF model (Nishio et al., 2016)

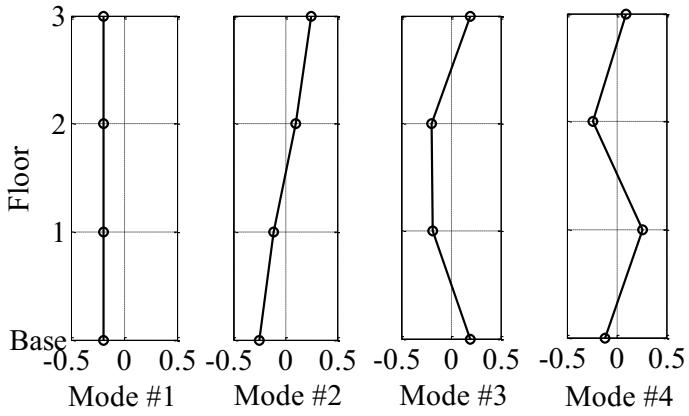

Fig. 4.2 Mode shapes of the three-story building

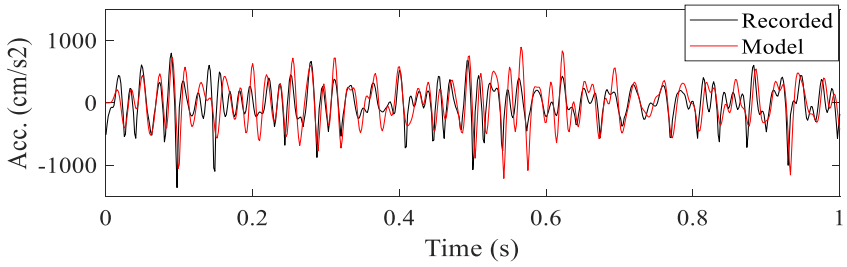

(a)

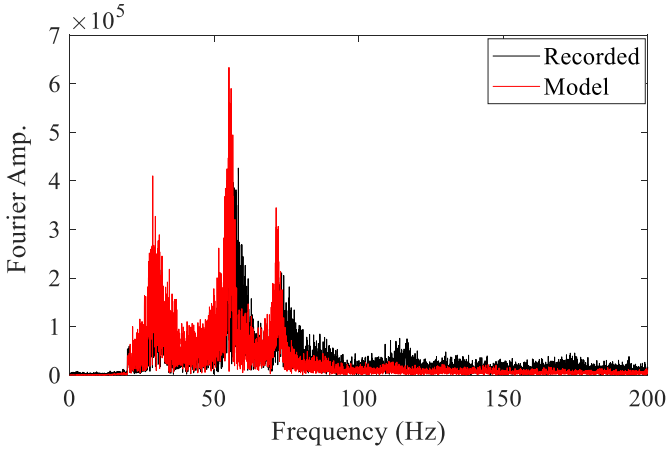

(b)

Fig. 4.3 Overlays of simulated and recorded accelerations of the 3rd floor in terms of the nonlinear case in (a) time domain, (b) frequency domain.

4.1.3 Sobol' index comparison between BSA and MCSA

In this context, we present estimated Sobol' index results for two linear and nonlinear response cases on the experimental model. Eight uncertain variables include mass, M_1, M_2, M_3, M_4, and stiffness, K_1, K_2, K_3, K_4 of floors from the base to the top, as defined in Fig. 4.1(b), were concerned. Herein, the root mean squared error (RMSE) of prediction errors between measured and simulated output accelerations was chosen as an appropriate feature for performing GSA incorporating experimental observations. A uniform variability of ±10% was equally proposed for each variable. We applied the Latin hypercube sampling and quasi-random sequences for BSA and MCSA, respectively. A learning sample of size 200 was generated to construct the metamodels in BSA. For designing experimental samples in MCSA, convergence analysis is firstly performed to identify a proper sample size. Convergence analysis was basically done following Central Limit Theorem. The sample size was increased gradually by independent replicas of a base sample of 1000, SIs then were calculated for each increased sample. The procedure was kept until SIs approximately unchanged. The convergence rate of the total SIs in Eq. (2.10) is inherently higher than the one of main SIs in Eq. (2.9) since all variables except for a variable of interest in Eq. (2.10) were set constant meanwhile, this is converse in Eq. (2.9). Figure 4.4 shows the convergence plots of main SIs computed by MCSA for both linear and nonlinear cases. Figure points out that convergence is obtained at about 12,000 runs for factor ranking (FR) and 18000 runs for sensitivity indices (SIs) in the linear case. Whereas a slower convergence rate is found at approximately 19,000 runs and 23,000 runs for FR and SIs, respectively. The convergence of FR is reached if the ordering of variables remains stable meanwhile the convergence of SIs is achieved if the SIs values

are kept unchanged. In fact, models are more complex; more runs are required to obtain a convergence point.

Considering sensitivity of the parameters, Fig. 4.4 also indicates that stiffness of lower floors K_2 and K_3 has higher SIs than others, especially K_2 in both cases. It is recognized that stiffness changes of the lower floors significantly affect the response of the structure, i.e., vibration frequency, and magnitudes. Another interesting point is that mass M_1, and M_4 in the nonlinear case have higher sensitivity than M_2 and M_3, particularly M_1 with the highest index. It can be explained that with a predetermined input force, M_1 plays an important role to transfer force from the stinger to the structure through the base, the variability of M_1 critically changes input acceleration at the base. Along with the nonlinear response of the structure, the variability of M_1 predominantly affects the acceleration of the top floor than the linear case. Practically, without the support of SA tools, it is hard to quantify the variability of different structural parameters which influence output responses at specific locations under various excitations.

The accuracy of SIs results produced by the two approaches was evaluated through the standard errors. One sample result of the sensor located at the third floor in the nonlinear model, as shown in Table 6, indicates that 95% confidence interval of the standard errors of the main indices as defined in Eq. (11) is smaller than the ones of total indices. Both methods have very small standard errors which can be neglected. The comparison of the coefficient of variance (COV) of input variables produced by BSA indicates that COVs of K_1 and K_4 are high especially in the nonlinear case while the others have small COVs of less than 10%, see Table 7. Nevertheless, these variables are non-influential input factors with very low indices, as referred from Table 6, and thus their variance has a negligible effect on the output's variance. Additionally, there is not much difference regarding COVs of SIs between linear and nonlinear response cases except for the ones with very low indices. Therefore, either linear or nonlinear models can still be adopted using the BSA method.

Regarding main and total SIs, Fig. 4.5 and Fig. 4.6 illustrates that the SIs computed by BSA and MCSA against RMSE of simulated and measured accelerations of the third floor are quite close each other in both time and frequency domain. Sensitivity analysis in the frequency domain (Fig. 4.6) indicates the variability of parameter importance in three dominant frequency ranges, 20-40 Hz, 50-60 Hz, 70-80 Hz corresponding to mode #2, mode #3, and mode #4, respectively. For instance, Fig. 4.5 depicts that K_2 is most influential to the prediction errors in the time domain. However, its ranking is varying in the different frequency ranges with the highest SIs at mode #2, see Fig. 4.6. On the other hand, the high discrepancy between main and total SIs indicates that interaction between the parameters significantly increase their impact on the output variance, and therefore it needs to be critically considered in GSA.

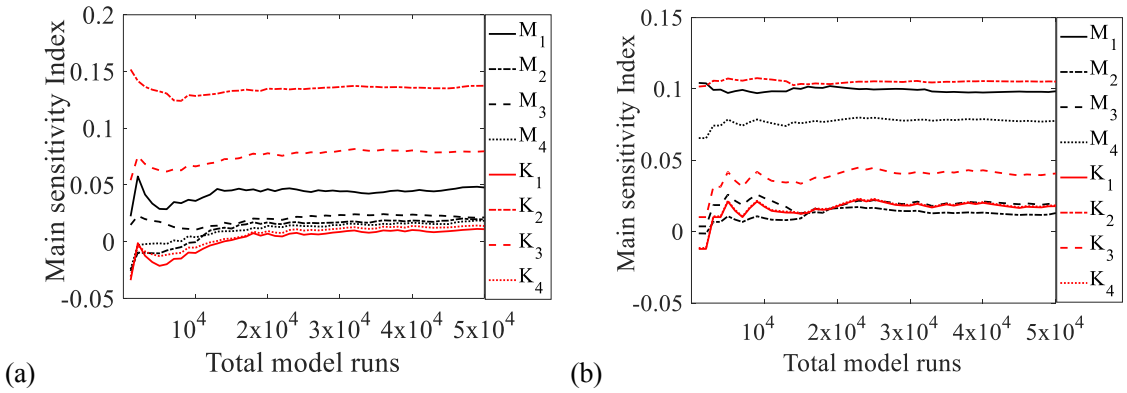

Fig. 4.4 Convergence plots of eight variables against RMSE of the prediction errors between observed and simulated output accelerations for (a) linear model, and (b) nonlinear model.

Table 6. SIs and standard errors of BSA and MCSA against RMSE of the prediction errors between recorded and simulated output accelerations of the 3rd floor for the nonlinear model.

Var.	BSA				MCSA			
	Main SI		Total SI		Main SI		Total SI	
	$\mu_{\overline{S}_i}^T$	95% CI	$\mu_{\overline{S}_i}^T$	95% CI	$S_i^{(MC)}$	95% CI	$S_i^{T(MC)}$	95% CI
M_1	0.089	1.33E-04	0.382	3.25E-	0.098	9.48E-04	0.386	4.28E-
M_2	0.013	6.04E-05	0.263	2.40E-	0.013	1.21E-04	0.252	3.21E-
M_3	0.006	3.55E-05	0.271	3.76E-	0.020	1.83E-04	0.271	3.22E-
M_4	0.063	1.19E-04	0.239	2.97E-	0.078	7.12E-04	0.259	3.02E-
K_1	1.45E-	5.77E-06	8.05E-	8.32E-	1.23E-	1.58E-05	5.29E-	6.85E-
K_2	0.083	6.62E-05	0.564	3.64E-	0.105	9.91E-04	0.572	6.32E-
K_3	0.025	7.05E-05	0.131	3.70E-	0.041	3.66E-04	0.116	1.48E-
K_4	5.73E-	3.18E-06	3.27E-	9.25E-	2.03E-	1.63E-05	3.92E-	5.07E-

Table 7. The coefficient of variance (COV) of the SIs produced by BSA against RMSE of the prediction errors between recorded and simulated output accelerations of the 3rd floor for linear and nonlinear models

Var.	Linear model		Nonlinear model	
	COV (Main SI)	COV (Total SI)	COV (Main SI)	COV (Total SI)
M_1	5.06%	2.90%	2.42%	1.38%
M_2	9.04%	1.05%	7.75%	1.47%
M_3	5.94%	1.64%	9.12%	2.24%
M_4	2.59%	1.64%	3.04%	2.00%
K_1	46.00%	114.91%	64.39%	166.68%
K_2	1.77%	0.67%	1.28%	1.04%
K_3	3.99%	4.27%	4.60%	4.56%
K_4	34.01%	17.85%	89.48%	456.61%

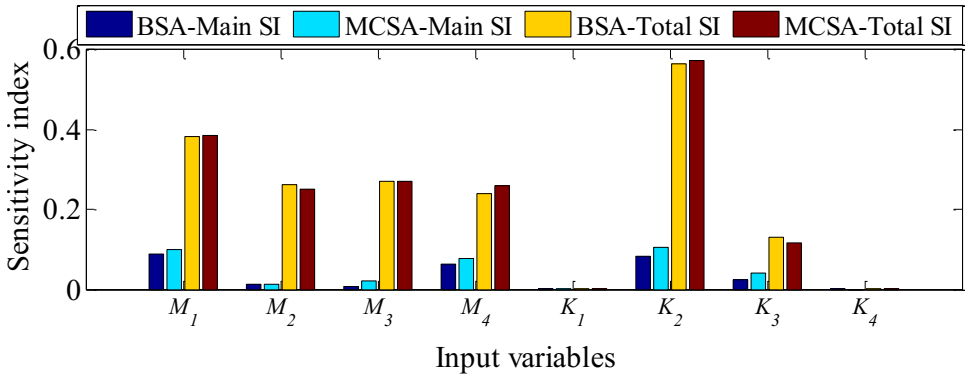

Fig. 4.5 Sensitivity indices of BSA and MCSA against RMSE of the prediction errors between observed and simulated output accelerations in time domain at the 3rd floor in the nonlinear model.

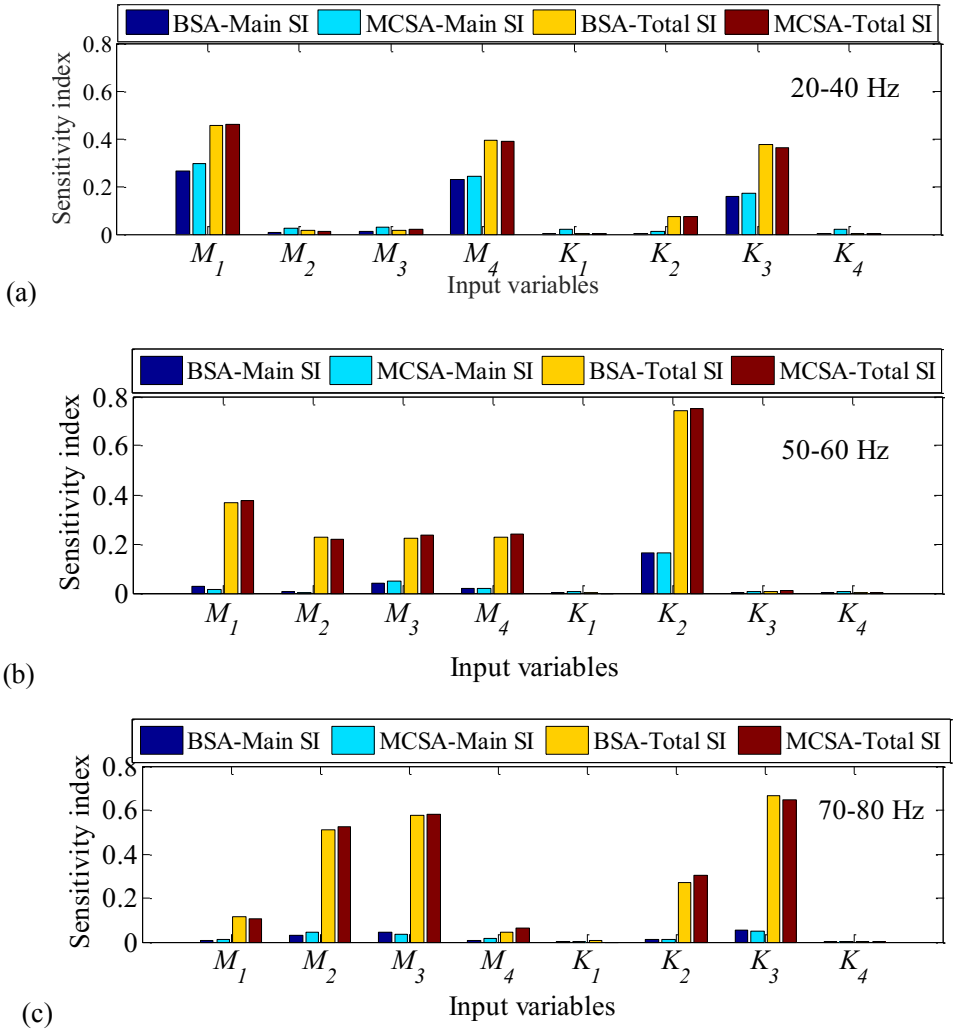

Fig. 4.6 Sensitivity indices of BSA and MCSA against RMSE of the prediction errors of Fourier amplitudes transferred from the response accelerations of the 3rd floor in three dominant frequency ranges a) 20-40 Hz, b) 50-60 Hz, c) 70-80 Hz corresponding to three first torsional modes of the nonlinear model.

4.2 Bayesian sensitivity analysis to the existing building

Comparison between numerical results and recorded data indicated small error levels in large earthquakes but large errors in small earthquakes. The study also indicates that there is the possibility of the structural stiffness reduction after the main shock. Although the numerical results of the main shock showed an acceptable error level, accumulated structural changes attributed to large earthquakes or consecutively small earthquakes possibly lead to critical errors in future large earthquakes. Moreover, seismic risk prediction should be implemented on a properly updated model. The numerical model hence requires being updated with time. In this section, BSA using the metamodels was performed to calculate SIs for each output. It is noted that

4.2.1 Global input variables

In this study, two uncertainty sources are considered: the systematic uncertainty due to lack of knowledge on material properties in modeling process and the uncertainty of structural properties resulting from external effects on the structure under large earthquakes. The former always exists, simply because the predicted results have never been matched with measurements. Therefore, all input parameters of numerical models can be considered as uncertain parameters. In this section, the authors first conducted GSA for all input variables of the model such as mass M_s, stiffness K_s and damping ratio ξ_s of the superstructure, stiffness K_b and damping ratio of the base ξ_b. These variables are termed global input variables. It is also noticed that damping ratio, an assigned parameter in the initial design phase can be independent of others. However, in a theoretical sense, they should be treated as correlated variables, and hence Sobol' decomposition in Eq. (1.1) cannot be interpreted accurately. In cases with either uncorrelated or correlated variables, main SIs can still be a good interpretation of how a variable's variance influences on the variance of output without interaction effect between variables.

BSA on global inputs was carried out for two earthquakes with different intensities, one is the foreshock on March 9, 2011, with PGA of 5 gal in the *X* direction and 6 gal in the *Y* direction and the other is the main shock with 160 gal and 170 gal in the *X* direction and *Y* direction, respectively. The structural response under large earthquakes is supposed to be nonlinear. To create experimental input samples for BSA, we first assumed bounds of the uncertain parameters. In this study, an assumption of ±10% uniform variability for M_s, K_s, K_b, and uniform distributed ranges of 0.01-0.03 and 0.025-0.075 for ξ_s and ξ_b, respectively, were applied.

Bayesian sensitivity analysis was implemented by MCMC with random walks in single chain. Therefore, convergence analysis is required to obtain stable sensitivity indices for each run case. A rule of thumb for iteration number of $M = 50000$ including $m = 5000$ burn-in were called through MCMC. The burn-in iterations were finally discarded. The final posteriors were derived by a thinning interval of $n = 5$. The total iteration number equal to $N = M + m \times n$, i.e., N being 75000. Figure 4.7 indicates that draws of the parameters is close to pseudo randomness. This implies the convergence of the chain. In other words, the mean value of the draws or the point estimate of the posterior distributions approach stationary. The last 50000 iterations are used to derive the posterior distributions. Figure 4.8 indicates the convergence of the chain after 300 draws in 5000 burn-in. By this way, the number of iterations can be reduced to save computational cost. However, MCMC was implemented on a single chain which was too early to say that the posterior has reached a converged distribution. Therefore, the author keeps running a long chain to obtain good estimate. Convergence diagnostics by trace plots and running mean were performed for all sensitivity cases under each earthquake.

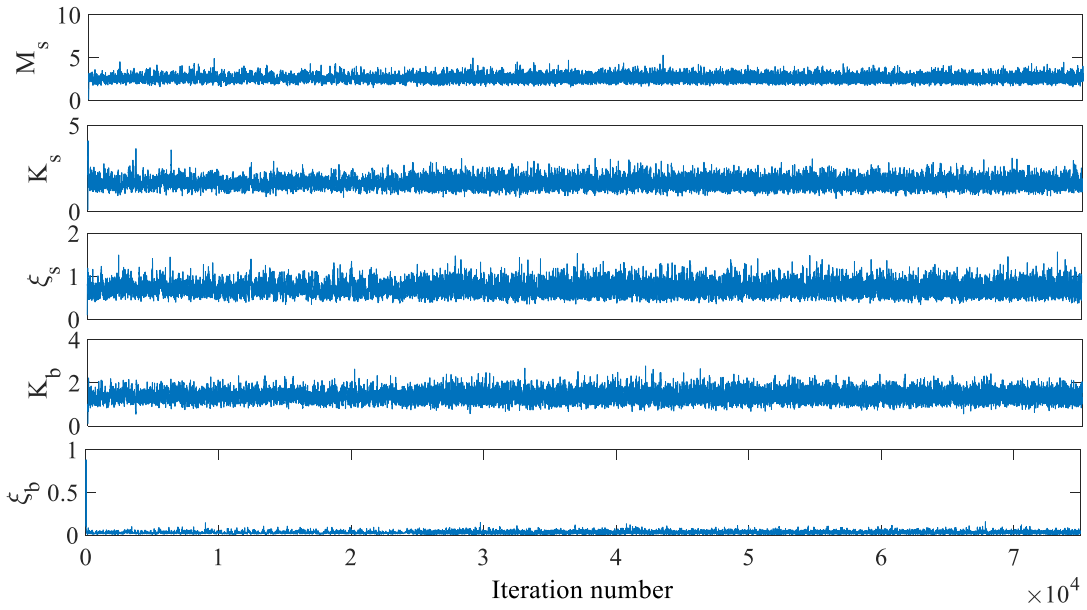

Fig. 4.7 Trace plot of MCMC iterations of the model parameters M_s, K_s, ξ_s of the superstructure and K_b, ξ_b of the base for the response measured at sensor C111 under the foreshock on March 9, 2011.

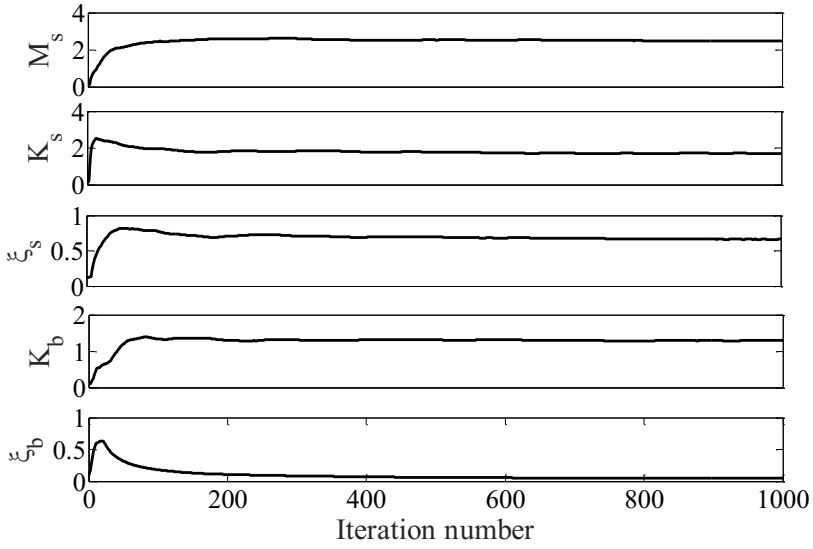

Fig. 4.8 Running mean of the model parameters M_s, K_s, ξ_s of the superstructure and K_b, ξ_b of the base for the response measured at sensor C111 under the foreshock on March 9, 2011.

Figure 4.9 shows that the input parameters of the superstructure M_s, K_s and ξ_s significantly influenced RMSE between simulated and recorded accelerations in comparison with K_b and ξ_b in the foreshock. Comparing this with the ones of the main shock in Fig. 4.10, the sensitivity of the parameters in the main shock has an inverse trend,

i.e., SIs of M_s and K_s of the superstructure are lower while K_b and ξ_b of the base are higher than the ones in Fig. 4.9. This can be explained to be because the base isolation function was well engaged in the structure's response to the main shock while the upper structure's behavior was dominant in the foreshock. Subsequently, any structural changes in the superstructure can also cause high errors in small earthquakes, which can be concerned in model updating. Another remarkable characteristic is that the variability of the superstructure parameters M_s, K_s significantly affects to RMSE at building C in the X direction and building B in the Y direction, as shown in Fig. 4.9 and Fig. 4.10. The damping ratio ξ_s notably influences to building B and one side of building C (at the locations of sensors C103, C106, C108, C110) in the foreshock, see Fig. 4.9; however, it is more dominant to the other side of building C in the main shock (at the locations of sensors C104, C107, C109, C111), as shown in Fig. 4.10. It can be hence said that with a high-density sensor deployment, SA with above global variability assumption of inputs can partially specify the influence of inputs on outputs at various locations of the building. A more comprehensive analysis with local variability assumption is performed to analyze input-output relation in more detail and predict structural changes or modeling errors in the next section.

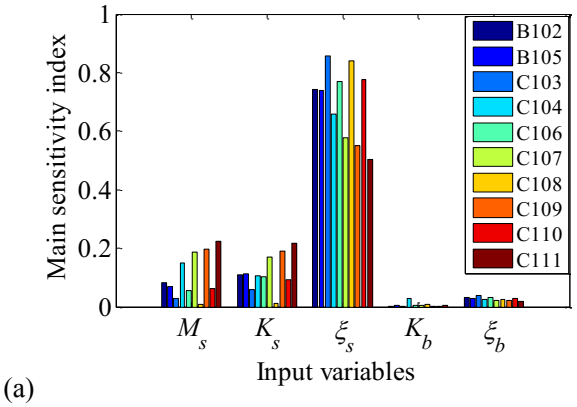

(a)

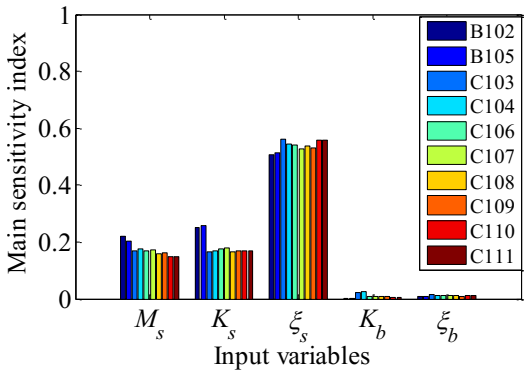

(b)

Fig. 4.9 Main sensitivity indices of uncertain parameters against RMSE between recorded and simulated output accelerations in the time domain in (a) X-direction and (b) Y-direction under the small foreshock on March 9, 2011.

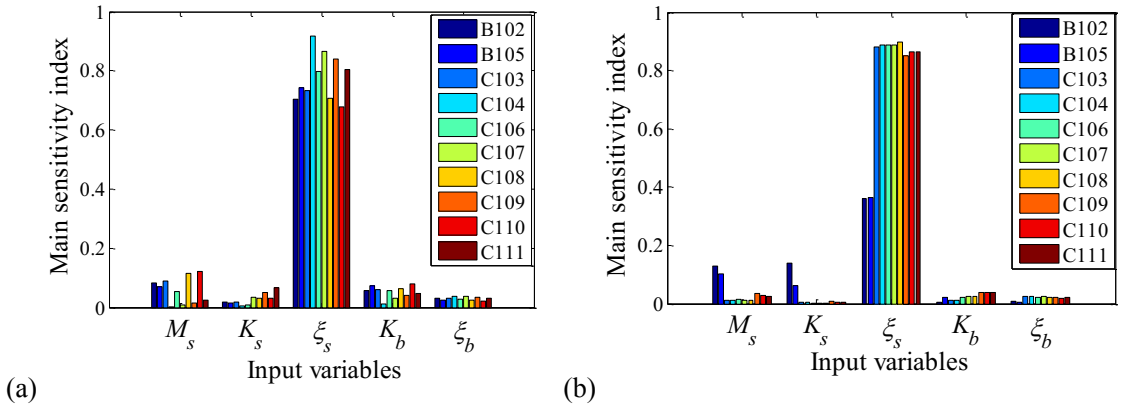

Fig. 4.10 Main sensitivity indices of uncertain parameters against RMSE between recorded and simulated output accelerations in the time domain in (a) X-direction and (b) Y-direction under the main shock on March 11, 2011.

4.2.2 Local input variables

As aforementioned, there was the possibility of the structural changes after the mainshock, i.e., the stiffness reduction of the superstructure after the largest earthquake and the stiffness variance of the isolation system due to Mullin's effect. The change of the isolation system's stiffness was temporal and recoverable; therefore, the authors concentrated on SA of the stiffness parameters of the upper structure. Stiffness parameters herein are termed local input variables.

By functioning BSA on the structural stiffness parameters, the aim of predicting which parameter was the most influential, which ones are uninfluential to the errors can be obtained. Here, the aftershock on September 21, 2011, with small PGA of 5.26 gal in the *X* direction and 4.4 gal in the *Y* direction was chosen for BSA with the fact that a high error level was found on this small earthquake. The building was divided into eight groups, B1, B2, Cb1, Cb2, Ca1, Ca2, C1, and C2, as shown in Fig. 10 (a), corresponding to 8 local stiffness parameters K_{B1}, K_{B2}, K_{Cb1}, K_{Cb2}, K_{Ca1}, K_{Ca2}, K_{C1}, K_{C2}. A learning sample of the parameters from Latin hypercube sampling with ±10% uniform variability for each was adopted for BSA.

To estimate the influence of one parameter to the structural responses at distinct positions of the building, the simultaneous variability of all inputs should be involved in sensitivity measures; and therefore, the total SIs were used to obtain this. By the factor ranking using the total SIs, the relation between model inputs and outputs can be interpreted explicitly. Figure 4.11 shows total SIs in terms of RMS of simulated output accelerations in the time domain. The variability of K_{Ca1} impacts significantly on the response of low floors at the corner of building C and decreases its influence on higher floors in the X direction. While K_{Ca1} is most influential to response at its location, K_{B1}

and K_{B2} indicate large impact on B2 and B1 in Y direction, respectively. The variability of K_{C1} has a high impact on the top of building B. Obviously, this topology is hard to learn about complex structures in general without the support of SA tools.

In the time domain, RMSE of the prediction errors between simulated and recorded accelerations was chosen to roughly predict significant parameter uncertainties under unknown local stiffness changes. The main SIs estimated in the time domain, as shown in Fig. 4.12, illustrates that the uncertainty of local stiffness parameters affects the errors in diversified degrees, some of which emerges as critically sensitive parameters while others seem to be uninfluential. When relatively comparing SIs in terms of each output at a sensor location, the stiffness of lower parts, K_{B1}, K_{Ca1}, K_{C1} have higher sensitivity to the errors than the ones of upper parts; K_{B2}, K_{Ca2}, K_{C2}. It is consistent with findings in section 4.4.1 that high transfer ratios are found at the low parts of the building. It is predicted that the lower parts have a higher possibility of stiffness reduction than others do.

In the frequency domain, RMS of Fourier amplitudes transferred from simulated output accelerations in three frequency ranges 0.3-0.5 Hz, 0.6-0.9 Hz and 0.9-1.2 Hz corresponding to mode #1, mode #2, and mode #3, respectively was chosen as an appropriate feature for BSA of the local parameters. It is interesting that sensitivity of the local stiffness in the frequency domain, as shown in Fig. 4.13, are strongly related to mode shapes as presented in section 4.2. Considering the first mode (mode #1) that has large displacement at the base, the parameter uncertainty more influences on the response variance of model parts in which they were defined. For instance, K_{B1} significantly affects the response of building B while K_{Ca1} is more influential to building Ca. Regarding mode #2, highly sensitive parameters are found at building C in the *X* direction and building B in *Y* direction where have large modal displacements, e.g., the variance of K_{B1} significantly influences to the corner Ca of building C in the *X* direction and building B in the *Y* direction. Regarding mode #3, since the response of the structure was oriented following to *Y* direction, higher sensitivity was found at positions of the building in this direction, e.g., K_{B1} is the most sensitive parameter in the *Y* direction. To sum up, there is a strong relationship between mode shapes and the superstructure parameters' sensitivity indices when considering the response at different positions on the building and hence contribute to comprehensive understanding about the structure's modal responses and input-output relations.

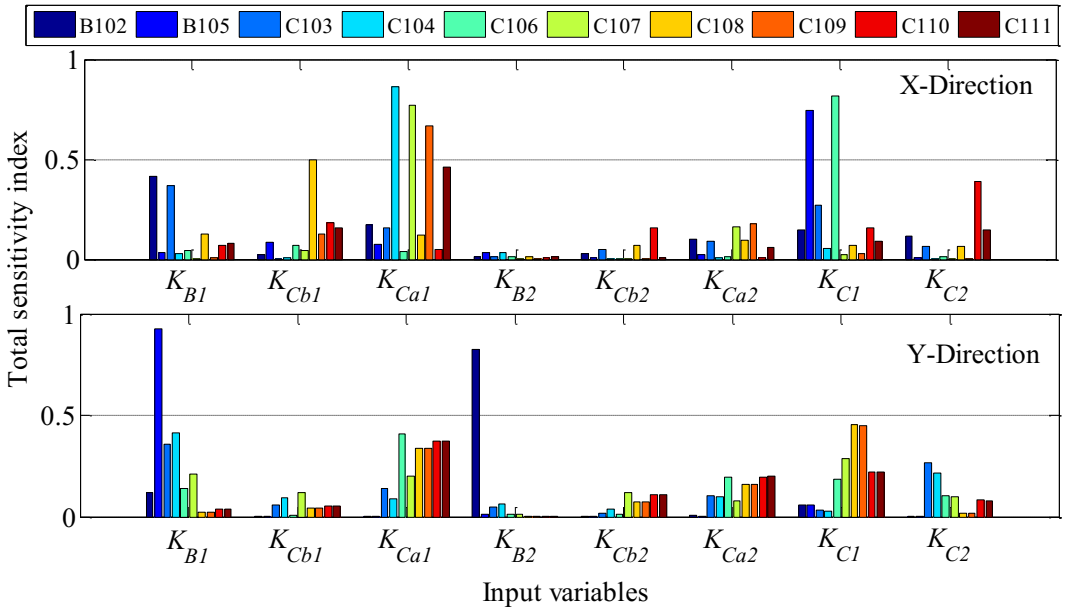

Fig. 4.11 Total sensitivity indices of local stiffnesses against RMS of simulated output accelerations in time domain under the aftershock on September 21, 2011.

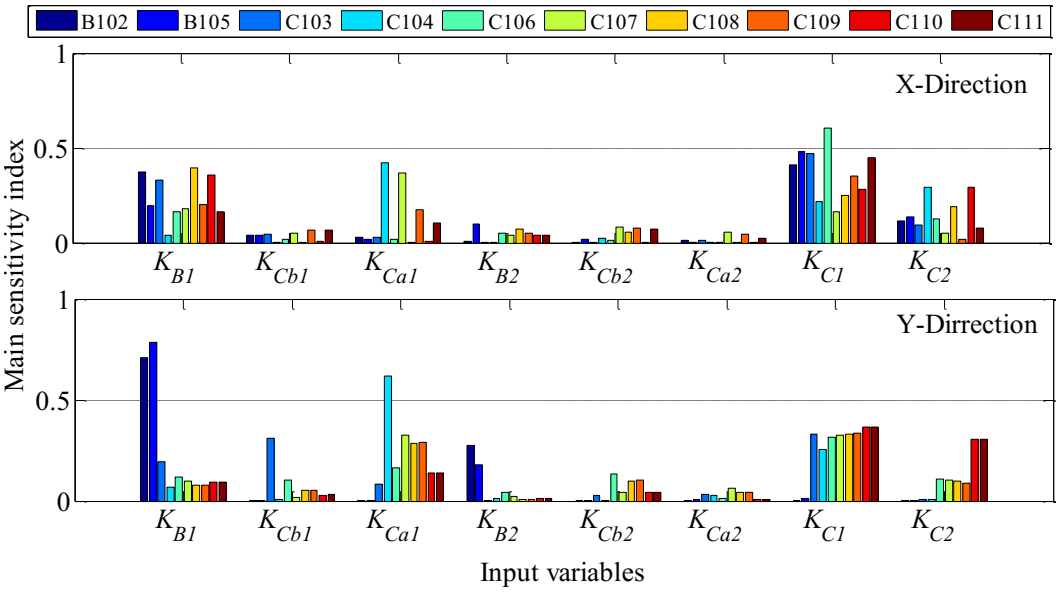

Fig. 4.12 Main sensitivity indices of local stiffnesses against RMSE of the prediction errors between recorded and simulated output accelerations in time domain under the aftershock on September 21, 2011.

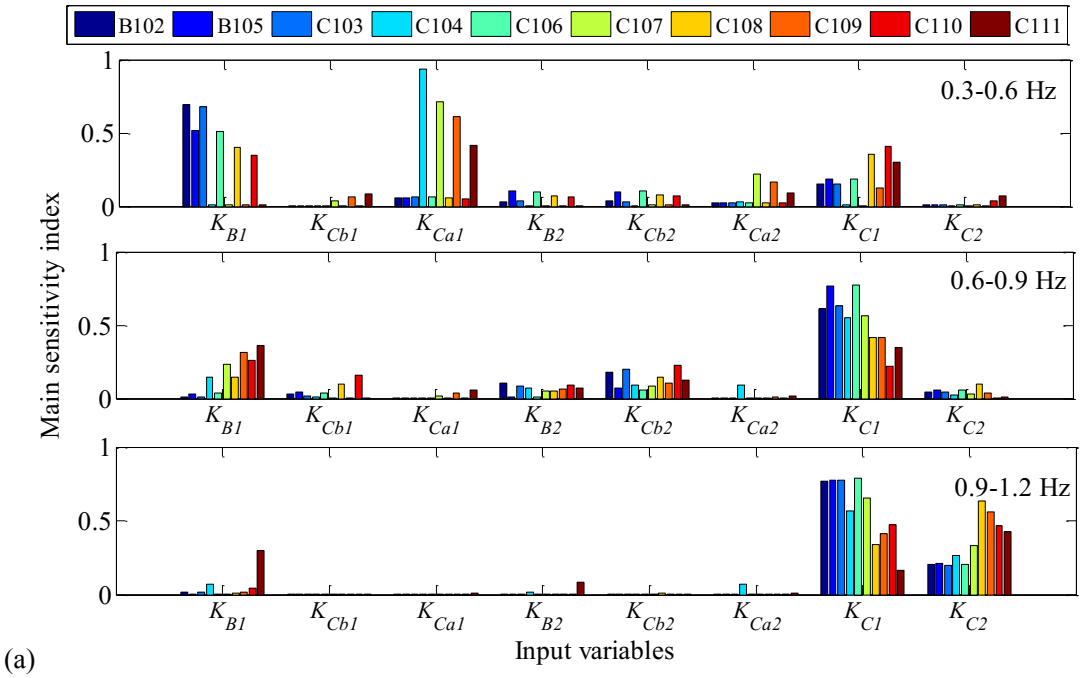

(a)

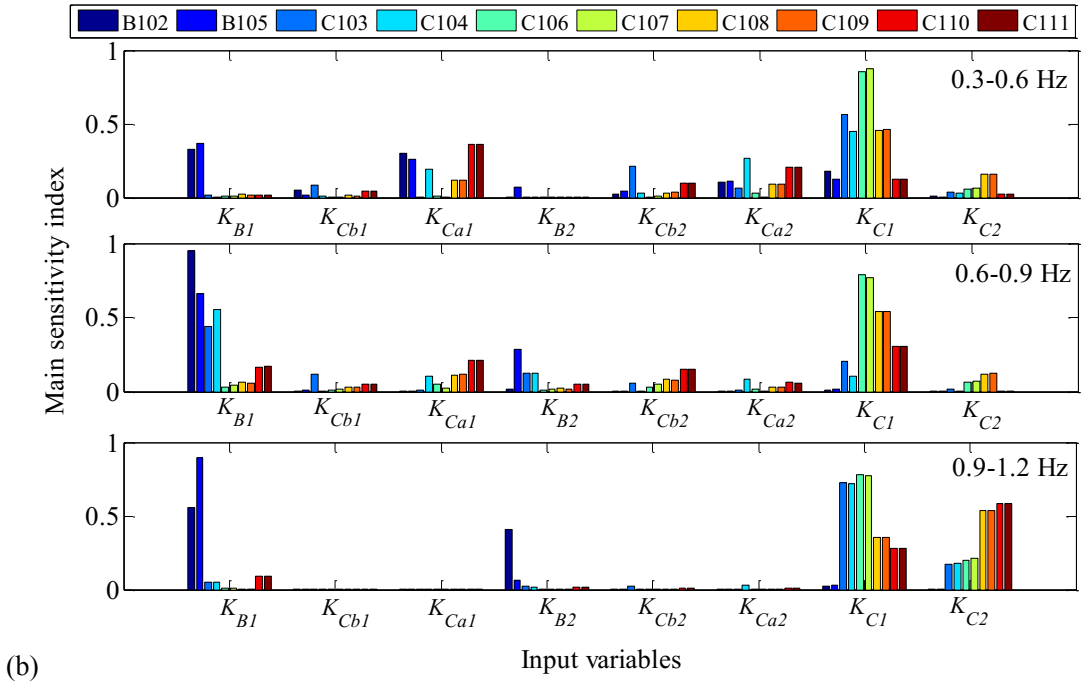

(b)

Fig. 4.13 Main sensitivity indices of local stiffnesses against RMS of Fourier amplitudes transferred from simulated output accelerations in the frequency domain in (a) X-Direction, (b) Y-Direction under the aftershock on September 21, 2011.

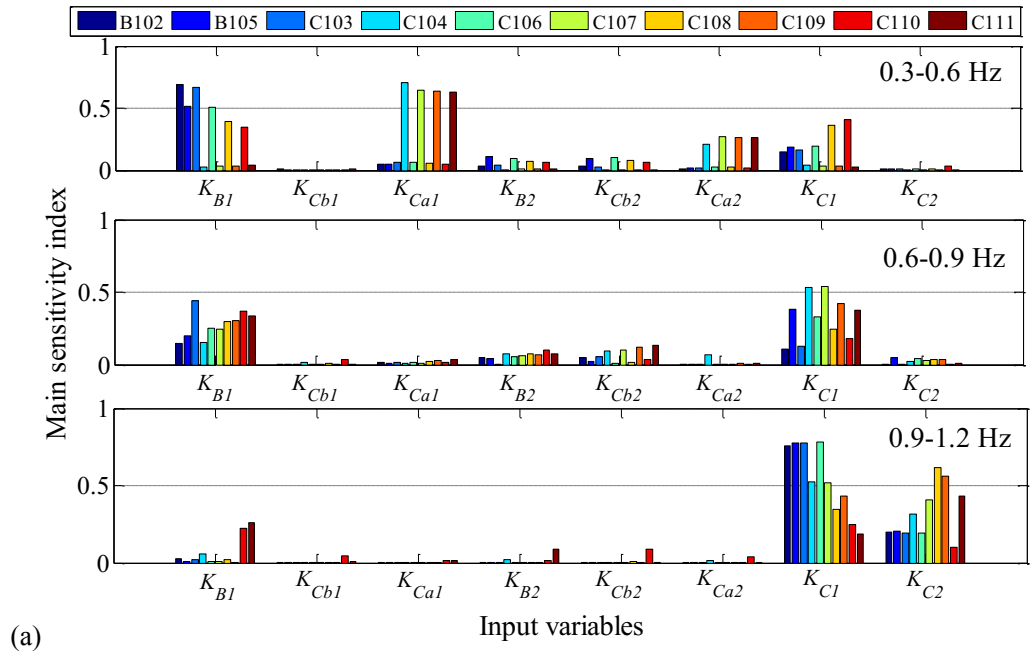

(a)

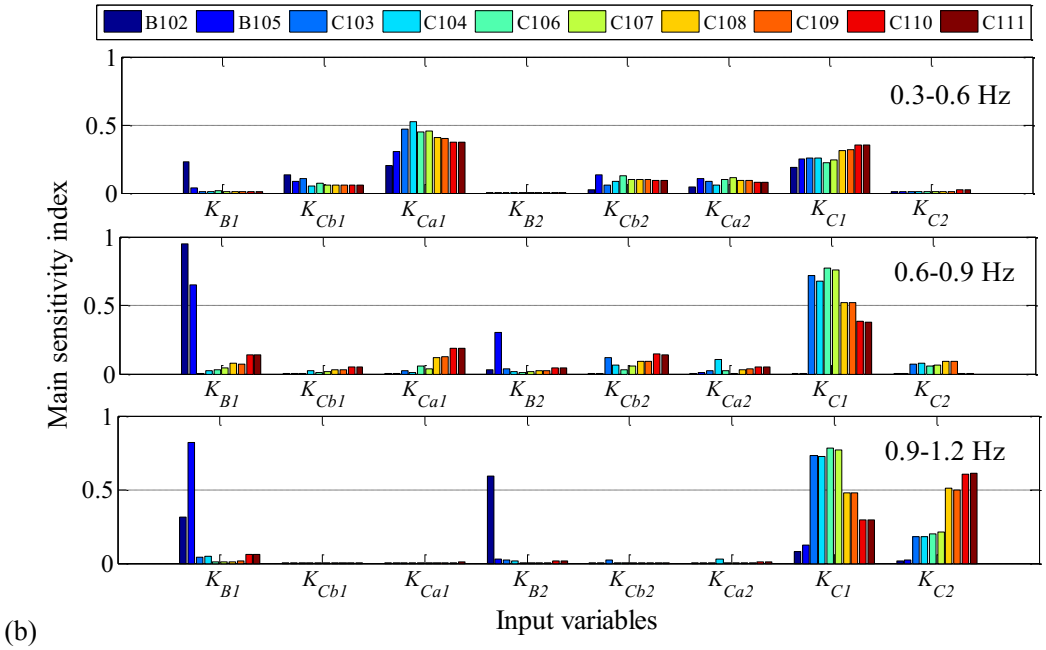

(b)

Fig. 4.14 Main sensitivity indices of local stiffnesses against RMSE of Fourier amplitudes transferred from simulated output accelerations in the frequency domain in (a) *X*-Direction, (b) *Y*-Direction under the aftershock on September 21, 2011.

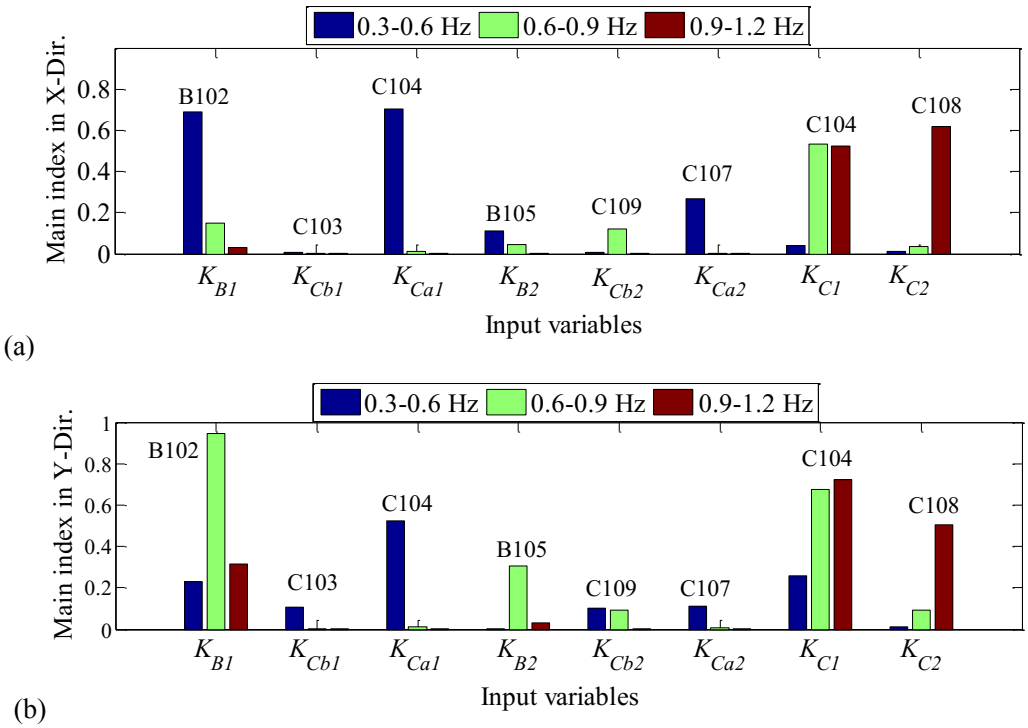

Fig. 4.15 Main sensitivity indices of local stiffness against RMSE of Fourier amplitudes transferred from simulated output accelerations in three frequency ranges, 0.3-0.5 Hz, 0.6-0.9 Hz and 0.9-1.2 Hz corresponding to mode #1, mode #2, and mode #3 of the structure, respectively in (a) X-direction, b) Y-direction under the aftershock on September 21, 2011.

Errors between simulated outputs and measurement can be localized by indicating SIs difference between two cases related to output features, RMS and RMSE, as shown in Fig. 4.13 and Fig. 4.14, respectively. The errors can be either from structural damages or modeling errors or both. SIs results against RMS of simulated outputs represent response characteristics of the numerical model itself. In case of no errors, SIs in two cases are expected to be consistent. Any significant difference between them can specifically predict which uncertain parameters should be updated. The difference of SIs related to output features RMS and RMSE in Fig. 4.13 and Fig. 4.14 respectively is prominent at some specific parameters. K_{B1}, K_{C1} in the range of 0.6-0.9 Hz in both X and Y direction, and K_{B1}, K_{Ca1}, K_{C1} in 0.3-0.5 Hz in Y direction. As analyzed earlier, these parameters belonging to the lower parts of the building are notably sensitive to the outputs. To what follows, these remarkable parameters should be regarded in model updating due to their stiffness reduction possibility and error presence in the modeling process.

On the other hand, the different influence level of parameters to various positions on the building is beneficial to select appropriate sensors for model updating using monitoring data. One sensor is selected for each parameter based on its high sensitivity index performance against RMSE of the prediction errors in the time domain at that

sensor location, see Fig. 4.12. For example, considering the sensitive degree of K_{Ca1} at different sensor locations shows that sensor C104 with the highest SI can be chosen for updating K_{Ca1} in both directions. A similar work can be done in three dominant frequency ranges of 0.3-0.5 Hz, 0.6-0.9 Hz and 0.9-1.2 Hz corresponding to mode #1, mode #2, and mode #3 for more detail concerns, as shown in Fig. 4.15. In this figure, SIs of the parameters from the selected sensors were referred from Fig. 4.14. Different sensitivity degrees of the parameters in dissimilar frequency ranges can narrow data to required bandwidths from the large observed data volume. For instance, needed data of sensor C104 for updating K_{Ca1} in both X and Y directions can be limited in the frequency range of 0.3-0.5 Hz since K_{Ca1} in other frequency ranges have very small sensitivity indices which can be neglected.

Chapter 5

Monte Carlo sensitivity analysis

Monte Carlo sensitivity analysis (MCSA) can be applied in a broad field of engineering including linear or nonlinear structural dynamics. Unlike Bayesian sensitivity analysis (BSA), which was presented in the previous chapter, using Markov Chain Monte Carlo iterations to estimate sensitivity indices (SIs) in the Bayesian scheme by statistical moments, MCSA uses pseudo-random or quasi-random Monte Carlo to generate random samples for sensitivity calculations of uncertain parameters. Both methods can be computed based on the Analysis-of-Variance algorithm in global space. In this chapter, MCSA for the seismically isolated bridge pier in Japan Design Specifications of Highway Bridges will be introduced. Sensitivity analysis (SA) will be examined for two various seismic characteristics of Kobe and Mid-Niigata earthquake regarding different magnitude scales and frequency content.

Sensitivity estimations via Monte Carlo simulations will be implemented for concerned response features. Reducing high dimension of selected features is desired to enable computing capacity of serviceable computers. The SA of modal responses via resonant modes was conducted in many previous studies. However, the implementation of SA in the time domain has not done much so far. In this section, weighted features in the time domain and frequency domain are adopted to global sensitivity analysis for uncertain model parameters of the isolated bridge pier. The procedure of sensitivity analysis for both earthquakes is summarized as in Fig. 5.1. The following chart starts with the original numerical model which was constructed in section 3.3.3, simulated response samples is created following an input set by Latin Hypercube sampling. These simulated results are weighted by the root mean square of response acceleration time-history and transfer ratios in the time domain and frequency domain, respectively. Later, global sensitivity analysis (GSA) using ANOVA theorem is conducted to obtain sensitivity effects or sensitivity indices. It is noticed that, unlike BSA presented in the previous chapter, the surrogate models are completely constructed before adopting them in GSA. In all cases of sensitivity analysis based on Monte Carlo simulations, convergence analysis is required to attain stable and precise sensitivity results.

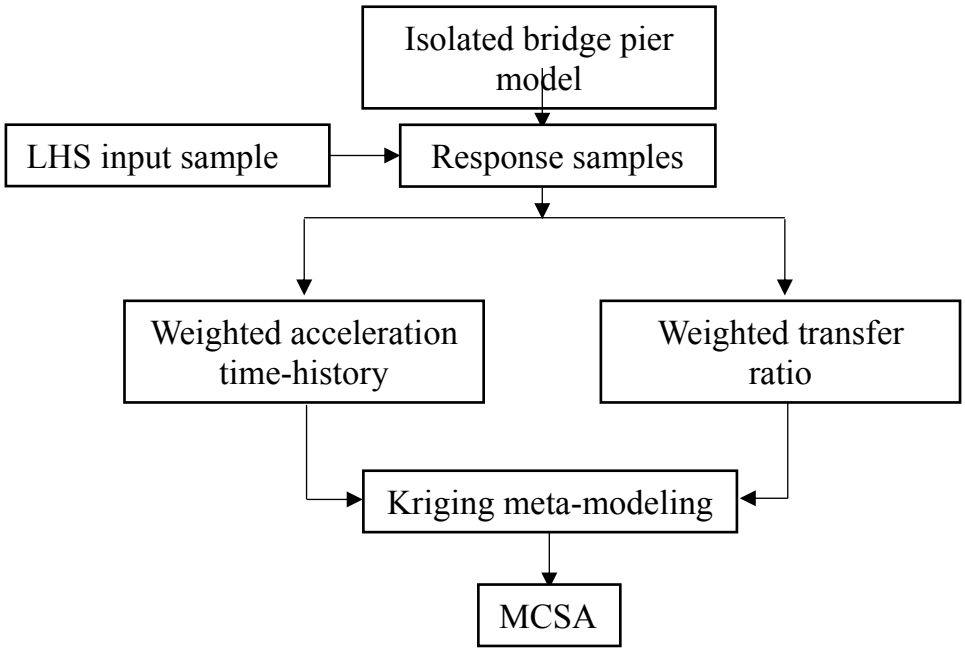

Fig. 5.1 Summarized procedure of Monte Carlo sensitivity analysis (MCSA)

5.1 Monte Carlo sensitivity analysis in Kobe earthquake

5.1.1 Kriging metamodeling

Kriging metamodels constructed based on the training samples of input parameters and corresponding outputs of the bridge. These metamodels can be used for SA to reduce computational cost. Various earthquake levels in Table 4 causes different nonlinear seismic responses, and hence developing the metamodels based on the training samples requires sample sizes are dissimilar. Leave-one-out (LOO) cross-validation (Stone, 1974) is used to measure the error of the metamodels. LOO error defines the average of discrepancy between simulated response by an input sample including all experimental points and the ones by the sample except a considered point. Smaller error values indicate better metamodels which are closer to the original model. Kriging metamodels were constructed whenever different response features chosen.

Considering surrogate models in case of time-domain features, while an experimental Latin Hypercube sampling (LHS) of size 200 is appropriate for constructing the metamodels with low errors ($E_{LOO} < 0.1$) for small EQs of 0.5%, 1%, 2%, 5% levels and very large EQs of 140% and 160%, larger training data of sizes from 300 to 900 is required for approximately similar accuracy of the remaining EQ levels, e.g., the metamodels of 25% and 30% levels necessitate sample sizes 900 and 700, respectively.

LOO errors are listed in Table 8. It is realized that the earthquake level of 25% causes the most dispersible variability of simulated responses based on training input data.

Similarly, the metamodels in case of transfer ratios were also validated via the LOO error. LOO errors are listed in

Table *9*. Error measures are slightly different from the case of selected features in the time domain in Table 8. The sample size of 650 is needed for earthquake scales of 20, 25 and 30% while others require less size. As presented in section 3.3.5, different earthquake levels are categorized into three groups in terms of PGA; group I, small EQs, 0-30 gal (0.5-5% levels); group II, large EQs, 30-210 gal (10-35% levels); and group III, very large EQs, more than 210 gal (40% level). In general, the large earthquakes from 90 to 240 gal defined as group II requires more training input data than group II and III for both features in the time domain and frequency domain.

Table 8. LOO errors of metamodels with RMS of acceleration time-history feature under different Kobe earthquake levels.

Scale (%)	PGA (gal)	Sample size	LOO error	
			RMS-Pier	RMS-Super.
0.5	3	200	0.098	0.020
1	6	200	0.098	0.020
2	12	200	0.098	0.020
5	30	200	0.098	0.020
10	60	300	0.096	0.015
15	90	600	0.112	0.014
20	120	650	0.107	0.021
25	**150**	**900**	**0.112**	**0.033**
30	180	700	0.102	0.027
35	210	600	0.107	0.025
40	240	600	0.098	0.025
50	300	550	0.102	0.049
60	360	550	0.102	0.049
70	420	550	0.105	0.041
80	480	400	0.093	0.022
90	503	400	0.096	0.018
100	600	300	0.086	0.021
120	720	500	0.068	0.011
140	840	200	0.052	0.011
160	960	200	0.037	0.009

Note: bolded numbers are the scale with a maximum sample size

Table 9. LOO errors of metamodels with RMS of acceleration transfer ratio under different Kobe earthquake levels.

Scale (%)	PGA (gal)	Sample size	LOO error
0.5	3	200	0.070
1	6	200	0.075
2	12	200	0.070
5	30	200	0.073
10	60	300	0.100
15	90	600	0.101
20	**120**	**700**	**0.091**
25	**150**	**650**	**0.076**
30	**180**	**650**	**0.045**
35	210	600	0.073
40	240	600	0.076
50	300	550	0.044
60	360	550	0.019
70	420	550	0.015
80	480	400	0.014
90	503	400	0.016
100	600	300	0.020
120	720	500	0.015
140	840	200	0.015
160	960	200	0.012

Note: Bolded numbers are scales with maximum sample sizes

5.1.2 Sensitivity analysis of RMS response acceleration time-history

Eight uncertain parameters consist of mass of the superstructure and pier, M_u, M_{rc}; initial stiffness, post-yielding stiffness and yield force of the pier, K_{rc1}, K_{rc2} and Q_{rc}; the ones of the isolators, K_{i1}, $K_{i2,}$ and Q_y, respectively. A ±10% uniform variability is assumed equally for all the parameters for sensitivity analysis. Training input data was created by random Latin Hypercube sampling. The selected features are root-mean-square (RMS) of response acceleration of the pier and superstructure.

Convergence analysis is critically required for SA based on random generation to obtain stable and precise results. The procedure describes in 4.1.3 using Central Limit Theorem (CLT) is only realistic when it is applied for a simple structure with few required

experimental tests and small parameter number. However, it is not suitable for complicated response surface or many cases required to check convergence. Since this study requires convergence analysis of each concerned feature for 20 earthquake levels; therefore, an alternative bootstrap method (Archer, Saltelli and Sobol, 1997) with less computational cost is chosen. Bootstrapping is adopted to get mean and confidence interval of main effects for each earthquake level. Assuming a m-size base sample, n resamples with replacement is constructed. Then, new statistical moments including mean and 95% confidence interval (CI) are calculated for each increase of base sample size. The advantage of this method is that resampling with replacement is conducted without any additional run on the models. Figure 5.2 shows convergence plots of eight parameters for acceleration time-history features of the pier and superstructure. Figure 5.2 and Fig. 5.3 points out how many model runs needed for converged sensitivity results of each parameter. A consideration of a total model run number is around 10^6 for RMS of acceleration time-history of the pier (RMS-Acc-pier) and a smaller number of 5×10^6 for the one of superstructure (RMS-Acc-Super.).

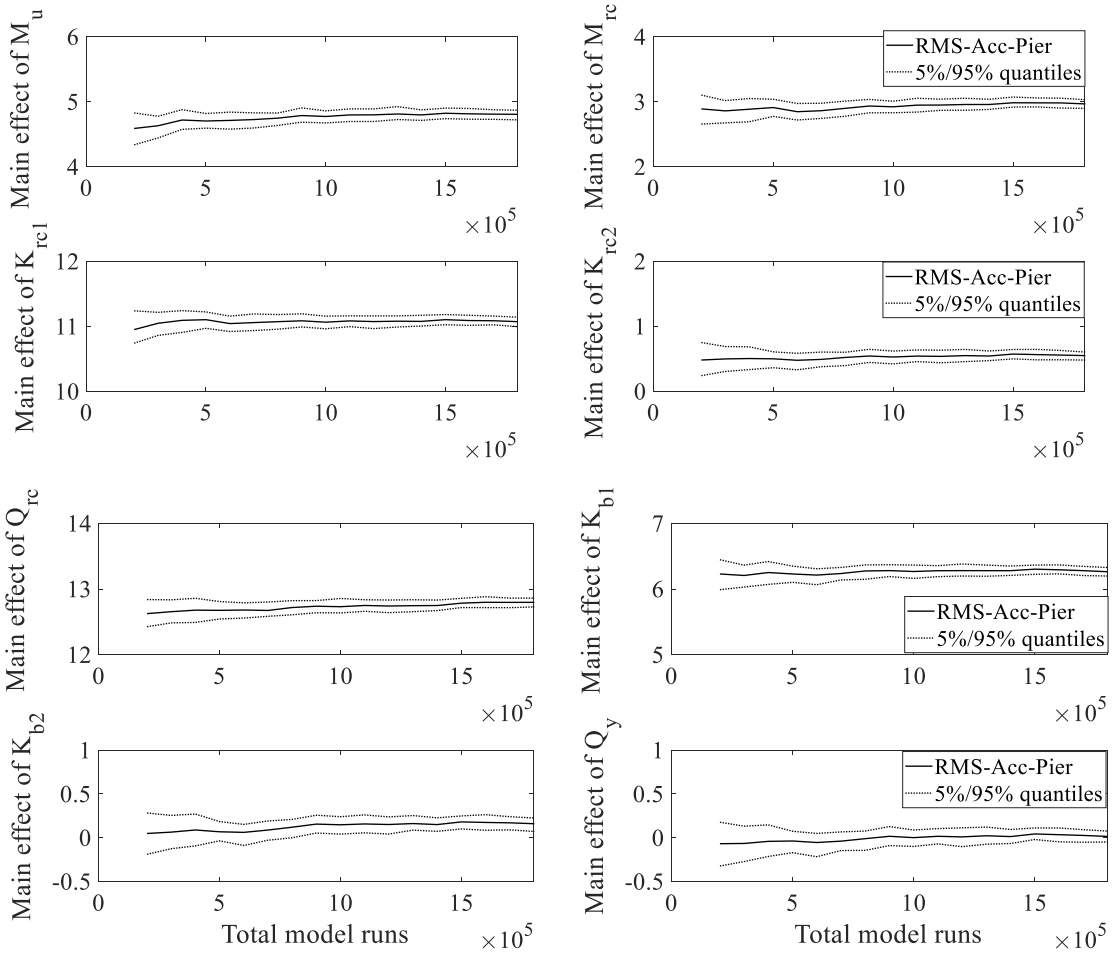

Fig. 5.2 Convergence plots performing mean and 5% and 95% quantiles of Bootstrap samples regarding RMS of pier acceleration time-history feature (RMS-Acc-pier).

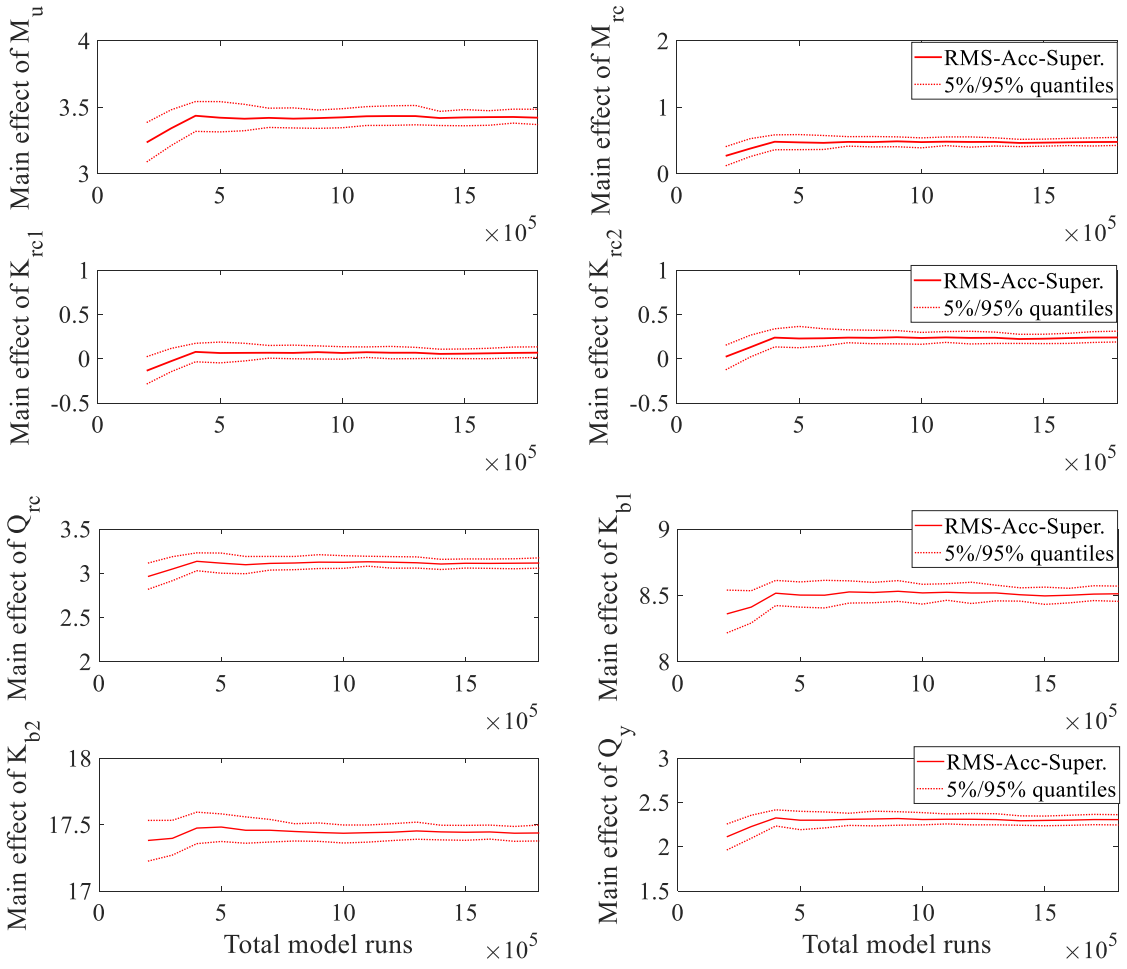

Fig. 5.3 Convergence plots performing mean and 5% and 95% quantiles of Bootstrap samples regarding RMS of superstructure acceleration time-history feature (RMS-Acc-Super.)

The time-history features including RMS of acceleration of the pier and superstructure with the 30 s time duration (T = 30s), termed as RMS-Acc-Pier, RMS-Acc-Super. are firstly considered. Figure 5.4 shows main and total effects of the model parameters under two selected seismic inputs including PGA 60 gal and 600 gal. The noninfluential parameters M_{rc}, and K_{rc} indicated by low total effects in both earthquakes can be fixed at their nominal values. Narrowing the dimensionality of input space can reduce computational expenses and high correlation between the parameters in the multi-variable inference, which will be presented in the next section. Moreover, factor ranking can be addressed by comparing main effects of the parameters under the same earthquake. For instance, the parameter M_u is specified as the most sensitive factor to RMS of acceleration time-history of the superstructure under PGA of 60 gal, K_{i2} holds the most influential parameter in the case of PGA 600 gal (the original earthquake). The difference in the sensitivity degree of the parameters under dissimilar earthquake magnitudes is expected to have a notable effect on the uncertainty of inference results in the next section.

Sensitivity degrees of chosen output features for each uncertain parameter under different earthquake magnitudes are performed via nonnormalized sensitivity effects, i.e., the numerators of Eq. (2.9). The main effect of the parameters has different trends for each seismic level group. High sensitivity is mostly found in group II and III. However, there are extreme points at which the effect decreases dramatically in the same group. For instance, sensitivity degree in group II significantly reduces at 25% level as considering the trend of M_u in terms of RMS of acceleration of the superstructure, then increases again to reach the peak value at 40%. The trend is like the lowest value at 60% level as considering K_{rc1} in group III. Moreover, the variability of nonlinear parameters K_{rc2}, K_{i2}, Q_{rc} and Q_y highly affect one of responses at large earthquakes in group III. Particularly, K_{rc2} is quite small compared with others. The indication of highly sensitive parameters in different earthquake levels can be helpful to obtain precise posterior densities which are presented in next section. In contrast, low sensitive parameters can be fixed to reduce the dimensionality of the input space. A well-known term for this in sensitivity analysis is called 'factor fixing'. More factors are fixed, SA is more efficient.

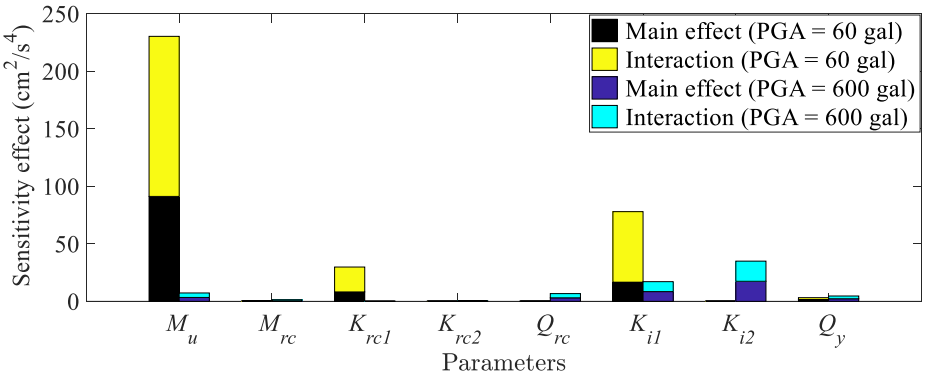

Fig. 5.4 Main effect and total effect (sum of main and interaction effects) of the model parameters against the RMS of acceleration time-history of the superstructure under two earthquake levels, PGA 60 gal (scale 10%) and PGA 600 gal (scale 100%, Kobe earthquake).

5.1.3 Sensitivity analysis of RMS acceleration transfer ratio

In this section, the SA procedure is carried out in the frequency domain. Selected features are weighted transfer ratios, i.e., RMS of acceleration transfer ratios. Transfer ratios were calculated from well-known transfer function or frequency response function between acceleration responses of the pier and superstructure in the frequency domain. Like SA in the time domain, eight parameters including M_u, M_{rc}, K_{rc1}, K_{rc2}, Q_{rc}, K_{i1}, K_{i2} and Q_y were considered. Latin Hypercube sampling technique with the assumption of ±10% uniform variability for each parameter was adopted to create training input data.

Figure 5.6 shows the unnormalized main effect of eight uncertain parameters in terms of RMS of transfer ratios. It is interesting that high sensitivity is found in small and very large earthquakes corresponding to group I and III. K_{i1} and K_{rc1} have high effect on the output responses in group I but small in group III. It is because the linear response is predominant at smaller earthquake levels in group I. In contrast, $K_{i2,}$ $Q_{rc,}$ and Q_y have high sensitivity in group III but small in group I since high nonlinearity occurs in larger earthquakes. Particularly, the least sensitivity happens at K_{rc2} with the computed main effect being nearly zero. Hence, it is predicted that the uncertainty of this parameter cannot be reduced effectively in Bayesian statistics, which will be presented in chapter 6. This parameter can be hence fixed at its nominal value in global sensitivity analysis.

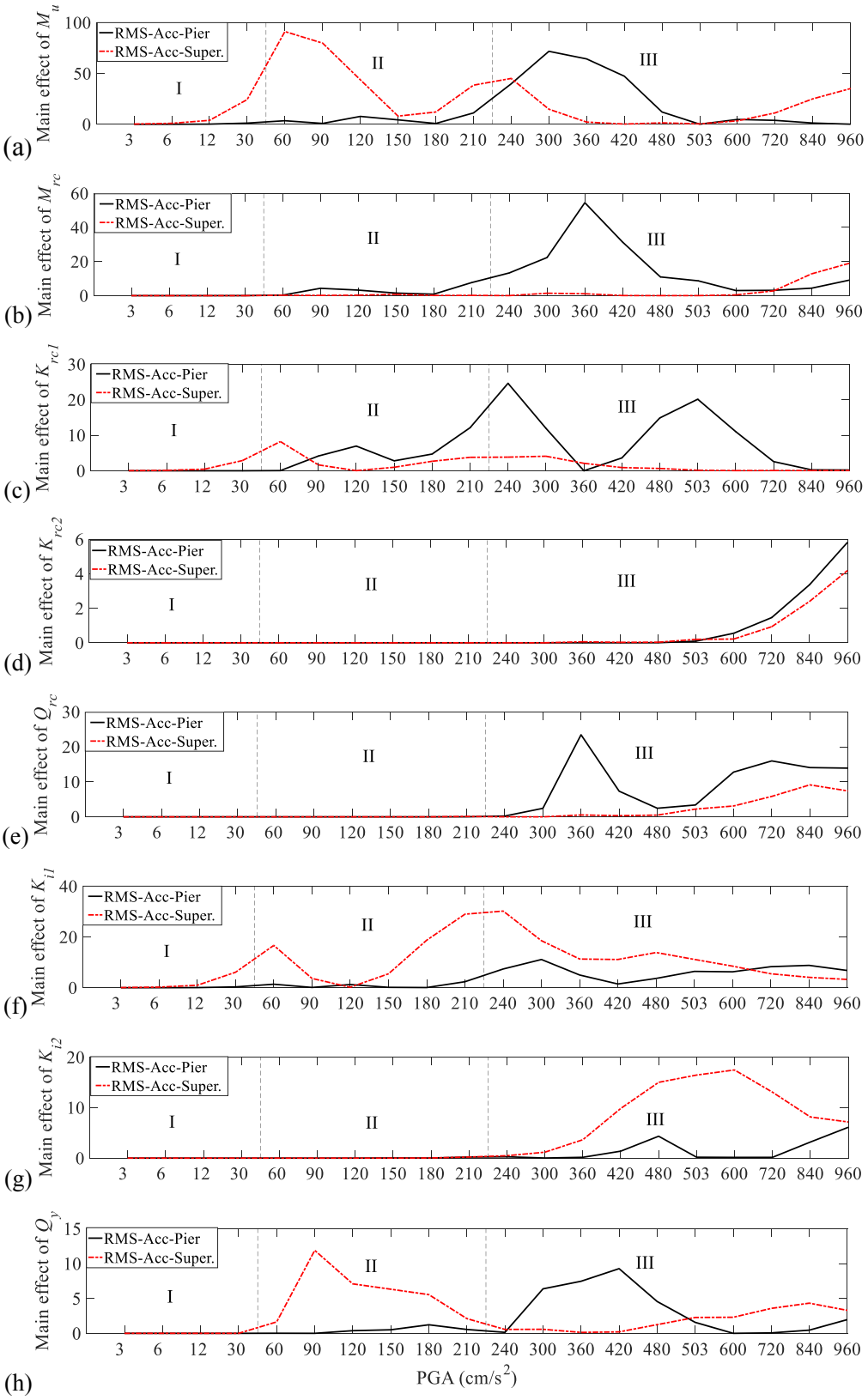

Fig. 5.5 Unnormalized main effect of eight uncertain parameters in terms of RMS acceleration time-history: (a) M_u, (b) M_{rc}, (c) K_{rc1}, (d) K_{rc2}, (e) Q_{rc}, (f) K_{i1}, (g) K_{i2}, and (h) Q_y in various earthquake levels with different scale (%) of the Takatori earthquake. (Unit: (cm/s^2)^2)

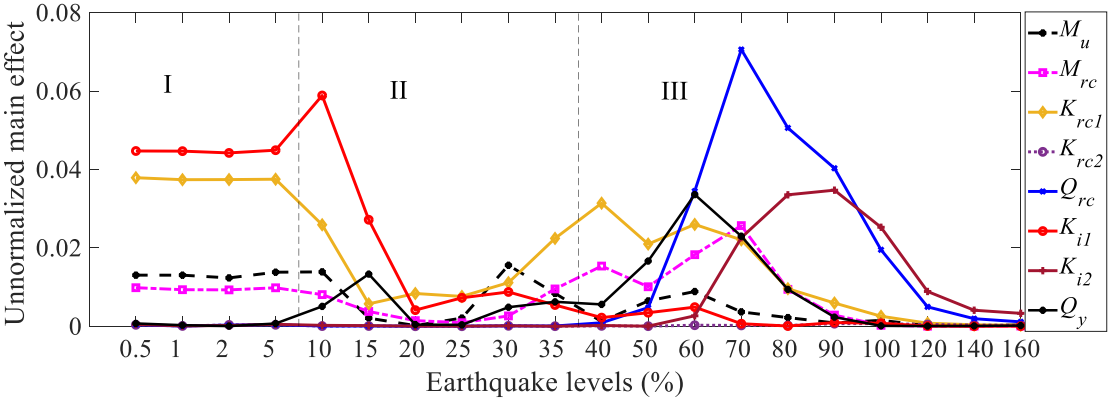

Fig. 5.6 Unnormalized main effect of eight uncertain parameters *Mu, M_{rc},, K_{rc1}, K_{rc2}, Q_{rc}, K_{i1}, K_{i2},* and Q_y in terms of RMS of transfer ratios in various earthquake levels with different scale (%) of Takatori earthquake.

5.2 Monte Carlo sensitivity analysis (MCSA) in Mid-Niigata earthquake

Sensitivity analysis using Kriging metamodels for Mid-Niigata earthquake, which is same to MCSA for Kobe earthquake, was also conducted following the procedure in Fig. 5.1. A uniform variability of ±10% was applied for eight uncertain parameters M_u, M_{rc}, K_{rc1}, K_{rc2}, Q_{rc}, K_{i1}, K_{i2} and Q_y. In this section, Kriging metamodeling and GSA for the response in time domain and frequency domain under Mid-Niigata earthquake are presented.

5.2.1 Kriging metamodeling

Kriging metamodels in terms of RMS acceleration time-history and RMS transfer ratios are constructed for different earthquake levels, as shown in Table 10. Since the impact of the high-frequency earthquake on the structure is insignificant, the response of structures under large earthquakes is almost linear. The requirement of training sample size is equally 200 for all the cases. Three large earthquakes with PGA of larger than 700 cm/s^2 have LOO error of around 0.11 in terms of RMS of response acceleration of the pier, the error of the others is quite small. This demonstrates that the surrogates have high accuracy with limited input samples.

Table 10. LOO errors of metamodels under different Mid-Niigata earthquake levels.

Scale (%)	PGA (gal)	Sample size	LOO error	
			RMS-Pier	RMS-Super.
0.17	3	200	0.039	0.085
0.35	6	200	0.037	0.083
0.7	12	200	0.038	0.083
1.75	30	200	0.038	0.086
3.5	60	200	0.038	0.082
5.25	90	200	0.037	0.082
7	120	200	0.043	0.079
8.74	150	200	0.038	0.084
10.5	180	200	0.037	0.083
12.24	210	200	0.037	0.084
14	240	200	0.037	0.082
17.49	300	200	0.037	0.085
20.93	360	200	0.041	0.083
24.42	420	200	0.038	0.081
27.92	480	200	0.036	0.083
29.32	503	200	0.039	0.083
34.92	600	200	0.039	0.090
41.97	720	200	0.106	0.054
48.97	840	200	0.113	0.053
55.96	960	200	0.071	0.058

5.2.2 Sensitivity analysis of weighted response acceleration time-history

Figure 5.7 shows unnormalized main effect of eight uncertain parameters under the same earthquake levels with the case of Kobe earthquake. In general, the sensitivity of model parameters under Mid-Niigata earthquake is quite small in comparison with the one of Kobe earthquake. The parameters M_{rc} and K_{rc1} are highly sensitive parameters with the gradual increase of main effect according to the rise of magnitude (PGA). However, the trend suddenly decreases at PGA of 720 cm/s^2 and increase again since this coincides with the transform of nonlinear response characteristics of the pier starting at that level, as previously analyzed in section 3.3.5. It is reasonable to realize that most of the parameters are sensitive to RMS of acceleration time-history of the pier except that the variance of M_u actively affects RMS of acceleration of the superstructure. It is because the isolation system placing on the pier top is not well-functioned under this earthquake.

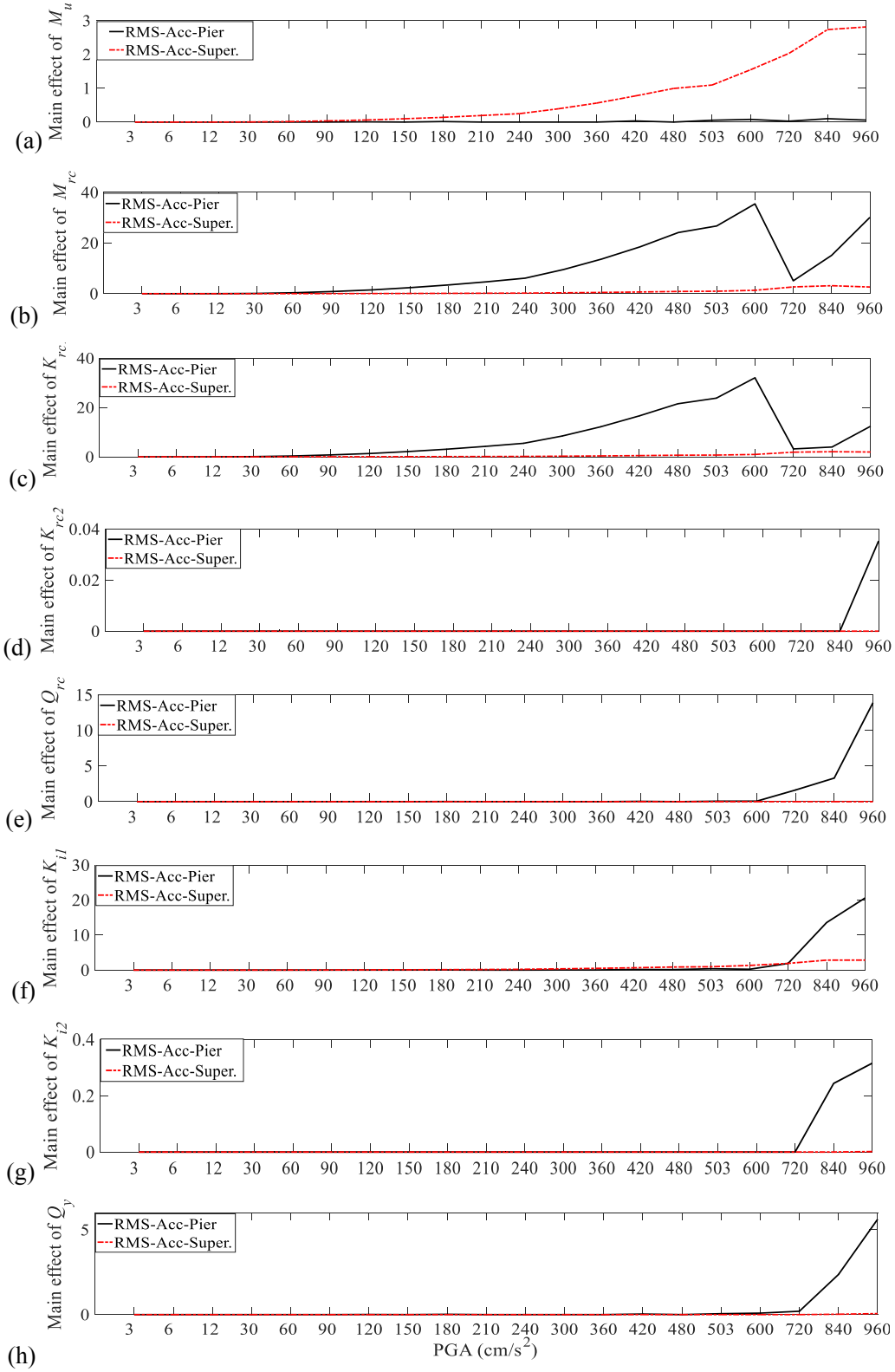

Fig. 5.7 Unnormalized main effect of eight uncertain parameters in terms of RMS acceleration time-history: (a) Mu, (b) M_{rc}, (c) K_{rc1}, (d) K_{rc2}, (e) Q_{rc}, (f) K_{i1}, (g) K_{i2}, and (h) Q_y in various earthquake levels with different scale (%) of Niigata earthquake. (Unit: $(cm/s^2)^2$)

5.2.3 Sensitivity analysis of weighted acceleration transfer ratios

The process of sensitivity analysis for RMS of the transfer ratio between the superstructure and pier acceleration under varying seismic levels of Mid-Niigata earthquake was performed similarly to the one of Kobe earthquake in section 5.1.3. While Fig. 5.6 shows quite large bias between different magnitudes, Fig. 5.8 depicts insignificant effect on RMS of the transfer ratios at nonlinear parameters K_{rc2}, Q_{rc}, K_{i2}, Q_y and the mass of the supertructure M_u. Whereas, linear parameters K_{rc1}, K_{i1}, and M_{rc} has higher sensitivity, especially for nearly equal effects to the transfer ratios for almost all levels except few levels of very large magnitudes being larger than 800 cm/s^2.

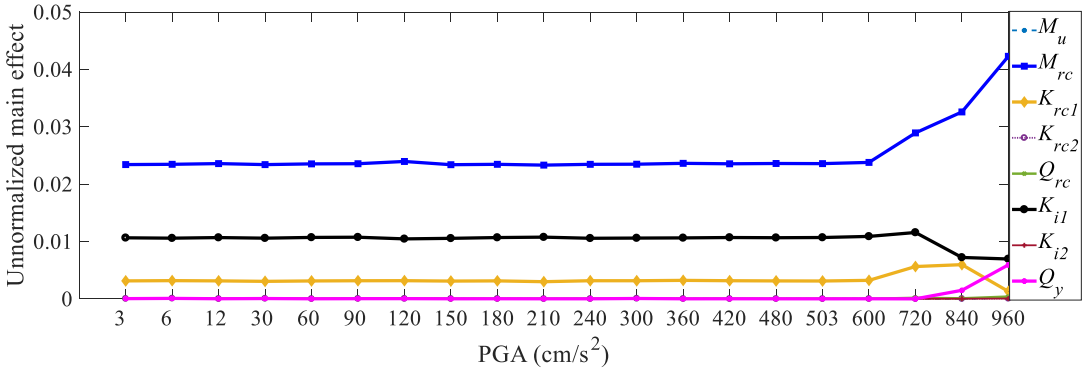

Fig. 5.8 Unnormalized main effect of eight uncertain parameters *Mu, M_{rc},, K_{rc1}, K_{rc2}, Q_{rc}, K_{i1}, K_{i2},* and Q_y in terms of RMS of transfer ratios in various earthquake levels with different scale (%) of Mid-Niigata earthquake.

Chapter 6

Uncertainty quantification

Uncertainty quantification (UQ) for model updating of target existing structures is applied in this study. The uncertainty of the structures stems from structural changes under large earthquakes or the epistemic uncertainty due to lack of knowledge in modeling process. Results of UQ returns probabilistic distributions (posteriors) after involving both prior knowledge and real observations inverse uncertainty propagation in the Bayesian framework. The inference implemented under an earthquake event may not result in precise densities for all concerned model parameters due to different sensitivity degree of each under varying seismic characteristics. Therefore, utilizing data acquisition of many earthquakes is helpful for this problem. Moreover, generating random walks in Markov Chain Monte Carlo (MCMC) scheme requires advanced algorithms to solve problems of multimodality, high dimensionality for highly nonlinear dynamic models. Therefore, two methods including a traditional MCMC using Metropolis-Hasting updates and Different Evolution Adaptive Metropolis (DREAM) were used to implement the Bayesian inference in this chapter. Two software packages with MATLAB coding implementation, GPM/SA using the traditional MCMC (Higdon *et al.*, 2008) and the DREAM_ZS adopting the DREAM algorithm (Vrugt, 2016) were used for the inverse propagation. GPM/SA is applied on the existing base-isolated building under a specific earthquake events, while DREAM_ZS is for the isolated bridge pier in Japan Design Specifications of Highway Bridge (JRA, 2012) using response data from various seismic characteristics.

6.1 Uncertainty quantification using Markov Chain Monte Carlo algorithm (MCMC)

Bayes' theorem is generally described following the formula in Eq. 2.15 or a normalized one in Eq. 2.16 to infer posterior densities. In GPM/SA software, the metamodels are developed parallel with the inference process. The procedure of Bayesian inference via the inverse propagation of the uncertainty is implemented by MCMC using Metropolis-Hasting updates. The method was proposed by Kennedy and O'Hagan, 2000 for the univariate system and expanded for multi-variate systems by Higdon *et al.*, 2008.

The Bayesian inference procedure follows the sensitivity analysis of the base-isolated building on eight local stiffness parameters K_{B1}, K_{B2}, K_{Cb1}, K_{Cb2}, K_{Ca1}, K_{Ca2}, K_{C1}, and K_{C2} under the earthquake on September 21, 2011 in section 4.2.2. Stiffness parameters at the lower floors of the building K_{Ca1}, K_{C1}, K_{Cb1}, and K_{B1} has higher sensitivity than ones of the upper floors. It is also predicted that the lower parts have a higher possibility of stiffness reduction than others do. Therefore, uncertainty quantification was implemented for four stiffness parameters K_{Ca1}, K_{C1}, K_{Cb1}, and K_{B1} at the lower part of the structure. Based on bar plot of total sensitivity indices in Fig. 4.11, measured data at sensors C104, C106, C108 in the X direction, and B105 in the Y direction are chosen for UQ of K_{Ca1}, K_{C1}, K_{Cb1}, and K_{B1}, respectively.

The first crucial step in the inference procedure is to predict the prior distributions of the concerned parameters. Herein, the priors were represented by uniform distributions with an assumption of ±10% variance equally for all the parameters. Input samples size 200 were created by Latin Hyper Cube sampling on the uniform distributions. Structural responses were simulated for the input samples.

Field data was acquired from sensors installed on the building. For each earthquake, we can collect only one data set from each sensor. This is disadvantage in the Bayesian inference since all updates are based on measured data associated with the uncertainty in probabilistic scheme. Moreover, noise always exists in the field data. Therefore, an indication of noise presence is required. In this study, noise of observed data was assumed to be equal to RMS of acceleration time history in last 10 seconds of the vibration. Normal distribution with zero mean and standard deviation of approximately 0.0005 m/s^2 was assumed for all sensing data.

It should be careful about how precise the calibrated prediction is. Hence, visual check was done to detect any strange outlier between the field data can the calibrated prediction based on the reduced models. The simulators $\eta(x)$ were constructed from Gaussian process in section 2.1. The modeling error was involved to the Bayesian implementation by adding the discrepancy $\delta(x)$ in Eq. 2.16 to the simulator. Figure 6.1 shows the calibrated simulator, prediction and the discrepancy between the simulator and actual data considering measured data from sensor B105 in the Y direction. The sum of the calibrated simulator in Fig. 6.1 (a) and discrepancy is known as calibrated prediction in Fig. 6.1 (b). Since the discrepancy between the simulator and the actual response is quite small, adjusted features seem not clearly different from the calibrated simulator. Note that the actual response was assumed by the mean of the system output. It can be concluded that the surrogate models are adequately accurate to represent the actual response of the structure.

As the procedure presented in section 2.3, maximum likelihood acceptance criteria play a crucial role to decide whether a proposal point in MCMC moves to a next point or

stay at the current point. Herein, the key role of MCMC is to draw samples from further posteriors and keep moving forward to the target distribution. The process is implemented until obtaining stable posterior distributions. A single-chain MCMC using Metropolis-Hasting updates was applied to calculate the posteriors in Eq. 2.17. As all traditional methods based on Monte Carlo simulation, MCMC requires to analyze convergence to ensure the stability of the target posterior distributions. Some convergence diagnostics such as using trace plots, and correlation analysis were used.

The MCMC presented in this section was implemented with the total 75000 iterations including 25000 burn-in runs. Figure 6.2 shows trace plots of the parameters in MCMC procedure. The convergence was obtained before the stage of the burn-in process completed. In other words, a shorter length of 10000 runs can be applied for saving the computational time and storage capacity. Moreover, the draws for the eight parameters shows the randomness which can be a measure of the convergence, as shown in Fig. 6.3. Another convergence diagnostic is to use autocorrelation function to demonstrate independent draws in a trace. Figure 6.4 depicts very low correlation at lag 25 for all the parameters. It is hence concluded that 50000 walks after discarding the initial stage of burn-in is good to obtain reliable UQ results.

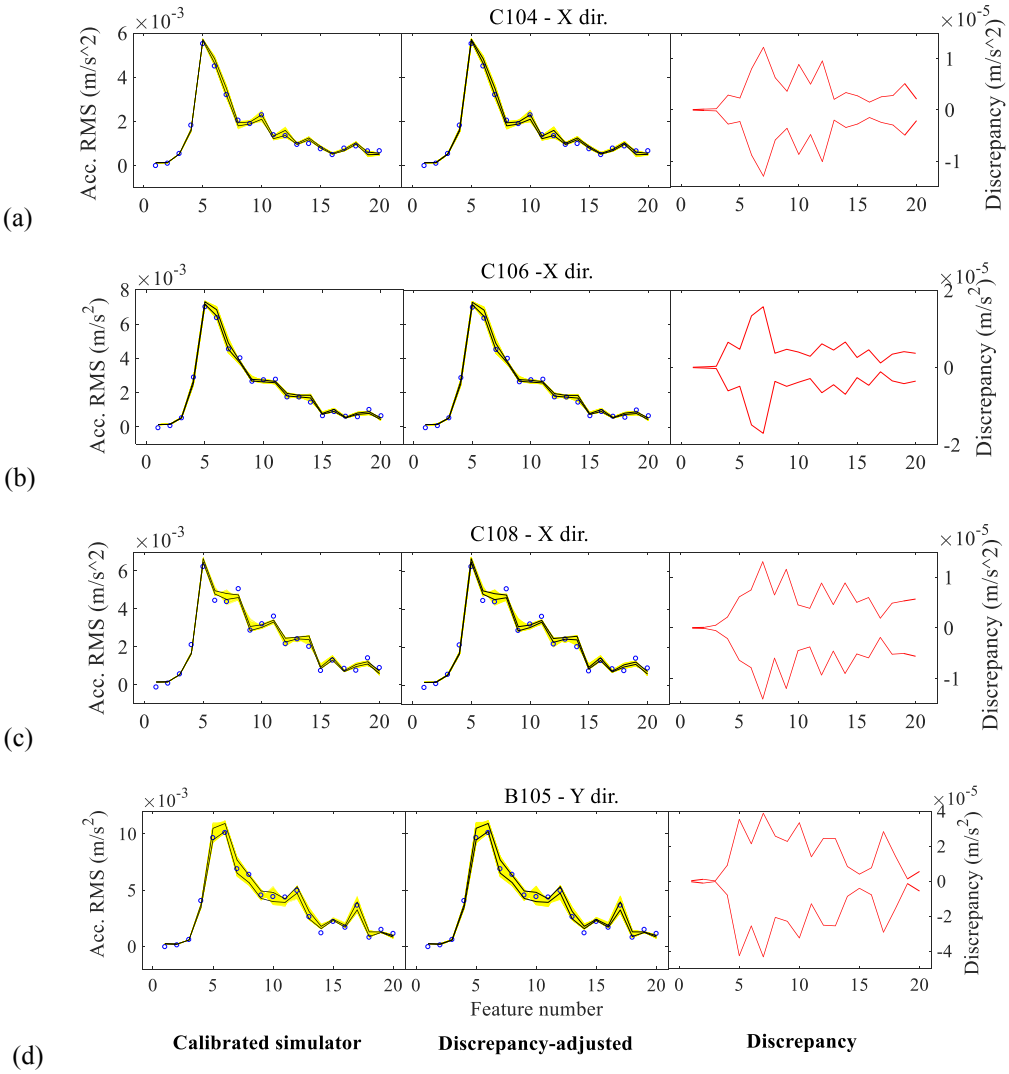

Fig. 6.1 Calibrated simulator and the discrepancy between the simulator and the actual response of the base-isolated building using field data from (a) sensor C104 in X dir., (b) sensor C 106 in X dir., (c) sensor C108 in X dir., (d) sensor B105 in Y dir. (blue circles are the field data at sensor 105 in Y direction, the black lines shows 5% and 95% pointwise quantiles of confidence interval of the simulator, yellow lines are the output responses computed from the LHS samples).

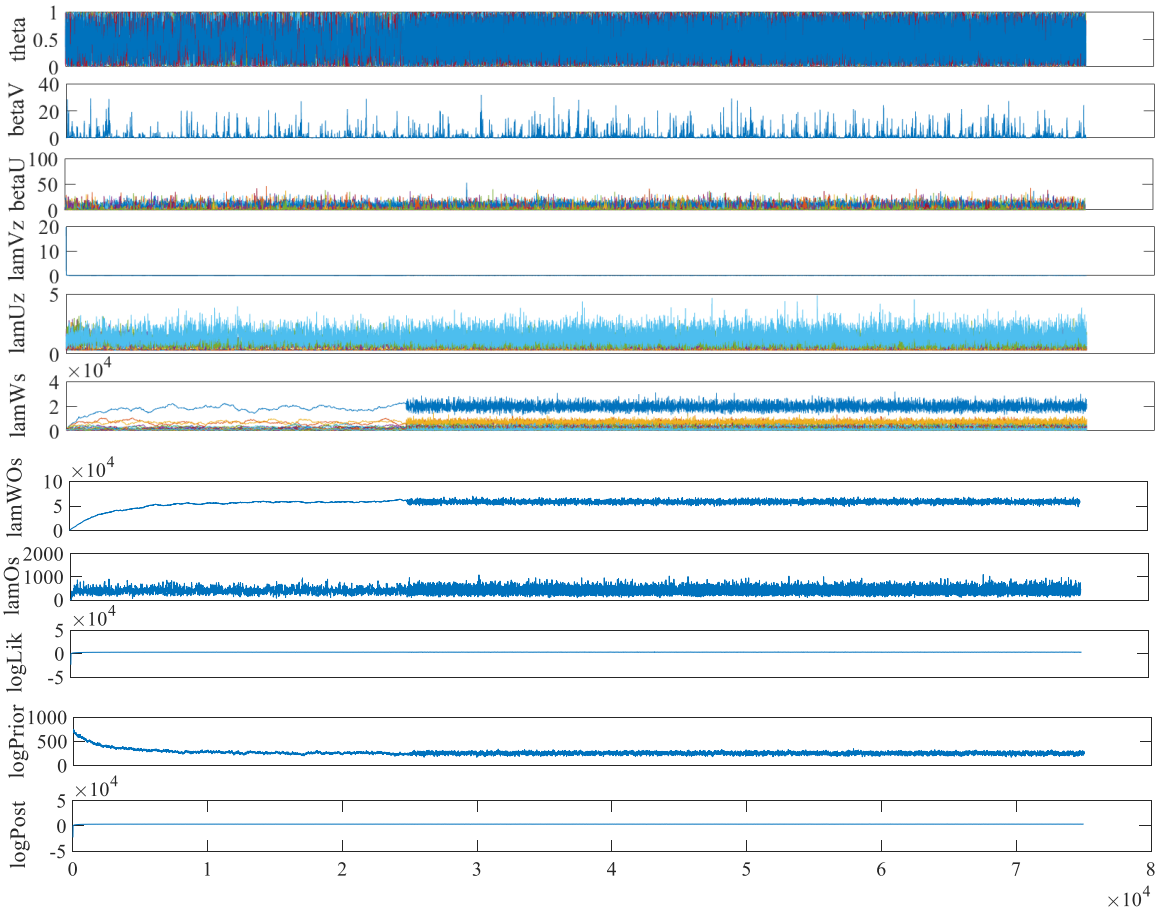

Fig. 6.2 Trace plots of hyperparameters of MCMC draws with betaV, betaU, lamVz, lamUz, lamWs, lamWOs, lamOs, logLik, logPrior, LogPost being hyperparameters defined in MCMC process.

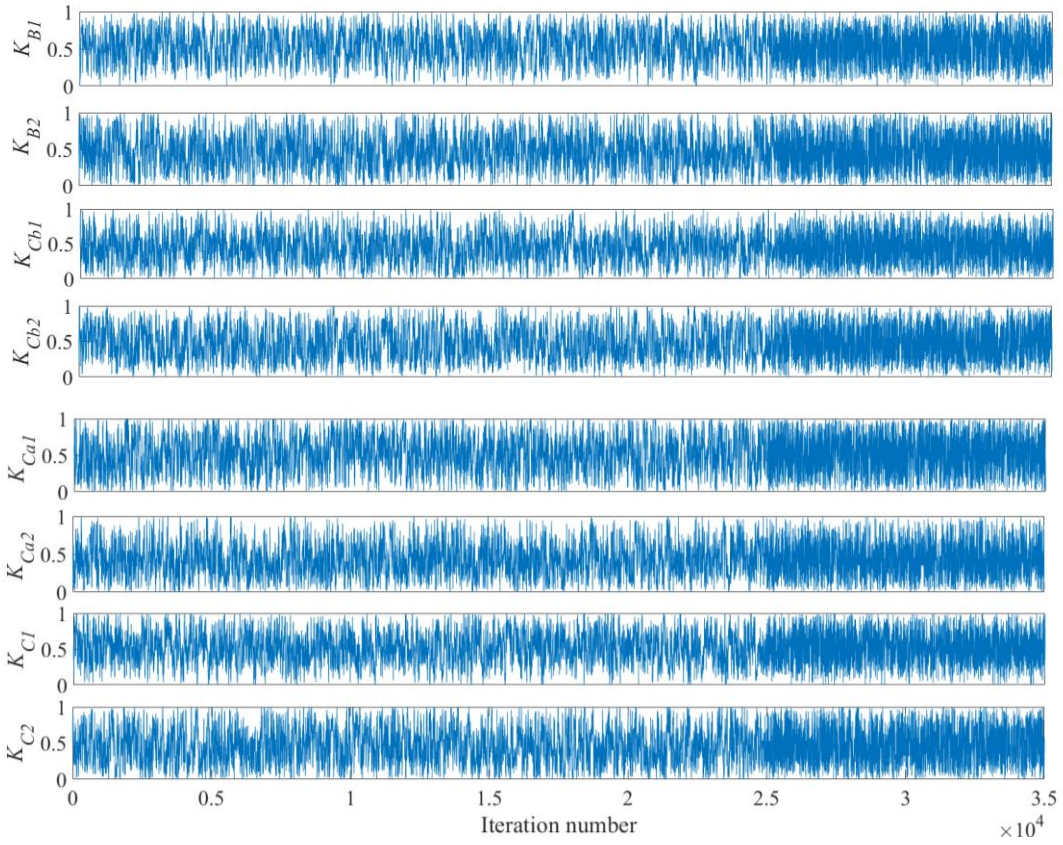

Fig. 6.3 Trace plots of draws of the eight parameters K_{B1}, K_{B2}, K_{Cb1}, K_{Cb2}, K_{Ca1}, K_{Ca2}, K_{C1}, and K_{C2} regarding RMS of acceleration time-history of sensor 105 in the Y direction under the earthquake 21th September, 2011, (note: Y axis shows sample values of the parameters normalized in $[0,1]^d$).

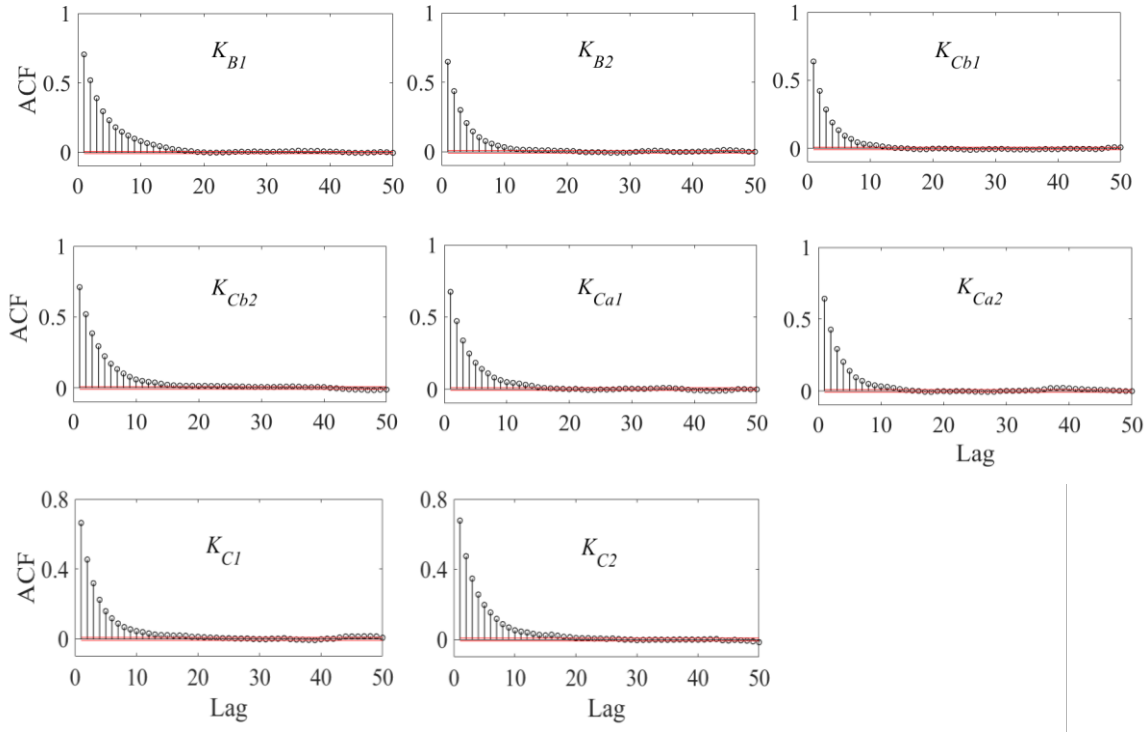

Fig. 6.4 Sample autocorrelation of eight model parameter K_{B1}, K_{B2}, K_{Cb1}, K_{Cb2}, K_{Ca1}, K_{Ca2}, K_{C1}, and K_{C2} regarding RMS of acceleration time-history of sensor 105 in the Y direction under the earthquake 21th September, 2011, (note: 95% confidence interval is in red color)

The resulting posterior distributions using data from sensor B105 in the *Y*-direction under 21th Sep. 2011 earthquake are shown in Fig. 6.5. The posterior density of the parameter K_{B1} is better constrained by the data than others. It is because the variability K_{B1} has larger effect on the output at sensor B105 than others do. The parameters are less sensitive, their posterior distributions tend to have similar shape with the prior' ones. However, the shape of K_{B1} still does not have clear tails of a Gaussian distribution. The UQ results using data from sensors C104, C106, C108 in the *X*-direction also indicates unexpected results, as shown in Fig. 6.6. It is hence concluded that acquired data under the small earthquake on 21th Sep. 2011 is not appropriate to update the model parameters. Moreover, the inference using one earthquake event was not able to update all parameters of interest. In the next section, the Bayesian inference will be implemented using the innovated algorithm DREAM using response data from more than one earthquake with different characteristics in magnitudes and frequency content. The DREAM is expected to overcome the limitations of the traditional MCMC such as multi-modality, increasing the mixing speed of drawn samples.

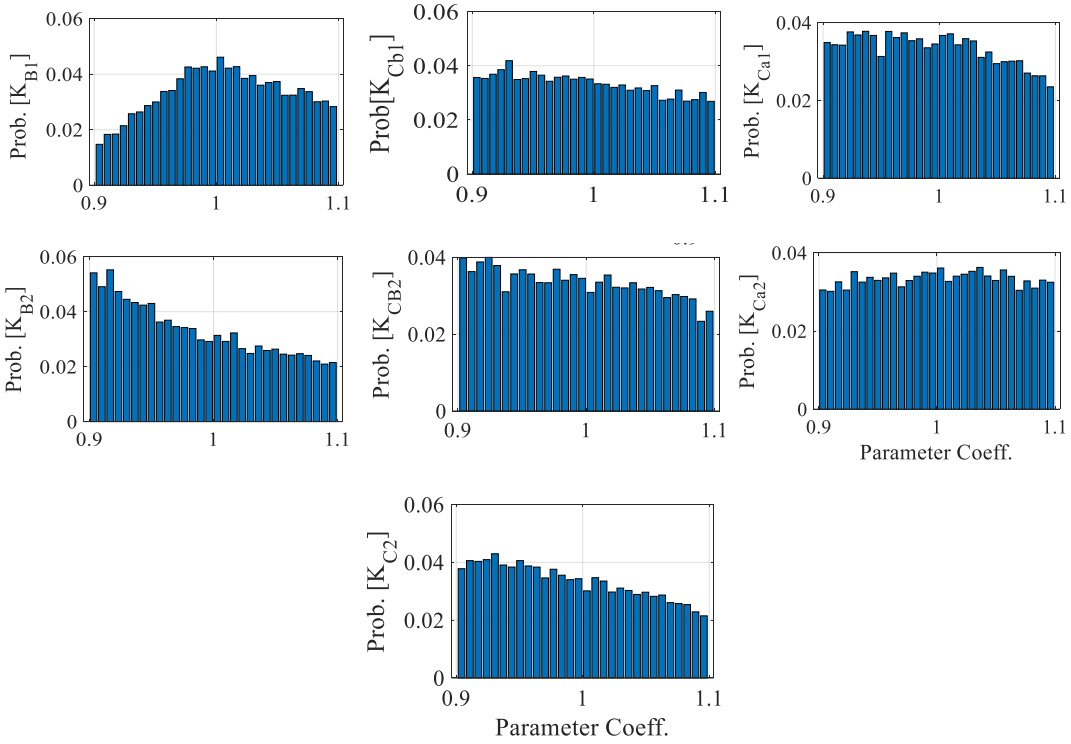

Fig. 6.5 The posterior distributions of eight stiffness parameters K_{B1}, K_{B2}, K_{Cb1}, K_{Cb2}, K_{Ca1}, K_{Ca2}, K_{C1}, and K_{C2} regarding RMS of acceleration time-history of sensor B105 in the Y direction under the earthquake 21th Sep. 2011.

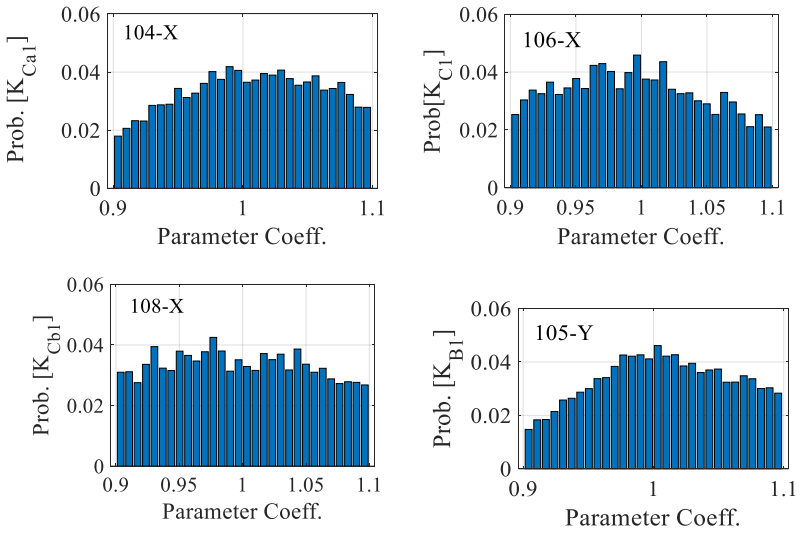

Fig. 6.6 The posterior distributions of four stiffness parameters K_{B1}, K_{Cb1}, K_{Ca1}, and K_{C1} regarding RMS of acceleration time-history of sensor B105 in the *Y* direction, sensor C104, C106, and C108 in the *X* direction, respectively under the earthquake 21th Sep. 2011.

6.2 Uncertainty quantification using Differential Evolution Adaptive Metropolis algorithm (DREAM)

Updating all uncertain input parameters by simulating the optimal posterior distributions is essential to achieve a properly updated model. However, it is not always able to update all the parameters with high reliability without using more than one seismic response data induced by different earthquakes. For this reason, the parameter uncertainty of the isolated bridge was quantified using the response data from different levels of Kobe earthquake. The reason to choose this earthquake is because its seismic characteristics including the magnitude and frequency content cause damage-sensitive behavior on the structure. Unlike many previous studies using modal responses extracted at dominant modes in the Bayesian inference (Nishio et al., 2012; Au, 2012), this study quantifies the uncertainty using the responses in both time domain and frequency domain. Since no clear peak can be realized in the nonlinear responses by modal feature extraction, e.g. peak amplitudes in Fourier transfer functions, it is challenging to point out the dominant frequencies. To cope with this problem, an alternative solution is to use transfer ratios corresponding to all frequencies less than 5 Hz. Another solution is to use the responses in time domain by taking RMS of acceleration time-history for small time segments. This is because the incapability of constructing the metamodels and quantifying the uncertainty with very high-dimensional time-history features. However, the usage of the weighted time-history responses needs to be verified to ensure that there is no significant bias between its derived posteriors and "given true" values. The implementation of Bayesian inference is conducted using the DREAM algorithms (Vrugt *et al.*, 2008; Vrugt *et al.*, 2009) encoded in DREAM software package (Vrugt, 2016). The algorithm is an enhancement of MCMC. The important reason of use is that multi-chain DREAM algorithm can overcome limitations of the traditional MCMC adopted in section 6.1. DREAM can solve posterior sampling problems such as bimodality and nonsymmetric of the posterior distributions. The UQ procedure is briefly introduced in Fig. 6.7.

In this section, the authors firstly demonstrate that the significantly sensitive parameters against the extracted response features which found in different earthquake magnitudes will have more precise posterior densities than ones whose variability have less impact on the responses. As a result, the accuracy of UQ results can be verified based on this clarification. The optimal posterior for each parameter can be then generated using response data acquired from different earthquakes. Finally, a sequential uncertainty quantification procedure using the long-term monitoring data is developed, which is expected to be applicable for any structures including building and bridges.

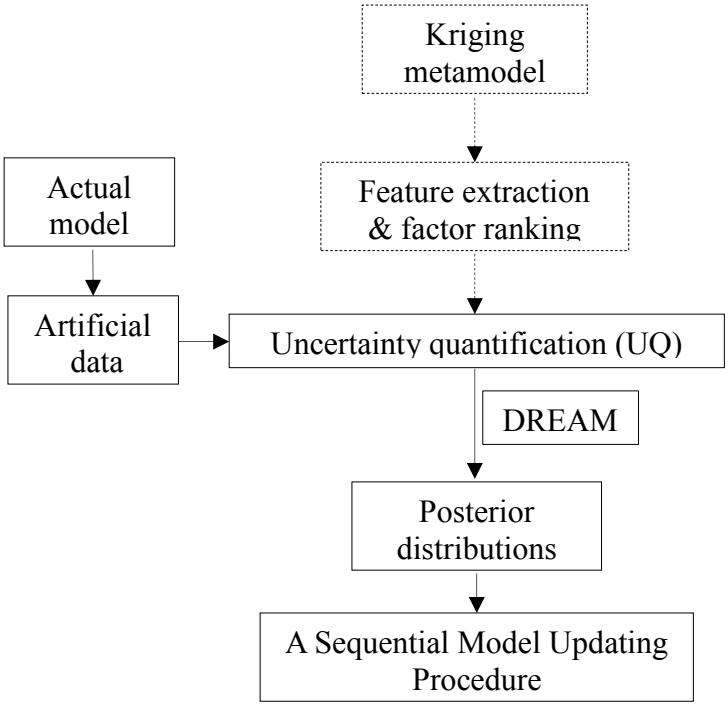

Fig. 6.7. The procedure of Bayesian uncertainty quantification

6.2.1 Posterior distribution verification using Kobe earthquake response data

The precision of the posterior distributions needs to be verified under two scenarios: (1) the applicability of the Bayesian inference using weighted time-history responses, (2) the effect of sensitivity evaluations on the reliability of derived posterior densities. To cope with these issues, two seismic levels, 10% and 100% corresponding to PGA 60 and 600 gal were adopted to excite the bridge in its longitudinal direction. Two major ingredients which are most concerned in the inverse propagation in Eq. (2.17) constitute the prior knowledge on the parameter uncertainty and the choice of the observed data. The prior knowledge about the inputs was assumed to be uniform distributions produced by Latin Hypercube sampling in a limited range of ±10% variability. To facilitate the inverse inference, the sample values were normalized by coefficient bounds between 0.9 and 1.1, with 1 being nominal coefficient. The observed data was created by adding white noise to the acceleration time-history and performed as normal distributions, as presented in section 3.3.6. These observations were exhibited by features in both time domain and frequency domain. The verification will be conducted with the assumption that the structure is in an undamaged condition.

Convergence diagnostics

The Bayesian inference in Eq. (2.17) was implemented by the DREAM algorithm, which is an enhancement of the traditional MCMC to generate samples from complex multi-modal posterior distributions. The total of 30 weighted responses taken by RMS of acceleration time-history for each 1s and 40 transfer ratios between the response acceleration of the superstructure and pier corresponding to the frequencies less than 5 Hz, respectively. Some diagnostics adopted include qualitative methods such as trace plots, convergence rate, and autocorrelation, and quantitative method as multi-chain $\hat{R}$-statistic of (Gelman and Rubin, 1992). The convergence diagnostics using $\hat{R}$-statistic is known as the most powerful tool as it can indicate when the sampled chains have been obtained the limiting distributions. A $\hat{R}$-statistic of 1.2 can be considered as a good proxy to diagnose how many samples can be discarded as burn-in, and the remaining samples can be used to build up the posterior distributions. Herein, convergence analysis results are shown for an example case of the original Kobe earthquake (PGA = 600 gal). The selected output feature is RMS of superstructure acceleration time-history for each 1s. The observed data was assumed to be the response of the actual model with input parameters designed at nominal coefficients under the undamaged condition. The observations were normal distributions with zero mean and 0.05 gal standard deviation (SNR = 40 dB).

Convergence analysis must be done for every MCMC using DREAM algorithm in different seismic loadings. In this section, the analyses were performed for both PGA 60 and 600 gal. However, only the case of PGA 600 gal is presented here for basic explanation of the uncertainty quantification procedure. The trace plots in Fig. 6.8 depict generations of each chain with different starting points. Figures show good mixing between the Markov chains after less than 1000 samples, i.e., 5000 runs for burn-in discarded. On the other hand, as shown in Fig. 6.9, autocorrelation analysis for each parameter indicates small correlation coefficients of nearly zero at lag 30. Some parameters can be tolerated to consider autocorrelation at lag 50. This is not strictly required to predict the convergence since this method cannot determine when the convergence is obtained. Another proxy for convergence diagnostics is considering the acceptance rate which can dictate the mixing speed convergence rate. Figure 6.10 indicates the rate is larger than 10% which can be considered as efficient mixing of the chains. The convergence evaluation via $\hat{R}$-statistic indicate the convergence happens at early 20000 runs. As above analyzed, the total 50000 iterations including 5000 burn-in with a thinning interval of 5 can be called through MCMC.

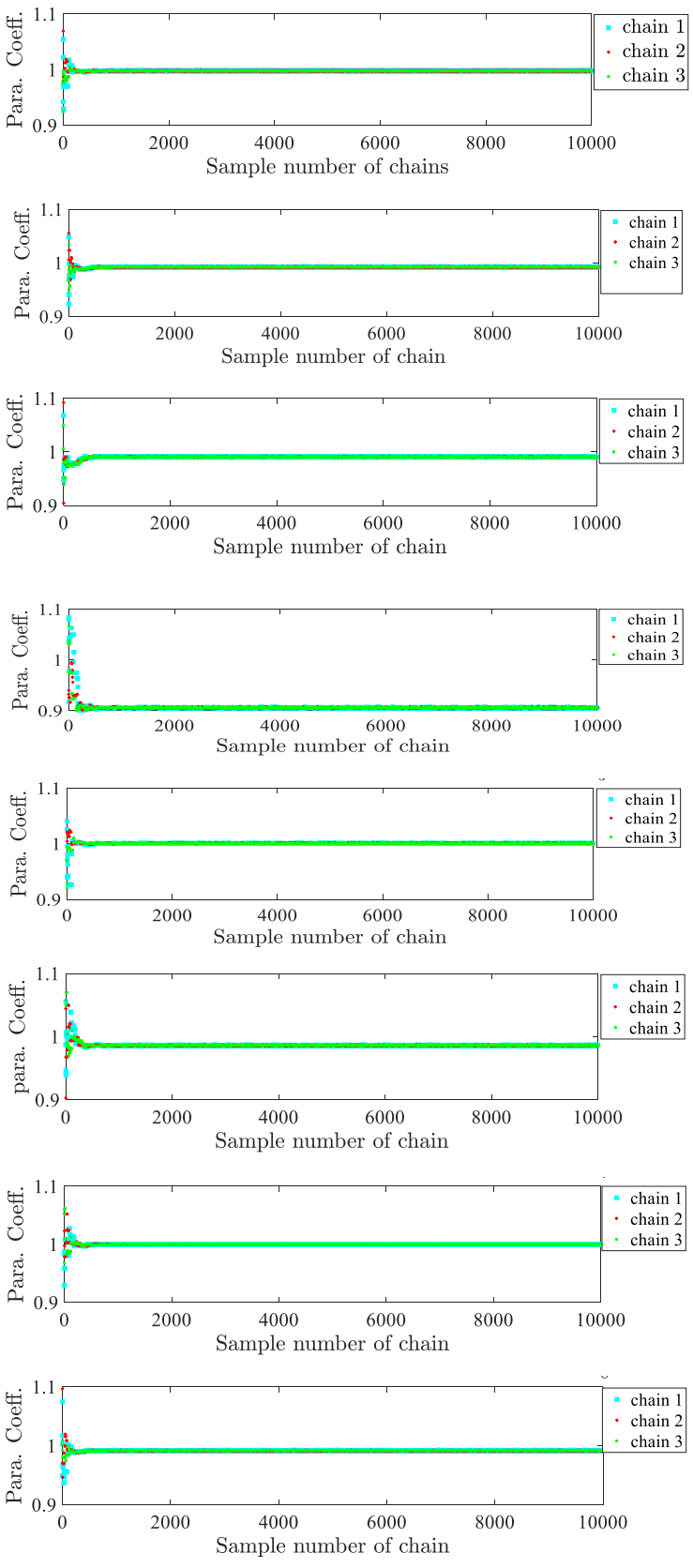

Fig. 6.8 Chain convergence plot of the parameters

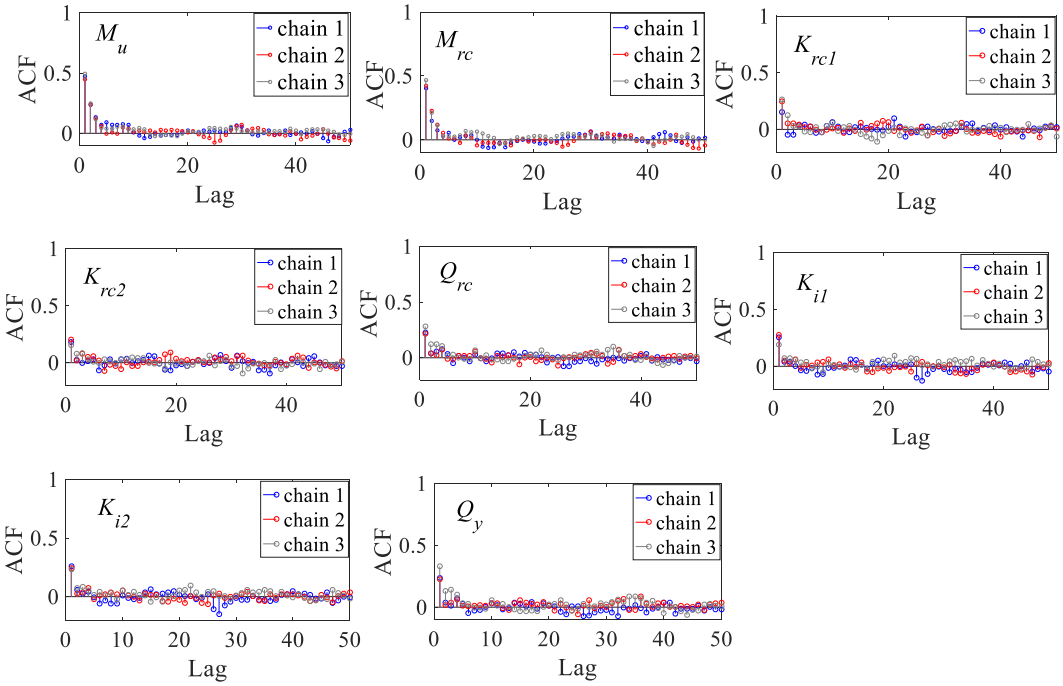

Fig. 6.9 Autocorrelation function of the eight uncertain parameters for 3 chains of walks.

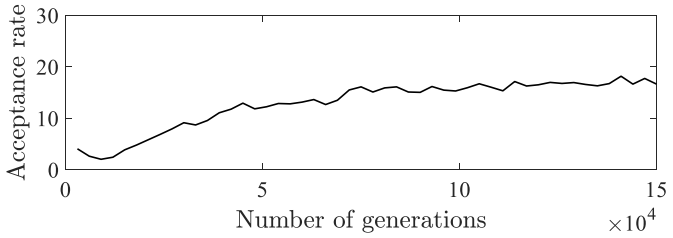

Fig. 6.10 Evolution of acceptance rate

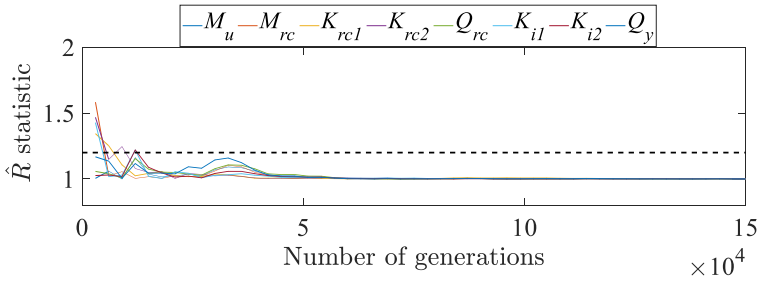

Fig. 6.11 Convergence diagnostics of sample chains, (note: dash line indicates critical threshold valued at 1.2).

Verification of posterior distributions of the model parameters

The applicability of the Bayesian inference using weighted time-history responses is verified by comparing with one using transfer ratios at all frequencies of less than 5 Hz. The latter has been expected to provide more reliable posterior distributions owing to the ability of capturing responses in the wide dominant frequency range of the structure. The posterior distributions are derived by accepting any responses across the deviation interval of the observation noise. Figure 6.12 shows resulting marginal posterior densities of the model parameters using the features characterized by RMS of acceleration time-history for each 1s and transfer ratios under the Kobe earthquake (PGA = 600 gal). It is interesting that the simulated distributions in terms of the weighted acceleration time-history usage shift to the left side; in contrast, ones using transfer ratios concentrate to the right side of the nominal point. i.e., the coefficient equal to 1. It can be interpreted that the probabilistic distributions using the weighted time-history responses tend to underestimate the "true" value of the model parameters, this is contrary to the derived distributions using transfer ratios. The maximum bias between the posterior mean of Q_{rc} and the "true" coefficient in term of the weighted time-history responses is at approximate 1.6×10^{-4}, i.e., around 0.016% variance that is even smaller than one using the features in frequency domain. The small bias is considered not affecting much on the reliability of posterior distributions. This conveys that the inference using the weighted time-history response features in small time segments can be applied to simulate the posterior precision with high reliability.

The effect of sensitivity evaluations on the reliability of derived posterior densities will be proved by comparing the posterior densities of the eight parameters under two different earthquake magnitudes, with PGA of 60 and 600 gal. It is noticed that the sensitivity was roughly evaluated by using the responses characterized by RMS of the whole time-histories (T = 30s) or RMS of all transfer ratios at the frequencies of less than 5 Hz (f < 5 Hz). For UQ, increasing the number of features as much is essential to reduce ill-posed inverse problems, e.g., the maximum likelihood estimation. Under the undamaged condition, the posterior distributions are expected to have point estimates, i.e., Maximum-A-Posterior (MAP) and mean, valued at a nominal coefficient of 1. As presented in section 5.1.2 regarding the sensitivity evaluations of the model parameters, M_u, K_{rc1}, K_{i1}, Q_y in case of 60 gal PGA hold higher main effect, and the others have less effect to the responses than ones in the original EQ (see Fig. 5.4). Correspondingly, Fig. 6.13 shows that the posterior distributions of M_u, K_{rc1}, K_{i1}, Q_y under 10% level have point estimates approximately 1 and less uncertainty than ones in the 100% EQ level. However, the opposite indication is dedicated for the remaining parameters M_{rc}, K_{rc2}, Q_{rc}, K_{i2}. While M_u is the most sensitive parameter, K_{rc2} and Q_{rc} have no effect to the responses under earthquake PGA = 60 gal. The posterior distribution of M_u is hence well-constrained by

the observed data and has the most probable point estimates, MAP and mean being closely equal to 1. In contrast, the distributions of K_{rc2} and Q_{rc} have wide uncertainty that is theoretically supposed to be a uniform distribution with the fact that no nonlinear response is found under this small earthquake. However, the little correlation between the parameters is supposed to cause the bias in the distribution quality. Therefore, it is suggested that fixing the noninfluential parameters which have very low total effect may eliminate this problem in the multivariate inference. Regarding to UQ results under the original EQ, the most sensitive parameter K_{i2} shows the most precise distribution with MAP and mean of 1.0001. To sum up, the precision of derived posteriors strongly depends on the sensitivity degree of each model parameter. By examining sensitivity under various seismic loadings, the optimal posterior distributions for each parameter can be achieved.

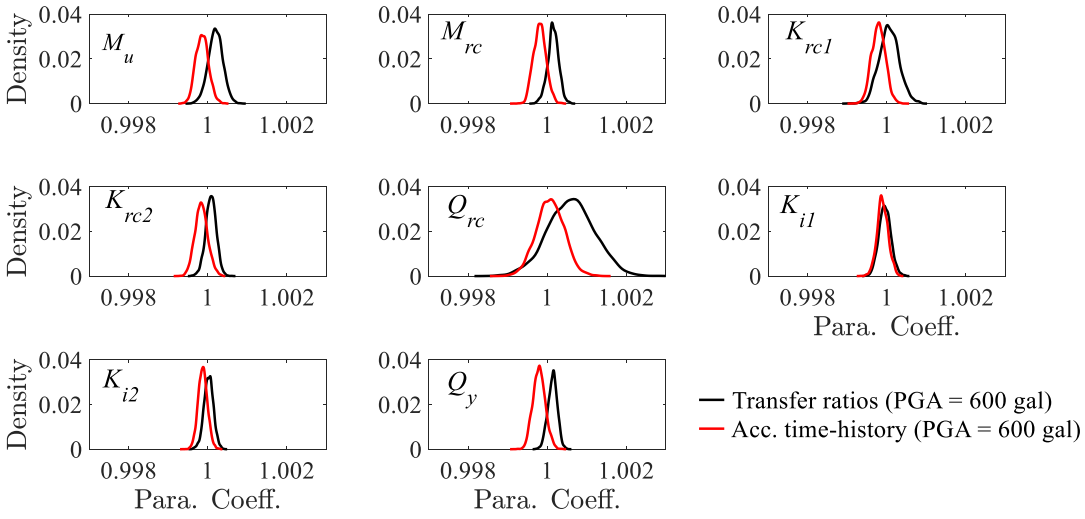

Fig. 6.12 Empirical posterior density of uncertain parameters in terms of RMS of superstructure acceleration time-history for each 1s and transfer ratios of all frequencies less than 5 Hz under the original Kobe earthquake (100% level).

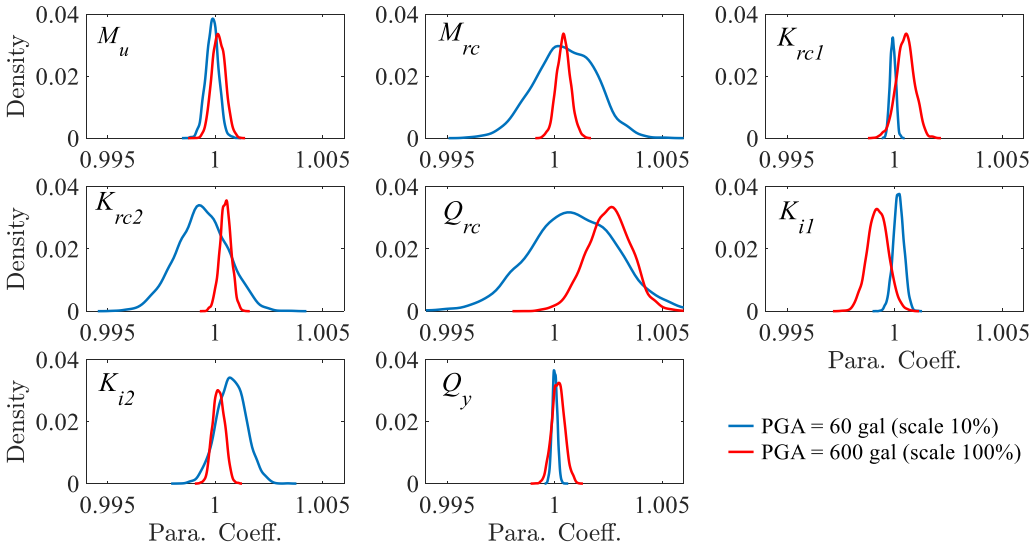

Fig. 6.13 Empirical posterior density of uncertain parameters in terms of RMS of superstructure acceleration for each 1s under two earthquake levels, 10% and 100% corresponding to PGA of 60 and 600 gal of Kobe earthquake.

6.2.2 A sequential procedure for model updating using data from various earthquake levels

Response feature is RMS of acceleration time-history

This section presents an updating procedure of the uncertain parameters using available long-term data. The response acceleration of the superstructure and pier was weighted by RMS for each 1s due to the incapability of constructing the metamodels and quantifying the uncertainty with very high-dimensional time-history features. Consequently, a total of 30 RMS features of the 30s excitation duration was adopted. Considering inverse propagation capability of the uncertainty, a deterioration condition of the bridge was assumed with 5% reduction of K_{rc1}, K_{rc2}, K_{i1} and Q_y and the other factors with no change. To facilitate the inverse inference, uniform distributed parameter values following Latin Hypercube sampling was normalized through coefficient bounds between 0.9 and 1.1, with 1 being nominal coefficient. The total 50000 iterations including 5000 burn-in were called through MCMC. The convergence analysis is also performed for case under each earthquake levels to ensure the posterior distributions approaching convergence. Figure 5.5 indicates that M_u, M_{rc}, K_{rc1}, K_{rc2}, Q_{rc}, K_{i1}, K_{i2} and Q_y highly affect the response features at 10%, 60%, 40%, 160%, 60%, 40%, 100%, and 15% levels, corresponding to PGA 60, 360, 240, 958, 360, 240, 600, and 90 gal, respectively. Marginal posterior distributions obtained by UQ under these earthquakes are shown in Fig. 6.14.

Maximum a posterior (MAP) and distribution mean of M_u, M_{rc}, Q_{rc}, and K_{i2} are found at approximate 1 while ones of K_{rc1}, K_{rc2}, K_{i1}, and Q_y values at around 0.95. In general, the posterior densities in Fig 6.14 are well-constrained by the experimental data and well-defined by nearly Gaussian distributions. It is concluded that a sequential uncertainty quantification procedure can be constructed by comparing unnormalized main effects considering available long-term measured data.

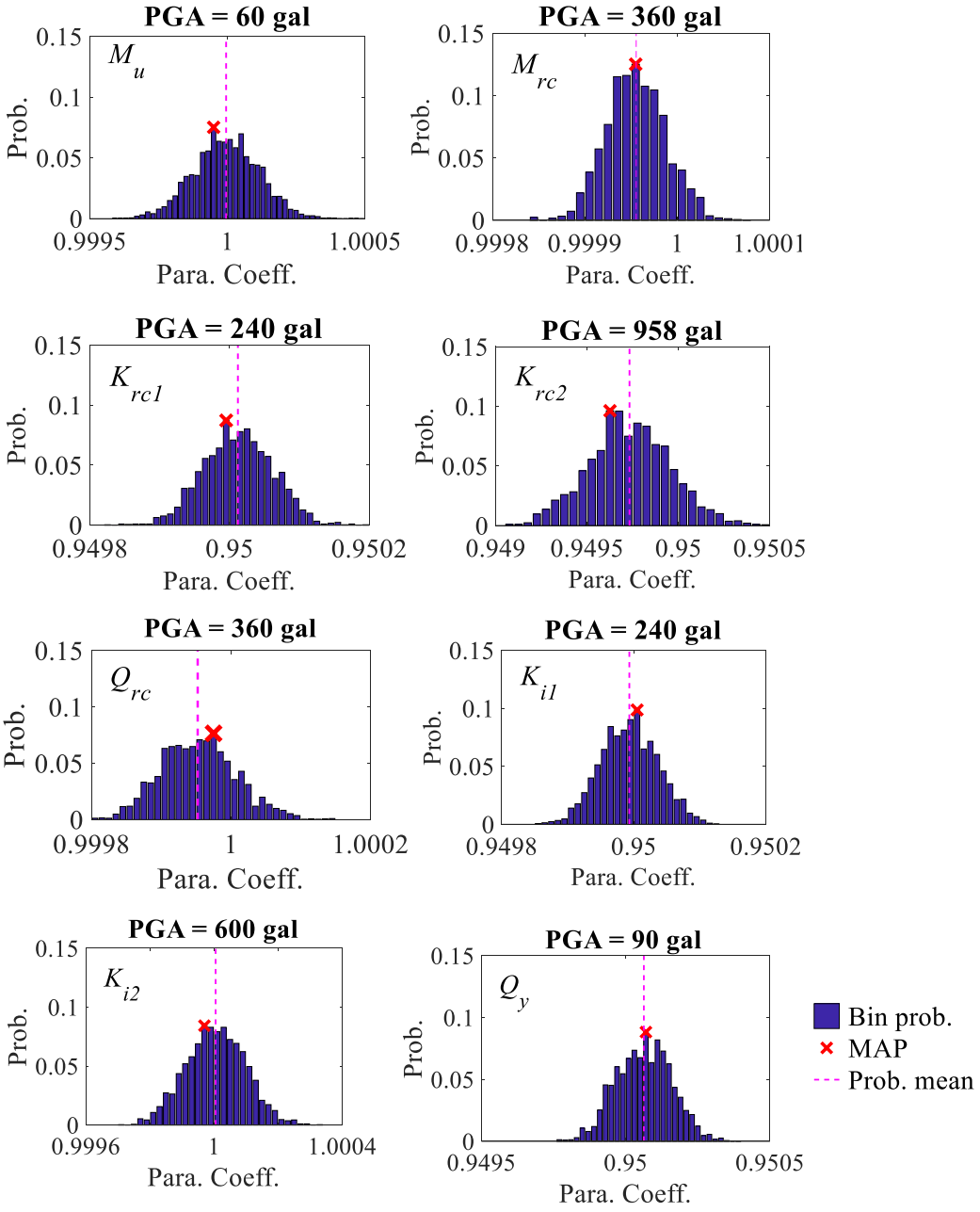

Fig. 6.14 Marginal posterior distributions of the eight uncertain parameters regarding extracted response features in time domain under the healthy and deteriorated conditions of the bridge.

Response feature is transfer ratios

The UQ procedure was also conducted for response features in frequency domain. Herein, transfer ratios in frequency range less than 5 Hz were adopted. Figure 5.6 points out that 7 parameters M_u, M_{rc}, K_{rc1}, Q_{rc}, K_{i1}, K_{i2} and Q_y except for K_{rc2} are highly affect the response features at PGA 180, 420, 30, 420, 60, 503, 360 gal. Marginal posterior distributions obtained by UQ under these earthquakes are shown in Fig. 6.15. Maximum a posterior (MAP) and distribution mean of M_u, M_{rc}, Q_{rc}, and K_{i2} are found at approximate 1 while ones of K_{rc1}, K_{i1}, and Q_y values at around 0.95. It is noticed that K_{rc2} with sensitivity nearly zero in all considered seismic magnitudes cannot inferred using earthquake responses in frequency domain.

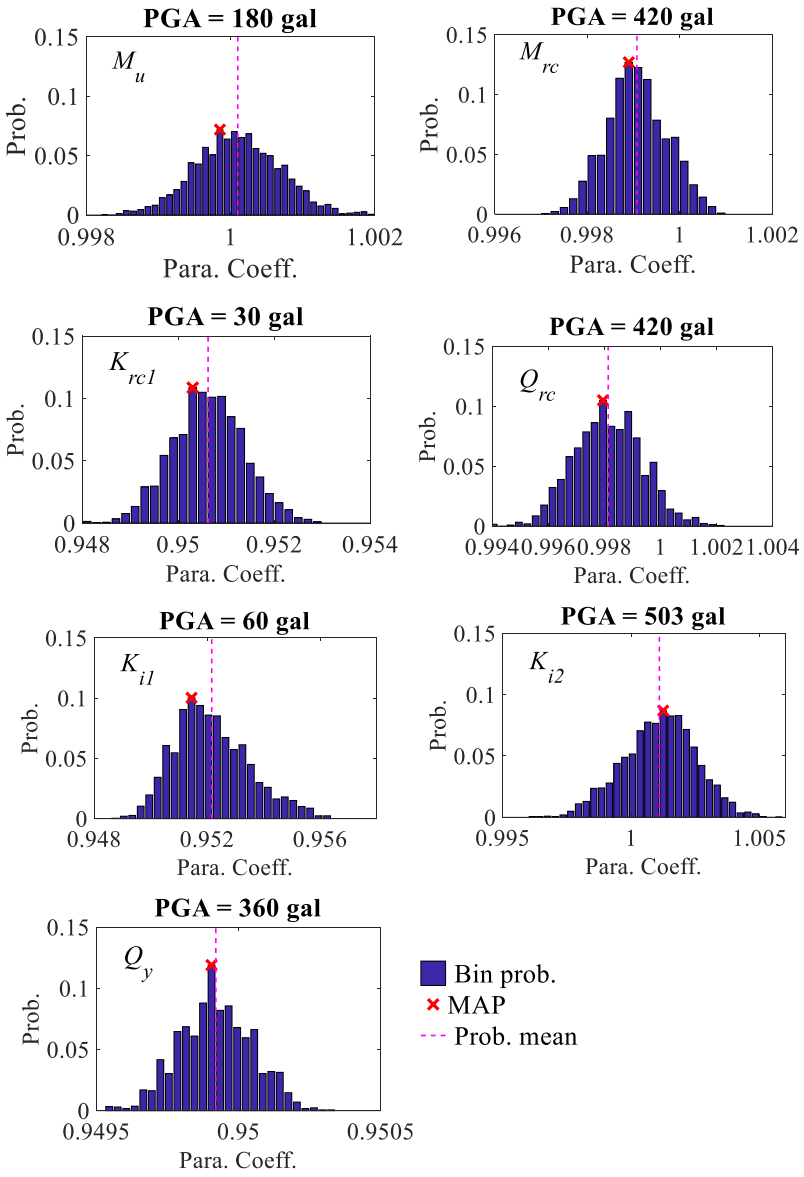

Fig. 6.15 Marginal posterior distributions of the seven uncertain parameters (except for K_{rc2}) regarding RMS of transfer ratios under the healthy and deteriorated conditions of the bridge

Chapter 7

Summary, Conclusion, and Future Work

7.1 Summary of major contributions

The core idea in this thesis is to generate reliable posterior distributions of the uncertain model parameters and realize the seismic risks of the existing structures using the updated numerical models. To obtain this, sensitivity analysis and uncertainty quantification were conducted using Kriging metamodels under different seismic characteristics. The models that must be dealt with in this study include: (1) a base-isolated asymmetric building with the large number of DOFs to represent a complex geometry; (2) a seismically isolated bridge pier desinged in Japan Design Specifications of Highway Bridges.

Bayesian sensitivity analysis (BSA) using a small learning sample with physical output features can be applied on complex building structures under various seismic excitations with high accuracy and efficiency. Running time is drastically decreased when using metamodels in BSA in comparison with Monte Carlo sensitivity analysis (MCSA) which is commonly applied on full models.

Transfer function for a set of earthquakes before and after the main shock indicates that there were stiffness reduction indicators of the superstructure due to the large earthquake of March 11, 2011. The analysis of equivalent stiffness variance of the isolation system over time also points out that the stiffness variance of the isolation system was temporal and could recover in 4 months after the main shock.

Global sensitivity analysis on local stiffness parameters of the superstructure indicates which parameters of lower floors should be considered in model updating. By comparing SIs against RMS and RMSE of outputs, parameter uncertainties due to local stiffness changes and modeling errors can be predicted. Moreover, the influence level of one factor to the dynamic response at various positions of the building can be also indicated. As a result, this can strongly influence parameter selection in model updating. Further, GSA of structural parameters has a strong relationship with characteristics of dominant mode shapes. The multi-input multi-output relation of numerical models can be interpreted comprehensively in any earthquakes. It is hence recommended for understanding the dynamic response of existing buildings better. Furthermore, GSA results in the frequency

domain can support selection of appropriate sensors in model updating. The study also suggests a strategy for effective monitoring data usage by limiting data acquisition to appropriate bandwidths via main sensitivity index.

To evaluate sensitivity of the model parameters under random seismic excitations, there is a strong need to consider uncertainties from both loading history and structural response features. Sensitivity analysis was conducted on two different earthquake characteristics: Kobe earthquake with PGA of 600 gal and the frequency content coinciding with the frequency of the bridge, and Mid-Niigata earthquake with PGA of 1715 gal and dominant frequency range of larger than 5 Hz. Kobe earthquake causes much higher sensitivity effect on the parameters than Mid-Niigata earthquake does. This indicates that structures having fundamental natural frequencies out of the range of ground motion will exhibit less sensitivity effect than the ones having two frequency ranges coinciding. Therefore, its effect on sensitivity results can be neglected. Moreover, by considering the most sensitive effects of the parameters under different earthquake characteristics and responses in time and frequency domain, response data and features can be selected for the uncertainty quantification procedure.

The precision of the posterior distributions was verified under two scenarios: (1) Bayesian inference using small segment time-history responses tends to underestimate "true value" of the parameters. However, this bias is small to affect the precision of the posteriors; hence, UQ using response features in time domain can be conducted instead of using modal responses. (2) Sensitivity evaluations have strong effect on the reliability of UQ results. More sensitive parameters are verified to have more precise posterior distributions derived by UQ.

The study proposes a sequential uncertainty quantification procedure based on sensitivity analysis using long-term monitoring data to derive optimal and efficient posterior distributions of the structural model parameters. The procedure can quantify epistemic uncertainties, i.e., structural changes subjected to large earthquakes and modeling errors using the long-term data measured from the considered damaging earthquake and later. Moreover, the procedure allows the effective and efficient use of the long-term monitoring data in reliability analysis. This proposed procedure is expected to be applicable for any civil structures under seismic excitations.

7.2 Future work

Sensitivity analysis and uncertainty quantification in Bayesian framework are commonly applied in many fields including aerospace. However, it is not widely explored in structural engineering according to the author. Since the Bayesian statistics can solve many uncertainty problems, e.g., in the structure modeling, some limitations are required for further research.

Strong correlation between the parameters as considering solving Bayesian statistics in multi-variate space will make the resulting posterior distributions less reliable. This problem is actively concerned recently. Intrinsically, if the parameters of concern are highly correlated, it seems inefficient to reduce the correlation by increasing the number of generations, i.e., Monte Carlo iterations in this study. Therefore, we expect to have better solutions to countermeasure the recent limitation in future work.

The aim of generating optimal and efficient posterior distributions of the parameters has been achieved. These posterior distributions can be involved in reliability estimation to obtain new fragility curve of existing structures.

References

Abdel-Khalik, H. *et al.* (2008) 'Uncertainty Quantification, Sensitivity Analysis, and Data Assimilation for Nuclear Systems Simulation', *Nuclear Data Sheets*, 109(12), pp. 2785–2790. doi: 10.1016/j.nds.2008.11.010.

Archer, G. E. B., Saltelli, A. and Sobol, I. M. (1997) 'Sensitivity measures, anova-like techniques and the use of bootstrap', *Journal of Statistical Computation and Simulation*, 58(2), pp. 99–120. doi: 10.1080/00949659708811825.

Asher, M. J. *et al.* (2015) 'A review of surrogate models and their application to groundwater modeling', *Water Resources Research*, 51(8), pp. 5957–5973. doi: 10.1002/2015WR016967.

Au, S. K. (2012) 'Fast Bayesian ambient modal identification in the frequency domain, Part II: Posterior uncertainty', *Mechanical Systems and Signal Processing*, 26(1), pp. 76–90. doi: 10.1016/j.ymssp.2011.06.019.

Becker, W. *et al.* (2012) 'Bayesian sensitivity analysis of a nonlinear finite element model', *Mechanical Systems and Signal Processing*, 32, pp. 18–31. doi: 10.1016/j.ymssp.2012.03.009.

Besag, J. *et al.* (1995) 'Bayesian Computation and Stochastic Systems', *Statistical Science*, 10(1), pp. 3–41. doi: 10.1214/ss/1177010123.

Ter Braak, C. J. F. (2006) 'A Markov Chain Monte Carlo version of the genetic algorithm Differential Evolution: Easy Bayesian computing for real parameter spaces', *Statistics and Computing*, 16(3), pp. 239–249. doi: 10.1007/s11222-006-8769-1.

Catbas, F. N., Susoy, M. and Frangopol, D. M. (2008) 'Structural health monitoring and reliability estimation: Long span truss bridge application with environmental monitoring data', *Engineering Structures*, 30(9), pp. 2347–2359. doi: 10.1016/j.engstruct.2008.01.013.

Chen, W., Jin, R. and Sudjianto, A. (2006) 'Analytical Global Sensitivity Analysis and Uncertainty Propagation for Robust Design', *Journal of Quality Technology*, 38(4), pp. 333–348. doi: 10.4271/2004-01-0429.

Cukier, R. I. *et al.* (1973) 'Study of the sensitivity of coupled reaction systems to uncertainties in rate coefficients. I Theory', *Journal of Chemical Physics*, 59(8), pp. 3873–3878. doi: 10.1063/1.1680571.

Franck, I. M. and Koutsourelakis, P. S. (2017) 'Multimodal, high-dimensional, model-based, Bayesian inverse problems with applications in biomechanics', *Journal of Computational Physics*, 329, pp. 91–125. doi: 10.1016/j.jcp.2016.10.039.

Frangopol, D. M., Strauss, A. and Kim, S. (2008) 'Bridge Reliability Assessment Based on Monitoring', *Journal of Bridge Engineering*, 13(3), pp. 258–270. doi: 10.1061/(ASCE)1084-0702(2008)13:3(258).

Gelman, A. and Rubin, D. B. (1992) 'Inference from Iterative Simulation Using Multiple Sequences', *Statistical Science*, 7(4), pp. 457–472. doi: 10.1214/ss/1177011136.

Ghanem, R. G. and Spanos, P. D. (1991) *Stochastic Finite Elements: A Spectral Approach*, *_Book*. doi: 10.1007/978-1-4612-3094-6.

Heiselberg, P. *et al.* (2009) 'Application of sensitivity analysis in design of sustainable buildings', *Renewable Energy*, 34(9), pp. 2030–2036. doi: 10.1016/j.renene.2009.02.016.

Helton, J. C. (1993) 'Uncertainty and sensitivity analysis techniques for use in performance assessment for radioactive waste disposal', *Reliability Engineering & System Safety*, 42(2–3), pp. 327–367. doi: 10.1016/0951-8320(93)90097-I.

Higdon, D. *et al.* (2008) 'Computer Model Calibration Using High-Dimensional Output', *Journal of the American Statistical Association*, 103(482), pp. 570–583. doi: 10.1198/016214507000000888.

Hoeffding, W. (1948) 'A Class of Statistics with Asymptotically Normal Distribution', *The Annals of Mathematical Statistics*, 19(3), pp. 293–325. doi: 10.1214/aoms/1177730196.

Homma, T. and Saltelli, A. (1996) 'Importance measures in global sensitivity analysis of nonlinear models', *Reliability Engineering & System Safety*, 52, pp. 1–17. doi: 10.1016/0951-8320(96)00002-6.

Japan Road Association (2004) 'Manual on Bearing of Highway Bridges', *Tokyo: Maruzen*.

Japan Road Association (2012) 'Design Specifications of Highway Bridges: Part V Seismic Design', *Tokyo: Maruzen*.

Juang, J.-N. (1997) 'System Realization Using Information Matrix', *Journal of Guidance, Control, and Dynamics*, 20(3), pp. 492–500. doi: 10.2514/2.4068.

Kennedy, M. C. and O'Hagan, A. (2000) 'Predicting the output from a complex computer code when fast approximations are available', *Biometrika*, 87(1), pp. 1–13. doi: 10.1093/biomet/87.1.1.

Kennedy, M. C. and O'Hagan, A. (2001a) 'Bayesian Calibration of Computer Models', *Journal of the Royal Statistical Society. Series B (Statistical Methodology)*, 63(3), pp. 425–464. doi: 10.1111/1467-9868.00294.

Kennedy, M. C. and O'Hagan, A. (2001b) 'Bayesian Calibration of Computer Models', *Journal of the Royal Statistical Society. Series B (Statistical Methodology)*, 63(3), pp. 425–464. doi: 10.1111/1467-9868.00294.

Krige, D. G. (1952) 'A Statistical Approach to Some Basic Mine Valuation Problems on the Witwatersrand', *Journal of the Chemical, Metallurgical and Mining Society of South Africa*, pp. 201–215. doi: 10.2307/3006914.

Lam, J. C. and Hui, S. C. M. (1996) 'Sensitivity analysis of energy performance of office buildings', *Building and Environment*, 31(1), pp. 27–39. doi: 10.1016/0360-1323(95)00031-3.

Lomas, K. J. and Eppel, H. (1992) 'Sensitivity analysis techniques for building thermal simulation programs', *Energy and Buildings*, 19(1), pp. 21–44. doi: 10.1016/0378-7788(92)90033-D.

Metropolis, N. *et al.* (1953) 'Equations of state calculations by fast computing machine', *Journal of Chemical Physics*, 21(6), pp. 1087–1092. doi: http://dx.doi.org/10.1063/1.1699114.

Morris, M. D. (1991) 'Factorial sampling plans for preliminary computational experiments', *Technometrics*, 33(2), pp. 161–174. doi: 10.1080/00401706.1991.10484804.

El Moselhy, T. A. and Marzouk, Y. M. (2012) 'Bayesian inference with optimal maps', *Journal of Computational Physics*, 231(23), pp. 7815–7850. doi: 10.1016/j.jcp.2012.07.022.

Nagel, J. B. and Sudret, B. (2016) 'Spectral likelihood expansions for Bayesian inference', *Journal of Computational Physics*, 309, pp. 267–294. doi: 10.1016/j.jcp.2015.12.047.

Nishikawa T., Konno K., Fujino Y., Nakayama M. (2014) 'High-density Structural health monitoring System for High-rise Seismic Isolated Building Using existing Network Facilities', *Journal of Japan Association for Earthquake Engineering*, 14(2), pp. 1–15.

Nishio, M., Farrar, C., Hemez, F., Stull, C., Park, G., Cornwell, P. and Figueiredo, E., Luscher, D.J., Worden, K. (2016) 'Feature Extraction for Structural Dynamics Model Validation', *LA-14489, Los Alamos National Laboratory*.

Nishio, M., Marin, J. and Fujino, Y. (2012) 'Uncertainty quantification of the finite element model of existing bridges for dynamic analysis', *Journal of Civil Structural Health Monitoring*, 2(3–4), pp. 163–173. doi: 10.1007/s13349-012-0026-z.

Oakley, J. E. and O'Hagan, A. (2004) 'Probabilistic sensitivity analysis of complex models: A Bayesian approach', *Journal of the Royal Statistical Society. Series B: Statistical Methodology*, 66(3), pp. 751–769. doi: 10.1111/j.1467-9868.2004.05304.x.

Özer, E. and Soyöz, S. (2015) 'Vibration-based damage detection and seismic performance assessment of bridges', *Earthquake Spectra*, 31(1), pp. 137–157. doi: 10.1193/080612EQS255M.

Rasmussen, C. E. (2006) 'Gaussian processes for machine learning', *International journal of neural systems*, 14(2), pp. 69–106. doi: 10.1142/S0129065704001899.

Regis, R. G. and Shoemaker, C. A. (2005) 'Constrained global optimization of expensive black box functions using radial basis functions', *Journal of Global Optimization*, 31(1), pp. 153–171. doi: 10.1007/s10898-004-0570-0.

Robert, C. P. and Casella, G. (2004) *Monte Carlo Statistical Methods*, *Springer, New York. Sanso, B. and Guenni, L*. doi: 10.1007/978-1-4757-4145-2.

Robinson, W. H. (1982) 'Lead-rubber hysteretic bearings suitable for protecting structures during earthquakes', *Earthquake Engineering & Structural Dynamics*, 10(4), pp. 593–604. doi: 10.1002/eqe.4290100408.

Sacks, J. *et al.* (1989) 'Design and Analysis of Computer Experiments', *Statistical Science*, pp. 409–435. doi: 10.1214/ss/1177012413.

Saltelli, A. (2002) 'Making best use of model evaluations to compute sensitivity indices', *Computer Physics Communications*, 145(2), pp. 280–297. doi: 10.1016/S0010-4655(02)00280-1.

Saltelli, A. (2008) *Global Sensitivity Analysis*. The Primer. London: John Wiley & Sons.

Schueremans, L. and Van Gemert, D. (2005) 'Benefit of splines and neural networks in simulation based structural reliability analysis', *Structural Safety*, 27(3), pp. 246–261. doi: 10.1016/j.strusafe.2004.11.001.

Schwab, C. *et al.* (2012) 'Sparse deterministic approximation of Bayesian inverse problems', *Inverse Problems*, 28(4). doi: 10.1088/0266-5611/28/4/045003.

Serdar Soyoz, M.ASCE; Maria Q. Feng, M.ASCE; and Masanobu Shinozuka, H. M. A. (2010) 'Structural Reliability Estimation with Vibration-Based Identified Parameters', *Journal of Engineering Mechanics*, 136(1), pp. 100–106.

Singhal, A. and Kiremidjian, A. S. (1998) 'Bayesian Updating of Fragilities with Application to RC Frames', *Journal of Structural Engineering*, 124(8), pp. 922–929. doi: 10.1061/(ASCE)0733-9445(1998)124:8(922).

Siringoringo, D. M. and Fujino, Y. (2014) 'Long-term seismic monitoring of base-isolated building with emphasis on servicability assessment', *Earthquake Engineering & Structural Dynamics*, 44(4), pp. 637–655. doi: 10.1002/eqe.

Siringoringo, D. M. and Fujino, Y. (2015) 'Seismic response analyses of an asymmetric base-isolated building during the 2011 Great East Japan (Tohoku) Earthquake', *Structural Control and Health Monitoring*, 22(1), pp. 71–90. doi: 10.1002/stc.1661.

Sobol', I. M. (1993) 'Sensitivity Estimates for Nonlinear Mathematical Models', *Mathematical Modeling and Computational experiment*, pp. 407–414. doi: 1061-7590/93/04407-008.

Sobol, I. M. (1976) 'Uniformly distributed sequences with an additional uniform property', *USSR Computational Mathematics and Mathematical Physics*, 16(5), pp. 236–242. doi: 10.1016/0041-5553(76)90154-3.

Sobol, I. M. (1990) 'Sensitivity analysis for nonlinear mathematical models', *Matematicheskoe Modelirovanie*, 2(1), pp. 112–118. doi: 10.18287/0134-2452-2015-39-4-459-461.

Sobol, I. M. (1993) 'Sensitivity Analysis for nonlinear mathematical models', *Mathematical Modeling & Computational Experiment*, 1(4), pp. 407–414.

Sobol, I. M. (2001) 'Global sensitivity indices for nonlinear mathematical models and their Monte Carlo estimates', *Mathematics and Computers in Simulation*, 55(1–3), pp. 271–280. doi: 10.1016/S0378-4754(00)00270-6.

Spear, R. C. and Hornberger, G. M. (1980) 'Eutrophication in peel inlet-II. Identification of critical uncertainties via generalized sensitivity analysis', *Water Research*, 14(1), pp. 43–49. doi: 10.1016/0043-1354(80)90040-8.

Sraj, I. *et al.* (2014) 'Uncertainty quantification and inference of Manning's friction coefficients using DART buoy data during the Tōhoku tsunami', *Ocean Modelling*, 83, pp. 82–97. doi: 10.1016/j.ocemod.2014.09.001.

Stone, M. (1974) 'Cross-Validatory Choice and Assessment of Statistical Predictions', *Journal of the Royal Statistical Society*, 36(2), pp. 111–147. doi: 10.2307/2984809.

Takeda, Sozen and Nielsen (1970) 'Reinforced Concrete Response to Simulated Earthquakes', *Journal of the Structural Division*, pp. 2557–2573. doi: 10.1017/CBO9781107415324.004.

Tian, W. (2013) 'A review of sensitivity analysis methods in building energy analysis', *Renewable and Sustainable Energy Reviews*, 20, pp. 411–419. doi: 10.1016/j.rser.2012.12.014.

Tyler, R. and Robinson, W. (1984) 'High-strain tests on lead-rubber bearings for earthquake loadings', *Bulletin of the New Zealand Society for Earthquake Engineering*, 17(2), pp. 90–105. Available at: http://www.nzsee.org.nz/publications/nzsee-quarterly-bulletin/vol-11-20/.

Vrugt, J. A. *et al.* (2008) 'Treatment of input uncertainty in hydrologic modeling: Doing hydrology backward with Markov chain Monte Carlo simulation', *Water Resources Research*, 44(12). doi: 10.1029/2007WR006720.

Vrugt, J. A. *et al.* (2009) 'Accelerating Markov Chain Monte Carlo Simulation by Differential Evolution with Self-Adaptive Randomized Subspace Sampling', *International Journal of Nonlinear Sciences and Numerical Simulation*, 10(3). doi: 10.1515/IJNSNS.2009.10.3.273.

Vrugt, J. A. (2016) ‘Markov chain Monte Carlo simulation using the DREAM software package: Theory, concepts, and MATLAB implementation’, *Environmental Modelling and Software*, 75, pp. 273–316. doi: 10.1016/j.envsoft.2015.08.013.

Welch, W. J. *et al.* (1992) ‘Screening, predicting, and computer experiments’, *Technometrics*, 34(1), pp. 15–25. doi: 10.1080/00401706.1992.10485229.

Xiong, F. F. *et al.* (2010) ‘A new sparse grid based method for uncertainty propagation’, *Structural and Multidisciplinary Optimization*, 41(3), pp. 335–349. doi: 10.1007/s00158-009-0441-x.

Xiu, D. and Karniadakis, G. E. M. (2002) ‘THE WIENER – ASKEY POLYNOMIAL CHAOS FOR STOCHASTIC’, *Society*, 24(2), pp. 619–644. doi: 10.1137/S1064827501387826.